Four Dimensional (4D) Microstructural and Electrochemical Characterization of Dissimilar-metal Corrosion in Naval Structural Joints

by

Sridhar Niverty

A Dissertation Presented in Partial Fulfillment
of the Requirements for the Degree
Doctor of Philosophy

Approved April 2020 by the
Graduate Supervisory Committee:

Nikhilesh Chawla, Chair
Yongming Liu
Kumar Ankit
Xianghui Xiao

ARIZONA STATE UNIVERSITY

May 2020

ABSTRACT

AA 7XXX alloys are used extensively in aircraft and naval structures due to their excellent strength to weight ratio. These alloys are often exposed to harsh corrosive environments and mechanical stresses that can compromise their reliability in service. They are also coupled with fasteners that are composed of different materials such as Titanium alloys. Such dissimilar metal contact facilitates galvanic and crevice corrosion, which can further reduce their lifetimes. Despite decades of research in the area, the confluence of mechanical, microstructural, and electrochemical aspects of damage is still unclear. Traditionally, 2D and destructive methods have often been employed to study the corrosion and cracking behavior in these systems which can be severely limiting and lead to inaccurate conclusions. This dissertation is aimed at comprehensively studying the corrosion and cracking behavior of these systems using time-dependent 3D microstructural characterization, as well as correlative microscopy. The microstructural evolution of corrosion in AA 7075 was studied using a combination of potentiodynamic polarization, X-ray Computed Tomography (XCT) and Transmission X-ray Microscopy (TXM). In both experiments, a strong emphasis was placed on studying localized corrosion attack at constituent particles and intergranular corrosion. With an understanding of the alloy's corrosion behavior, a dissimilar alloy couple comprising AA 7075 / Ti-6Al-4V was then investigated. *Ex situ* and *in situ* x-ray microtomography was used extensively to investigate the evolution of pitting corrosion and corrosion fatigue in AA 7075 plates fastened separately with Ti-6Al-4V screws and rivets. The 4D tomography combined with the extensive fractography yielded valuable information pertaining the preferred sites of pit initiation, crack initiation and growth in these complex geometries. The use of correlative

microscopy-based methodologies yielded multimodal characterization results that provided a unique and seminal insight on corrosion mechanisms in these materials.

DEDICATION

I dedicate this dissertation to my parents who have supported me with everything, to Harsha, Ankita and Chithkala for being my role models, to all of my friends and teachers from Manasarowar Pushkarini Vidhyashrama, Kendriya Vidyala, NITK Suratkal, JSW Steels, Arizona State University and to my research group at the Center for 4D Materials Science. You are ALL responsible for making me the person I am today. So, I dedicate this dissertation to you.

ACKNOWLEDGMENTS

I would like to primarily thank my advisor, Prof. Nikhilesh Chawla, for continually guiding and supporting me as a graduate student. I am extremely grateful to him for giving me the opportunity to work on cutting edge Materials Science research and for being an excellent mentor. I am also grateful to my committee members Dr. Yongming Liu, Dr. Kumar Ankit and Dr. Xianghui Xiao for agreeing to evaluate my doctoral research. I would like to thank Mr. Bill Nickerson and the Office of Naval research for providing us with the financial support to conduct this research. The Advance Photon Source at Argonne National Laboratory has always been our research group's second home and for that, I would like to thank Dr. Xianghui Xiao, Dr. Vincent De Andrade and Dr. F. De Carlo. I would like to acknowledge the support and service from the ASU machine shop and their machinists James, Jerry, Bill and John who I have had the pleasure of learning from. I would like to thank Dr. Jason Williams and my colleagues at the Center for 4D Materials Science for their guidance and collaboration. Lastly, I would like to extend my deepest gratitude to my family and friends for having supported me through everything.

TABLE OF CONTENTS

Page

LIST OF TABLES vi

LIST OF FIGURES vii

CHAPTER

1. INTRODUCTION 1

2. LITERATURE REVIEW 5

2.1 Microstructure of Aluminum Alloys 5

2.2 Corrosion Studies on AA 7075 8

2.3 Corrosion Fatigue Behavior of AA 7075 11

3. MULTISCALE INVESTIGATION OF DAMAGE INITIATION AND PROPAGATION DURING CORROSION OF AA 7075-T651 USING CORRELATIVE MICROSCOPY 20

3.1 Introduction 20

3.2 Materials and Experimental Procedure 24

3.3 Results and Discussion 29

3.3.1 Microstructural Characterization of AA 7075 29

3.3.2 X-ray Tomography Observations 30

3.3.3 SEM Observations 34

3.3.4 Pitting Corrosion and Exfoliation Behavior 40

CHAPTER Page

3.3.5 Concentric Corrosion Patterns 46

3.3.6 Fe-rich Inclusion Dissolution Behavior 49

3.4 Summary 54

4. NANOSCALE 4D MICROSTRUCTURAL CHARACTERIZATION OF CORROSION IN ALUMINUM ALLOYS USING TRANSMISSION X-RAY MICROSCOPY (TXM) 56

4.1 Introduction 56

4.2 Materials and Experimental methods 58

4.3 Results and Discussion 66

4.3.1 X-ray Tomography Data and Processing 66

4.3.2 Corrosion Visualization and Quantification 67

4.4 Summary 76

5. 4D MICROSTRUCTURAL CHARACTERIZATION OF CORROSION AND CORROSION-FATIGUE IN A TI-6AL-4V / AA 7075-T651 JOINT IN SALTWATER 77

5.1 Introduction 77

5.2 Materials and Experimental Procedure 81

5.3 Results and Discussion 86

5.3.1 Microstructural Characterization of the Aluminum Alloy 7075-T651 Plate (anode) 86

5.3.2 X-ray Microtomography Scans and Data Post Processing 87

CHAPTER Page

5.3.3 Microstructure Evolution of Pitting corrosion 88

5.3.4 Fractographic Analysis of the Fractured Specimen after Fatigue 92

5.3.5 Crack Initiation Sites 100

5.3.6 Sequence of Crack Initiation and Propagation 107

5.4 Summary 109

6. *IN SITU* CHARACTERIZATION OF CORROSION FATIGUE IN A NAVAL STRUCTURAL JOINT IN SALTWATER ENVIRONMENT 111

6.1 Introduction 111

6.2 Materials and Experimental Procedure 114

6.3 Results and Discussion 121

6.3.1 Tomography Observations in Type A Specimens 121

6.3.2 Tomography Observations in Type B Specimens 123

6.3.3 Fractographic Analysis of the Fracture Specimens after Fatigue 125

6.4 Summary 126

7. CONCLUSIONS 130

7.1 Summary of Research Findings and Recommendations 130

7.2 Future Work 134

REFERENCES 135

LIST OF TABLES

Table Page

1. Elemental Tolerances (ASTM B209-14) and Measured Chemical Composition of the AA 7075-T651 Block. 25

2. Elemental Tolerances (ASTM B209-14) and Measured Chemical Composition of the AA 7075-T651 Block 82

3. Elemental Tolerances (ASTM B265-15) and Measured Chemical Composition of the Ti-6Al-4V Screw. 83

4. Elemental Tolerances (ASTM B209-14) and Measured Chemical Composition of the AA 7075-T651 Block 116

5. Elemental Tolerances (ASTM B265-15) and Measured Chemical Composition of the Ti-6Al-4V Rivet. 116

LIST OF FIGURES

Figure Page

1. Microstructure of AA 7075- T651, (a) Metallic Inclusions, (b) Dispersoids, (c) Precipitates. 7

2. Schematic Showing the Conditions Prevailing within Faster- Plate Couples and the Locations and Propagation Path of Corrosion Damage. 14

3. (a) Schematic of the Focused Ion Beam- Scanning Electron Microscope, (b) Schematic of the Serial Sectioning Nano-Tomography Procedure. 16

4. Schematic of the Geometry of the Cylindrical Rod Specimen of AA 7075-T651 Showing Regions Covered with Rubber Cement to Expose a ~ 1mm Height as ROI. 26

5. Anodic Polarization Curve of the Potentiodynamic Polarization Scan of AA7075-T651 Highlighting the Four Regions at which the Scans were Interrupted. 27

6. Microstructure Highlighting the Different Constituent Particles in the Specimen. 30

7. Representative Images of the Outer Surfaces (From the X-ray Tomography Dataset Volume Renderings) of the Specimens Before and After Potentiodynamic Polarization Testing. Macroscopic Damage Begins Only After the Second Breakdown Potential is Surpassed. 31

8. Virtual Slice Comparison showing the ST plane for Each Specimen Before and After Potentiodynamic Polarization Testing. Red Arrows indicate Sites where Pits Initiate clearly from Fe-Rich Inclusions. Blue Arrows indicate Sites where Pits are not observed (or resolvable) to Initiate at Microstructural Constituents. 32

Figure Page

9. Virtual Slices from Regions 3 and 4 Showing Planes Parallel to Rolling Axis (L) for each Specimen Before and After Potentiodynamic Polarization Testing. Red Arrows indicate Pits in both Conditions..... 33

10. SEM + EDS Images from Specimen Interrupted Immediately Beyond the First Breakdown Potential. Comparison of a set of Earmarked Inclusions shows a Decrease in Mg Content in Mg_2Si and Al_2CuMg (S-phase) Particles as the First signs of observable Damage at this Length Scale..... 35

11. SEM and EDS Images from Specimen Interrupted immediately before the Second Breakdown Potential. Dealloying of S-phase Particles and the very First signs of Surface Corrosion are seen at this Potential with the Formation of Concentric Corrosion Patterns around Fe-Rich Inclusions..... 36

12. SEM Images from Specimen Interrupted immediately After the Second Breakdown Potential. (a) and (b) show an Earmarked portion of the Specimen with Inclusion Clusters of various Compositions. A Combination of Intergranular Corrosion (Yellow Arrows), Trenching at Fe-Rich Inclusions and Al_2CuMg Particles and Concentric Corrosion Patterns (Red Arrows) is seen to be Acting Simultaneously. (c) High Magnification Image of an Al_7Cu_2Fe Particle that has undergone Peripheral Trenching and is also accompanied by Concentric Corrosion Patterns..... 37

13. FIB Cross Section of an S-phase Dispersoid Particle. Trenching, Dealloying and Intergranular Corrosion has been observed Beneath the Particle Assisted by the presence of Grain Boundary Precipitates. 38

Figure Page

14. Region 4: SEM Images from Specimen Interrupted roughly 30 mV Beyond the Second Breakdown Potential. Apart from the Corrosion Mechanisms Acting in Region 3, Extensive Pitting with Layering is also Observed at this Potential. 39

15. Exfoliation Corrosion, (a) Observation of Exfoliation Like Action in X-ray Tomography Datasets hinted at Lamellar Structure Formation Underneath Corroding Pit surface. (b) Sequence of Images showing the Segmentation and Rendering of Pit and Sub-Surface exfoliation. (c) Example of a Corrosion Pit where a FIB Trench was Milled using Ga+ Ions showing Sub-Surface Transgranular Exfoliation like action. 41

16. Comparison of Sub-Surface Damage from Specimens Interrupted at (a) Region 3 showing Intergranular Corrosion around the Al_7Cu_2Fe Particle, and (b) Region 4 showing Extensive ELA and Grain Dissolution. 43

17. (a) Pit of Interest that was chosen for Ga+ Milling by Grazing Incidence, (b) Milled Surface Exposing Multiple Exfoliation Sites and Grain Boundary Attack, (c),(d) and (e) show the ROI, corresponding EBSD IPF Map and the corresponding Grain Boundary Misorientation Map, (f), (g), (h) and (i) Highlight a specific region within the area showing Representative ELA Initiation Behavior,(j) Segmented Image of (i) highlighting the Low and High Angle Grain Boundaries accompanied by ELA (Red arrows), (k) Yellow arrows pointing to Precipitate remnants within the ELA hinting at the ELA's propagation mechanism..... 44

18. Concentric Corrosion Patterns are observed in Region 2 (Around Fe-rich Inclusions) and Region 3 (almost all over the Surface)..... 46

Figure Page

19. Hypothesized Mechanism for the Formation of Concentric Corrosion Patterns. A combination of Induced Magnetic Field and Local Surface Current Transients could Potentially induce a Lorentz Force acting Orthogonally to the Surface which can Induce a Convective Action in the Fluid. 49

20. (a) (b) (c) (d) show the Serial Sectioning Nano-Tomography Procedure employed to obtain a 3D Array of closely spaced images that can be used to analyze small Volumes. (e) Top view of the ROI as in (a) with color coded lines pointing to the position of specific slices, (f)(g)(h)(i)(j) show five representative slices that show Sub-surface Corrosion Mechanisms existing at this Potential. Extensive Trenching, Exfoliation like Action and Grain Dissolution are seen. Additionally, Red arrows point to locations where the Fe-Rich Inclusion particle (Al_7Cu_2Fe) is seen to be Dissolving under the Imposed Potential. 51

21. Mechanism of Dissolution of Al_7Cu_2Fe, (a) Example of a Sub-surface Al_7Cu_2Fe particle that was Sectioned using FIB Milling. Curtaining Effects visible on the cut surface due to Uneven open surface above. (b) High Magnification image of one edge of the particle that shows Directional Dissolution. (c) Schematic of Remnant Al_7Cu_2Fe particles Dissolution to leave behind Cu Clusters and Pores. 53

22. Size Distribution of Resolvable Precipitates observed using the SEM. Precipitates below 40 nm could not be Resolved during the TXM Experiment. 59

23. Procedure involved in the preparation of micropillars from rods of AA 7075 61

Figure Page

24. (a) Micropillar of AA 7075-T651 and (b) Micropillar of Highly Overaged AA 707562

25. Schematic showing the components of the Beamline at APS 32-ID-C..... 63

26. The Alternate Immersion Experiment involved Scanning the Specimen using the TXM and Corrosion of the Pillars by using a Custom made Setup for Immersion. 64

27. Comparison between As Reconstructed Slice vs the Same Slice Filtered..... 66

28. A Comparison of the Peak Aged and Highly Overaged Pillars Before and After Corrosion documented using the SEM..... 68

29. Virtual Slice Cross Section of the ST plane showing Progress in Corrosion Damage with Immersion time (0, 1, 3 and 5 hours). Blue Arrows show the Al_2CuMg Particle, Green and Yellow Arrows show an Fe-Rich Inclusion Particle. 69

30. Evolution of Localized Corrosion around the Fe-Rich Inclusion Cluster from Figure 29. Inclusion Volume is seen to be Relatively Constant while the Amount of Corrosion Product is measured to Increase Linearly. The Dissolution Model Proposed by Metzger and Zahavi are Improved upon using Observations from this Particle..... 70

31. Example of corrosion damage seen in highly overaged specimens along the ST plane. Yellow arrows show example locations of initiation of intergranular corrosion at grain boundaries indicating significant trenching around these particles..... 72

32. Another example of corrosion damage observed in highly overaged specimens along the ST plane. Fe-rich inclusion particle is observed not play as important a role in this specimen compared to the precipitates..... 74

33. SEM Image and Corresponding IPF and Grain Boundary Misorientation Maps for a Serially Sectioned Slice of a Highly Overaged Pillar. Intergranular Corrosion Preference is abundantly clear with the High Angle Grain Boundary (blue dotted line) corroding diametrically through the Pillar. Low Angle Grain Boundaries (green dotted lines) selectively undergo Intergranular Corrosion..... 75

34. Schematic showing the Geometries of the AA 7075-T651 plate and Ti-6Al-4V screw (All dimensions in mm) 82

35. Microstructure of the AA 7075- T651 Plate showing Metallic Inclusions and Dispersoids Oriented along the Rolling Axis of the Plate. 87

36. Vertical Cross Section of the AA 7075-T651 Plate and Ti-6Al-4V Screw. a) As Reconstructed Tomography Dataset b) Dataset after Anisotropic Diffusion c) Dataset after Anisotropic Diffusion + Unsharp Mask. 88

37. Evolution of the AA 7075 Microstructure with Increase in Corrosion Time. (a) Formation of Pits on the AA 7075 Plate during the Corrosion Experiment. (b) Pits only around the Threading of the Plate. (c) Plots of Surface area of Pits, Volume of Pits and Number of Pits as a function of Corrosion Duration. 89

38. Visualization of Fracture Surfaces. (a) Angled View of the Fracture Surface. (b) Top Down View of the Fracture Surface showing Three regions A, B and C for each half. 92

39. Fatigue Crack Initiation Sites, (a) (b) (c) Crack Initiation Sites showing the Presence of Crack Initiating Pit Clusters. 93

Figure Page

40. Pit from Crack site 2 showing the Presence of Corrosion Product within the Pit and signs of Crack Propagation ahead of it. 94

41. Crack Initiation site 1. (a) Large FOV Low Magnification image of ROI, (b) Stitched Image of Crack from Initiation to Fast Fracture, (c) Crack initiation site- 2 pits with an Fe Rich Metallic Inclusion, (d) River Patterns ahead of the Initiation Site, (e) Fast Fracture characterized by the Presence of Dimples. Black Arrow at the Bottom of the Figures specifies Direction of Crack Growth. 95

42. Crack Initiation Site 2, (a) Large FOV Low Magnification Image of ROI, (b) Crack Initiation Site Highlighting the Two Regions in Red and Green boxes, (c)(d)(e) Region 1- Three Pit Cluster(yellow box) and the Striations(blue box) ahead of the Pits, (f)(g)(h) Region 2- Single Pit (yellow box) and the Striations (blue box) ahead of the Pit. Black arrow at the Bottom of the Figures specifies Direction of Crack Growth. 97

43. Crack Initiation Site 3, (a) Large FOV Low Magnification Image of ROI, (b) Higher Magnification Image of the ROI Highlighting Crack Initiating Pits, (c) Stitched Image of a Crack Initiating Pit(yellow box) and the Adjacent Si-Rich Inclusion Particle + EDS map, (d) Image of the other Crack Initiating Pit (brown box) showing Cu and Fe-Rich Inclusion Particle Remnant + EDS map, (e) Higher Magnification Image of the Green box from (b) showing Striations ahead of the Crack Initiation Site. Black arrow at the Bottom of the Figures Specifies Direction of Crack Growth. 98

44. Top Down View of one Fractured Surface Highlighting Crack Initiation Site locations. 101

45. Crack Initiation Site 1 Traceback, (a) Fractured Halves of the Specimen Highlighting the Crack Initiation Site(white box), (b) The same Slice from the Dataset captured after 20 days of Corrosion highlighting Site 1(red box) and Pits in the slice with Yellow Arrows, (c) The same Slice with the ROI highlighted in green, blue, black and yellow boxes for the 15 days, 10 days, 5 days and 0 days datasets, (d) Schematics showing the ROI from Pristine Microstructure to 20 days showing the Fallout of Inclusion Particles during the Trenching and Pitting Process. 102

46. Crack Initiation site 2 Traceback, (a) Fractured Halves of the Specimen Highlighting the Crack Initiation Site(white box), (b) The same Slice from the Dataset captured after 20 days of Corrosion highlighting site 1(red box) and Pits in the slice with Yellow arrows, (c) The same slice with the ROI highlighted in green, blue, black and yellow boxes for the 15 days, 10 days, 5 days and 0 days datasets, (d) Schematics showing the ROI from Pristine Microstructure to 20 days showing the Fallout of Inclusion Particles during the Trenching and Pitting Process. 104

47. Crack Initiation Site 3 Traceback, (a) Fractured Halves of the Specimen Highlighting the Crack Initiation Site(white box), (b) The same Slice from the Dataset captured after 20 days of Corrosion highlighting site 1(red box) and pits in the slice with yellow arrows, (c) The same slice with the ROI highlighted in green, blue, black and yellow boxes for the 15days, 10 days, 5 days and 0 days datasets, (d) Schematics showing the ROI from Pristine Microstructure to 20 days showing the Fallout of Inclusion Particles during the Trenching and Pitting Process. 106

Figure Page

48. Schematic Showing the Geometries of the (a) AA 7075-T651 plate and (b) Ti-6Al-4V Rivet (All dimensions in mm) 115

49. Schematics Showing the Two Types of Specimens designed for this Experiment. Type A was Exposed on All surfaces to the Corrosive Fluid while Type B was Exposed only on the Face containing the Head of the Rivet. 118

50. (a) Beamline Setup at 2-BM, APS, Argonne National Laboratory, (b) Loading Fixture that was used to conduct the *In situ* Corrosion Fatigue Experiments. 119

51. Example of Segmented Crack Growth in a Type A Specimen. The Crack is observed to start near the Tail of the Rivet in the Aluminum Plate and Grow as a Quarter Elliptical Corner Crack. 122

52. 2D Slice of the LT Plane showing the Dominant Crack from Figure 51. Also seen are a host of other damage Mechanisms acting simultaneously, such as Secondary Cracks, Pitting with a preference along the L direction and Intergranular Corrosion. 123

53. Type B Specimen (a) Dominant Crack 44 Cycles before Specimen Failure on the left side of the Rivet, (b) Dominant Crack 44 cycles before Specimen Failure on the Right side of the Rivet. 124

54. Segmented Top View of the Type B Specimen from figure 53 showing Crack Initiation and Growth with Increase in Corrosion Fatigue Cycling. Red Arrows point to the Cracks in the AA 7075-T651 Plate (invisible) on both sides of the Rivet. 127

55. Fractography performed on one Fracture Surface of the Type B Specimen whose Segmentation is shown in figures 53 and 54. (a) and (b) show an angled (54 degrees) and Top view of the Fracture surface which was Delineated into surfaces A, B and C. Surface A showed signs of Typical Corrosion Fatigue in the specimen with the Initiation of Pits seen close to the Bore Hole Surface (figure 55(d)). (e) the Paris Regime characterized by the Presence of Striations. (f) Fast Fracture Regime Characterized by the Presence of Dimples. And (g), Surface B characterized by Excessive Intergranular Corrosion and Pitting..... 128

CHAPTER 1

INTRODUCTION

Aluminum alloys are used extensively in a variety of applications ranging from aerospace to naval applications. These alloys are strong, light, and can be produced very economically. Different series of alloys have been developed till date and are used in different applications depending on their individual properties. The focus of this research is on Aluminum 7XXX alloys, specifically AA 7075. This alloy has been the work horse of the aviation and naval industry for multiple decades and its behavior and properties have spurred the development of many new alloys. The alloy is composed of alloying elements such as Zn, Mg, Si and Cu, that bring about a significant enhancement in its mechanical behavior. This is achieved through the formation of second phase particles in the alloy, particularly precipitates. These nano-sized particles enhance the strength and hardness of the alloy by acting as barriers to dislocation motion. Additionally, particles such as metallic inclusions (tens of micrometers in size) and dispersoids (hundreds of nanometers to a few micrometers in size) are also formed in the alloy. Each of these particles contribute to the overall performance of the alloy[1,2]. Of interest, are the corrosion and corrosion fatigue behavior of this alloy and how individual constituent particles contribute to the alloy's global behavior. Decades of research have indicated that damage in these alloys are broadly dictated by three global parameters, namely the mechanical effects, the microstructural effects and the electrochemical effects[3,4]. The mechanical effects pertain the nature of mechanical stresses acting on the alloy. The microstructural effects pertain the ageing condition of the alloy, grain size, texture, and alloy cleanliness (metallic inclusion content).

Lastly, the electrochemical effects pertain the nature of the corrosive environment that is prevalent in the vicinity of the alloy and the potential galvanic effects that can be present between the alloy and another coupled alloy or micro-galvanic coupling between the different constituent particles themselves. Pitting corrosion due to constituent particles and damage at fastener bore holes are some of the most common forms of damage experienced by these alloys [5–9]. In short, owing to the complexity of these phenomena, it can be established that the damage behavior in these alloys is not perfectly well understood. This is corroborated by the fact that corrosion and corrosion related damage costs the US exchequer upwards of 300 billion dollars a year[10,11].

This dissertation focuses studying and improving our understanding of the corrosion behavior of AA 7075 using correlative microscopy-based-workflows[12,13]. The use of labscale corrosion techniques to quantify the corrosion behavior has greatly improved our understanding of the critical factors that contribute to the damage. Chapter 3 in this dissertation focuses on the use of potentiodynamic polarization, a labscale electrochemical method that studies the corrosion behavior under an imposed increasing potential. Combining this with multiple visualization techniques such as non-destructive 3D x-ray tomography and 2D scanning electron microscopy has yielded information pertaining global and local phenomena. In order to study the role of individual second phase particles better, a novel synchrotron x-ray computed tomography technique called Transmission X-ray Microscopy (TXM) was employed and is detailed in Chapter 4. This study documents for the very first time, the observation of corrosion at the nanoscale and in 4D.

Results indicate that the role of precipitates in contributing to intergranular corrosion and inclusion particles in dictating localized corrosion are strongly related to the ageing condition of the alloy.

Another more commonly observed problem in these structures is the initiation of fatigue cracking from fastener holes/ bore holes[7,9,14,15]. These dissimilar metal couple locations act as stress concentrators. Additionally, often the plate is coupled with titanium alloys or steel, both of which are cathodic to the AA 7075 plate. This can lead to localized galvanic and crevice corrosion, thereby making them potential candidate sites for crack initiation. Most studies have utilized post fracture fractography methods to study initiation and propagation of damage owing to the complexity in the geometry and difficulty in studying the same in 4D. The careful use of correlative microscopy-based-workflows can alleviate this issue by using x-ray microtomography in these specimens to track corrosion and cracking damage with time. The combination of lab-scale *ex situ* and synchrotron *in situ* x-ray tomography can yield valuable information regarding initiation sites, microstructural features that are responsible for the initiation of corrosion and cracking and lastly, crack growth behavior. Chapter 5 focuses on studying the corrosion behavior in one such AA 7075 plate / Ti-6Al-4V screw couple. The initiation and growth of pitting corrosion was studied *ex situ*, non-destructively and in 4D using labscale x-ray tomography. Fractography combined with post fracture tomography scans enabled the identification of crack initiation sites. To overcome this process of relying on fractography to identify initiation sites and propagation direction, 4D *in situ* synchrotron-based absorption contrast tomography experiments were conducted on AA 7075 plate and Ti-6Al-4V rivet couples with different area ratios to observe crack initiation and propagation

non-destructively, for the very first time. This helped address questions pertaining pit initiation, crack initiation, crack growth and shape evolution with time.

CHAPTER 2

LITERATURE REVIEW

2.1 Microstructure of Aluminum Alloys

Aluminum alloys are used ubiquitously in a variety of applications due to their high strength to weight ratio and ease of manufacturability. Aluminum is often alloyed with a variety of other elements to improve strength. Manganese (Mn), Copper (Cu), Magnesium (Mg), Zinc (Zn) and Silicon (Si) are the most common alloying elements added to aluminum to form a series of alloys that can be used for specific applications. Specifically, with regard to wrought alloys, a four-digit numerical system is designated to address and identify the alloy. 1XXX series of aluminum alloys contains no alloying elements, 2XXX series of alloys contain Cu as their primary alloying element, 3XXX series contain Mn, 4XXX contain Si, 5XXX contain Mg, 6XXX contain Mg and Si, 7XXX contain Zn and Mg and 8XXX contain Li. Among these, the 2XXX, 6XXX and 7XXX alloys can be precipitation strengthened using a variety of heat treatments in order to drastically improve mechanical properties such as hardness and strength[1,2].

The alloy of interest in this dissertation is AA 7075, a legacy 7XXX alloy that is widely used in industry. AA 7075 is generally composed of Si (0.4 wt.%), Fe (0.5 wt.%), Cu (1.2-2.0 wt.%), Mn (0.3 wt.%), Mg (2.1-2.9 wt.%), Cr (0.18-0.28 wt.%), Zn (5.1-6.1 wt.%)[16]. As a result of adding these elements, specific second phase particles form throughout the matrix of the alloy. Moreover, these size and distribution of these particles is strongly dictated by the production and heat treatment operations performed on the alloy. Constituent particles in AA7XXX can be specifically of three types: metallic inclusions,

dispersoids and precipitates. Inclusions are unwanted second phase particles present in notable quantities in the alloy and are primarily composed of Fe and Si. AA 7075 contains Fe-rich inclusions and Si rich inclusions that can total up to 1.63 % by volume[17]. Newer versions of AA 7XXX such as AA 7475 can contain fewer inclusions by volume and show 40% greater fracture toughness[18,19]. Interestingly, during forming methods such as rolling, these metallic inclusions can form stringers oriented in the direction of rolling and can be tens to hundreds of microns in length along the rolling axis (L direction) and a few tens of microns along the other two orthogonal directions (T and S directions). Due to the fact that they are harder than the aluminum rich matrix, they can also crack during rolling[17,20]. Dispersoids are deliberately formed in the alloy in order to be able to control the grain size and recrystallisation[1,21,22]. These dispersoids can range in sizes of a few hundreds of nanometers to sub 10 μm. Lastly, nano sized precipitates are present in the bulk matrix as well as grain boundaries of the alloy and are responsible for contributing to increasing the strength and hardness of the alloy[23,24]. The chemical composition and morphology of precipitates changes as per the ageing condition. Precipitation in AA 7075 follows the following sequence with ageing time- Super saturated solid solution (after solution treatment and quenching) → GP zones (underaged) → η' (peak aged)→ η (overaged)[25]. The precipitates are responsible for resisting slip of dislocations. As GP zones, their ability to hinder dislocation movement is very limited. On ageing to peak aged condition, the particles strengthen and TEM studies have shown that the particles are semi-coherent with the adjacent matrix lattice. This contributes to increased interfacial energy and misfit stress around the particle. At this point, dislocation- precipitation interactions involve precipitate shearing. On continued ageing, the precipitate- matrix interface

becomes incoherent and interfacial energy and misfit strains become minimized. The spacing between precipitates increases so much that the dislocations can now bow between the precipitates, thereby beginning to reduce strength once again[23,24,26].

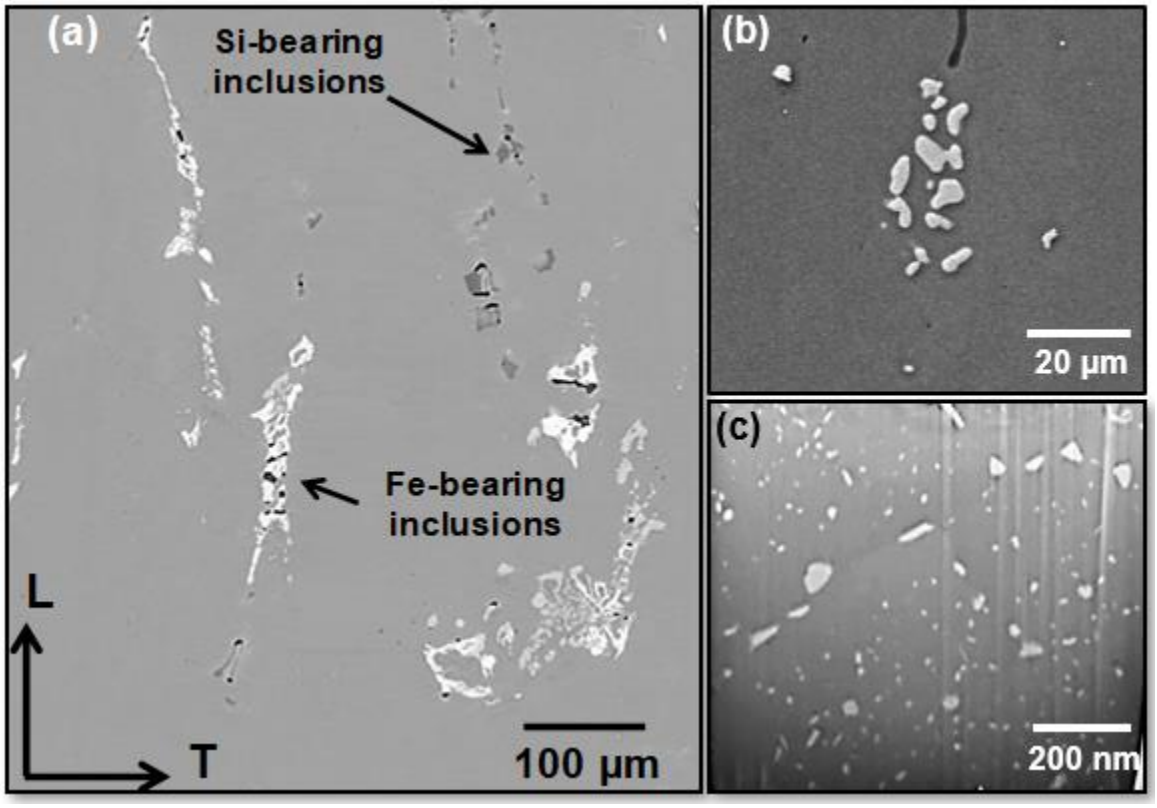

Figure 1: Microstructure of AA 7075- T651, (a) Metallic inclusions [17] , (b) Dispersoids, (c) Precipitates.

Figure 1 shows examples of metallic inclusions (figure 1(a)), dispersoid particles (figure 1(b)) and precipitates (figure 1(c)). In service, aluminum alloys are exposed to harsh environmental conditions such as in aircraft or naval structures, where they are most often used. These structures are constantly under imposed external mechanical stresses and corrosive environments involving saltwater or moisture[6,7,9]. Despite the many advantages of having these microstructural constituent particles on multiple length scales,

aluminum alloys, especially AA 7075 is highly susceptible to a host of structural problems such as pitting corrosion. The Fe-rich inclusions are particularly seen to be responsible for assisting in localized pitting corrosion by acting as local cathodes[22,27–29]. Additionally, the alloy is particularly susceptible to Stress Corrosion Cracking (SCC) and Corrosion Fatigue, both of which are responsible for catastrophic failures associated with the alloy[4,28,30–32]. Both phenomena require the presence of an external mechanical stress (monotonic for SCC and cyclic for corrosion fatigue) and the presence of a corrosive environment. The mechanisms that have been proposed to lead to these failures are directly related to the nature and distribution of second phase particles. Furthermore, the formation of pitting corrosion can severely affect the SCC and corrosion fatigue lives as these pits can act as effective stress concentrators and assist in crack initiation and propagation. Designing structures that utilize these alloys can be a challenge and often a 2 – 2.5 knockdown factor is used to account for corrosion related effects[8,33]. However, this can either be dangerous as it could lead to over-designing or under-designing. Additionally, considering that corrosion and corrosion related damage to weapons systems accounted for over 18 billion dollars annually as of 2014 (according to US Dept Of Defense)[14], it is of critical and immediate importance to be able to analyze and have the capability to predict corrosion related damage before and monitor the same during service.

2.2 Corrosion Studies on AA 7075

Decades of work have led to significant strides in the area of corrosion testing, mechanical testing and the combination of two. With regard to studying corrosion damage, a number of tests have emerged that attempt to replicate in service conditions in some form or another. Corrosion tests such as salt spray, continuous immersion, alternate immersion,

weight loss measurements, electrochemical methods etc. have emerged as viable techniques to study the corrosion behavior of alloys[34–36]. Combining these with characterization techniques such as optical, electron, x-ray or electrochemical microscopy is useful in identifying local and global corrosion damage behavior. Among these, potentiodynamic polarization is a widely used electrochemical method. It involves imposing the specimen of interest to a dynamically increasing potential and tracking the current response. The technique is unique in that it provides the user with a reliable and reproducible method to estimate the corrosion current, corrosion potential, corrosion rate and hence, life prediction[34]. Due to the speed at which results can be obtained via this technique, many different material systems can be studied in various corrosive environments and compared with one another with ease. This process is often preceded with an open circuit potential estimation where the corrosion potential of the specimen is estimated with time and no externally applied potential. The open circuit potential estimation gives an idea of the specimen's approach to steady state corrosion behavior. With time, the rate of change of the potential reduces and the potential settles within a short range of values. Following this, the potential is increased from a starting pre-determined value of the potential that is more negative compared to the open circuit potential and is increased at a scan rate that can be determined by the user based on trial experiments. A slower scan rate has been observed to yield significantly more reliable estimate of the breakdown potentials[37,38]. Higher scan rates are seen to overestimate breakdown potentials and distort the entire polarization curve leading to incorrect interpretations. Polarization scans comprise of an anodic polarization curve and a cathodic polarization curve. The reversible or rest potential is the potential value in the curve where the sum of

the anodic reaction rate and cathodic reaction rate is close to zero and this is reflected in the current value. Above this potential, the anodic reaction is dominant and leads to specimen oxidation and hence is called the anodic polarization curve. Below this potential, the cathodic reaction is dominant and reactions such as oxygen reduction are observed more and is called cathodic polarization curve[34].

The corrosion behavior of pure aluminum has been studied quite extensively. Although Al contains a persistent oxide film that protects it from corrosion, it has been observed that pitting is primarily seen in solutions containing Cl^- ions. The pitting behavior in pure Al has been broadly divided into four categories: processes occurring at the passive film and processes within the film are detailed by adsorption mechanisms[39–41], penetration mechanisms[39,42–44] and film breakage mechanisms[45,46]. In short, chloride ions can get adsorbed on to the passive layer, penetrate into the passive film and weaken it internally leading to its breakage and hence assist in the interaction of the fresh metal with the fluid. Following this, processes between the film and bare metal lead to metastable pitting and finally stable pitting[47–49]. The presence of precipitates, inclusions and dispersoids means that the local passive film in the vicinity and on the particles has poor native oxide coverage or is not present. In fact, an empirically derived size of 3 nm of intermetallic particle size was calculated, below which the native oxide can protect the matrix and above which they oxide layer will be compromised and corrosion can initiate[50]. This makes regions in close proximity to the particles particularly susceptible to localized corrosion attack. The oxidation and reduction reactions pertaining corrosion of aluminum can be found elsewhere[49].

Potentiodynamic polarization has been utilized to study AA 7075 quite extensively. Maitra and English were the first ones to report on the potentiodynamic polarization behavior of AA 7075 in saltwater solution[37]. They observed the presence of two breakdown potentials. Breakdown potentials are values of applied potential which show a large increase in measured current for a small increase in applied potential. The first breakdown potential was attributed to intergranular corrosion (due to grain boundary precipitate dissolution) and the second breakdown potential was attributed to pitting corrosion. This was proven wrong when Zn depletion was observed in the grain boundaries[51]. The first breakdown potential was later confirmed to be due to the dissolution of a thin layer of recrystallized material formed due to polishing. TEM studies have shown that this thin layer is also characterized by the presence of nano-sized grains with Zn and Mg segregating at grain boundaries within the layer[52,53]. On dissolution of the thin layer, a few discrete regions of the surface were observed to start corroding in the form of dark spots or localized matrix attack[52–54]. On exceeding the second breakdown potential, there is a clear consensus that the dominant damage mechanism observed is localized pitting corrosion [37,52,54–57].

2.3 Corrosion Fatigue Behavior of AA 7075

The corrosion fatigue behavior of Al7XXX has been studied extensively in the recent decades. Pitting corrosion is responsible for crack initiation under SCC or corrosion fatigue conditions. Under externally applied stresses, pits act as local stress concentrators and aid crack initiation[14,58–61]. Two main mechanisms have been proposed to explain corrosion fatigue behavior on the microstructural level- anodic slip dissolution and hydrogen embrittlement[62].

Anodic slip dissolution involves the rupture of the oxide formed either on the wake of the crack or crack tip under the applied load, dissolution of fresh matrix at slip steps or PSB's, nucleation and growth of oxide on the surface, further transport of corrosive fluid into the crack. On the other hand, hydrogen embrittlement involves the transport of water molecules or the hydrogenous medium to the crack tip, reduction and release of hydrogen at the tip due to corrosive attack of the specimen, adsorption of the hydrogen formed to locations within the tip such as dislocation cores, grain boundaries or precipitates (a percentage of the hydrogen is released in the form of hydrogen bubbles) and finally, easing crack propagation by enhancing local plasticity and/ or enhancing dislocation emission. The effect of mechanical loads applied, and the corrosive medium is prominent here. Increasing solution aggressivity (lower pH for example) can lead to more surface oxide removal, expose new matrix to the fluid, exacerbate corrosion fatigue reactions and increase crack growth rates significantly[63–65]. Additionally, it is also seen that lower loading frequencies during corrosion fatigue in a corrosive medium can lead to increased influence of the chemical species at the crack tip i.e more time for oxidation to occur and aid hydrogen release into the material. Loading ratio (R ratio) or the ratio of minimum applied stress to maximum applied stress is seen to play a role as well. Higher R ratios implies that the threshold ΔK for corrosion fatigue approaches the threshold ΔK for SCC[4,62]. Mechanistically, lower R ratios allow the corrosive species to spend more time at the crack tip continuously. The presence of a constant load (as R ratio increases up to 1) ensures that new material for oxidation and hydrogen release are available and hence exacerbates damage significantly.

The presence of an external mechanical load at the tip of corrosion pits ensures corrosion product breakage and exposes new material to the corrosive fluid, thereby enhancing the processes mentioned above. Therefore, pits are seen to be favorable features for crack initiation. In AA 7075 and in the absence of a corrosive environment, hard Fe-rich inclusion particles in the matrix are seen to be favorable sites for crack initiation as they contribute to local stress concentration [20,66–70]. Under a corrosive environment, these inclusion locations act as favorable sites for pit initiation as they behave cathodically in neutral or acidified saltwater solutions[27,28,58,71,72]. Following this, cracks initiate and are often seen to coalesce with time and aid in specimen fracture. The effect of hydrogen embrittlement is seen ahead of the crack tips in terms of flat surface features indicating hydrogen ingression and easing of transgranular crack propagation[32,65,73,74]. In the Paris regime of the crack growth, corrosion fatigue manifests in the form of brittle striations. Brittle striations have striation spacings which are larger than its ductile counterpart (in air) and the surface is significantly more rugged.

Often, corrosion and fatigue cracking are observed to initiate at or in close proximity to fastener holes, where the aluminum plates are in contact with the fasteners. These fasteners are often made of steel or titanium alloys and are electrochemically cathodic to the aluminum alloy in moisture or salt-water environments. This makes mating surfaces highly susceptible to a combination of galvanic and crevice corrosion. This situation is further exacerbated by the fact that aluminum alloys contain various types of intermetallic particles which contribute to localized corrosion damage in a variety of ways depending on their composition and the alloy's aging condition. Additionally, these fastener-plate joints are subject to complex stress states that vary depending upon whether an aircraft is parked or

is in flight. Such dynamic fluctuations in stress can potentially damage surface protective coatings around the fastener, which can in turn create a localized corrosive environment and nucleate corrosion pits and fissures. Micro-crevices between the fastener and plate can lead to the trapping of films of electrolyte, thereby exacerbating localized corrosion and leading to crack propagation during flight [8] (Figure 2). In short, the combined presence of a corrosive environment and external mechanical load makes studying damage in such dissimilar alloy couples a complex multi-disciplinary challenge.

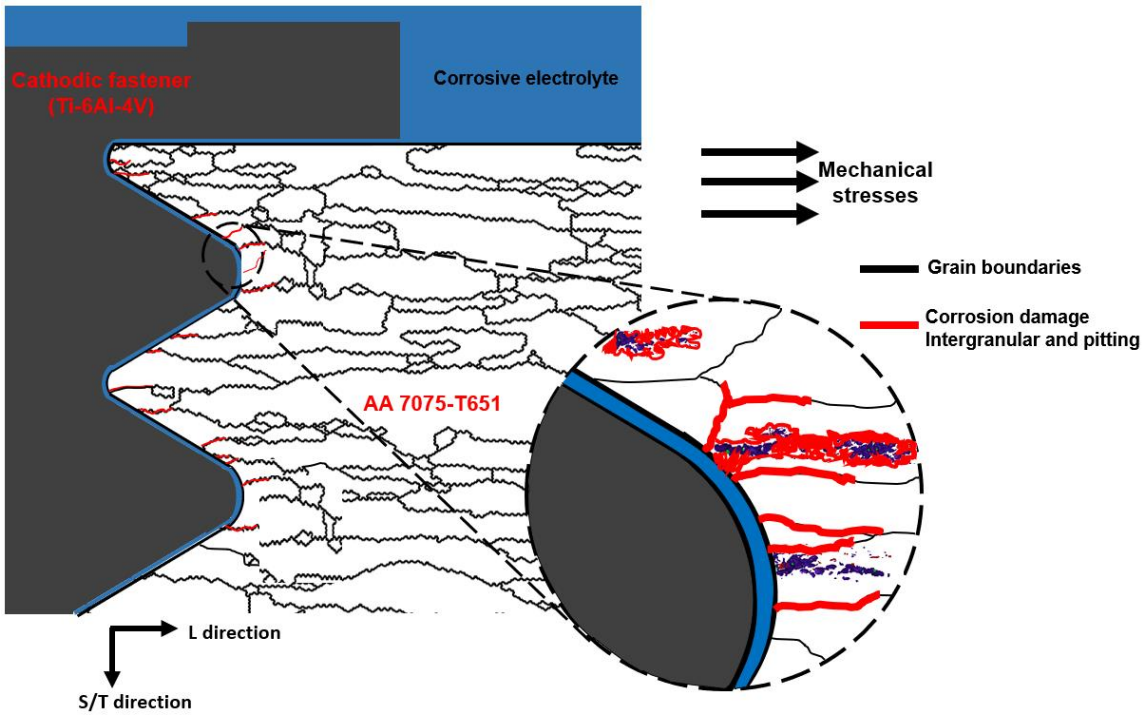

Figure 2: Schematic showing the conditions prevailing within faster- plate couples and the locations and propagation path of corrosion damage.

2D surface characterization and analysis techniques are extremely valuable as they have helped the progress of a multitude of scientific fields up until now. Techniques such as optical microscopy, Scanning Electron Microscopy (SEM), Energy Dispersive

Spectroscopy (EDS) and Electron Back Scatter Diffraction (EBSD) are of particular interest to this dissertation. However, the amount of sub-surface information that can be obtained from this technique is severely limited. Furthermore, most natural phenomena, including corrosion of material systems, although start off as 2D processes, manifest into 3D phenomena.

This can severely limit the insights that can be obtained pertaining the characterization of damage initiation, propagation mechanisms and quantification of the same. Moreover, extrapolating observations made in 2D to make conclusions in 3D can lead to incorrect or even dangerous consequences[71,72]. For example, studies of the initiation and growth of cracks by purely observing the specimen's surface can grossly underestimate sub-surface damage and lead to incorrect alloy performance predictions and prognosis. Moving forward, it is thus quintessential to include some form of 3D characterization that involves observation of sub-surface phenomena.

Destructive techniques in the study of sub-surface material behavior have gained immense popularity over the past few decades. Serial sectioning processes that involves manual/automatic mechanical polishing have been used to map the microstructure of material systems of small volumes, often involving a few tens of iterations[75–77]. Focused Ion Beam (FIB) milling is another excellent technique that can be used to mill and machine specimens at the microscale and also be used to map the microstructure at the nanoscale. Latest developments in laser FIB techniques can also mill materials in the size range of a few hundred of micrometers[78]. Trenches, micropillars, beams and other geometries can be milled to a very high degree of dimensional accuracy (few nanometers).

Moreover, these can be followed up with either microstructural characterization or mechanical behavior studies or both.

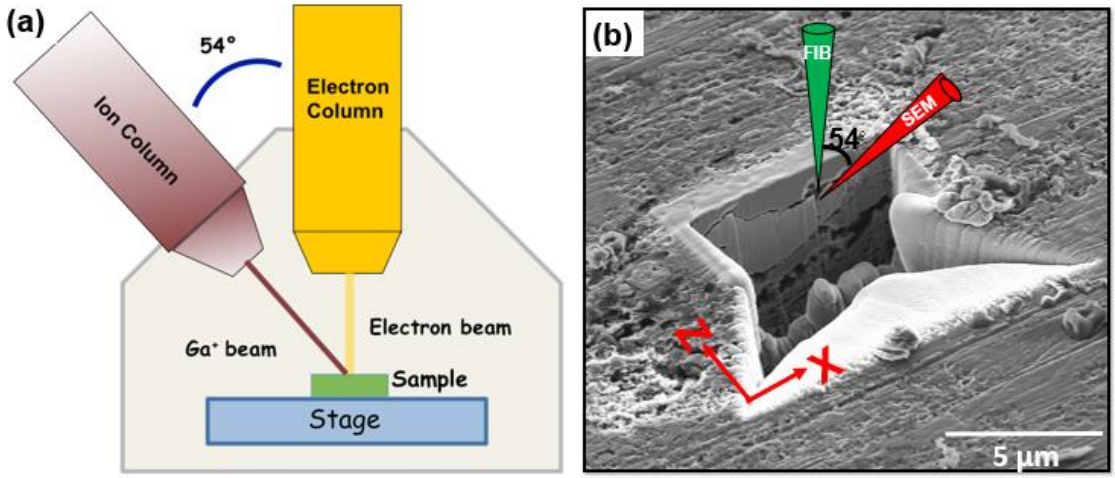

Figure 3: (a) Schematic of the Focused Ion Beam- Scanning Electron Microscope, (b) Schematic of the serial sectioning nano-tomography procedure.

In FIB based techniques, the specimen of interest is tilted to an angle of 54 degrees with respect the x-axis of the stage. Often, the FIB source, most commonly Ga+ (newer FIB sources include neon and argon ions[79–81]) and the electron beam are aligned such that the region of interest is in focus. The milling geometry can be controlled with a host of options ranging from a simple trench to more recently, having the ability to enter milling recipes that the FIB can follow to mill out the final specimen, such as in TEM specimen preparation. The milling rate, slice thickness and finish can be controlled by the careful use of appropriate milling currents, with smaller currents yielder better and cleaner surface finishes. Interestingly, the FIB and electron beam imaging can be combined and alternately used to mill and image the material. This destructive serial sectioning nano-tomography approach yields a stack of images that can be used like any tomography dataset and obtain

microstructural information in 3D[82–84]. However, the biggest shortcoming with regard to destructive techniques is that they are destructive in nature. Additionally, they are expensive, time consuming and can only analyze a small volume of material. Furthermore, 4D and *in situ* experiments cannot be performed because of the destructive nature of the technique. In summary, there is a need to nondestructively map the microstructure of large volumes of material.

X-ray computed tomography has proven to be an excellent suite of techniques to study specimens in a variety of fields including biology, geology and materials science. X-ray tomography is unique because it helps visualize and study materials non-destructively at high spatial (synchrotron ~20 nm and labscale ~0.8 μm resolutions) and temporal resolutions and in 3D. Synchrotrons all over the world offer an array of techniques that can map the microstructure of the specimens of interest very comprehensively from compositional imaging such as absorption based imaging such Absorption Contrast Tomography and Transmission X-ray Microscopy (TXM), diffraction based imaging techniques such High Energy Diffraction X-ray Diffraction Microscopy (HEDM) and Diffraction Contrast Tomography (DCT), spectroscopy, scattering (Small angle and Wide angle) etc [17,28,58,65,70,85–88]. Of particular interest to this dissertation are the Absorption based techniques i.e Absorption Contrast Tomography and Transmission X-ray Microscopy. Regardless of the technique used, x-ray techniques comprise of a source, specimen stage and detector system. The specimens are rotated over a pre-determined angular range (mostly 0-180 or 0-360). During this, x-rays from the source pass through the specimen and hit the detector. In Absorption Contrast Tomography techniques, the intensity values obtained on the detector are directly dependent on the source intensity and

the nature of the material being scanned and follow the Beer-Lambert law[84,89]. A few commercial x-ray microscope manufacturers have recently also started manufacturing x-ray tomography machines for labscale tomography purposes. Techniques such as absorption contrast tomography and diffraction contrast tomography can be performed in experiments, particularly where time is not a constraint (such as alternate immersion corrosion experiments) without visiting synchrotrons, which are often very high in demand and provide limited beam time[90–93].

Tomography techniques are excellent methods to study corrosion initiation and cracking phenomena. Traditionally, studying crack initiation and growth in such specimens has proven to be challenge. The absence of information pertaining pitting corrosion within such a complex geometry can be very limiting. But absorption contrast tomography can alleviate this problem and help identify precise crack initiation locations and crack growth trends. An overarching theme of the studies performed as a part of this dissertation is the use of correlative microscopy-based approaches to study damage phenomena. Correlative microscopy involves studying a microstructural phenomenon with two or more different imaging modalities so as to obtain different microstructural and phenomenological insights over multiple length scales[12,13]. Often this approach involves utilizing extensive image registration operations to probe specific parts of the microstructure. In this dissertation, a combination of tomography techniques and electron microscopy have been employed to study corrosion damage phenomena. The advantage of using such an approach is that multiple modalities of information can be obtained from the same sample. Developing and executing correlative microscopy workflows that combine x-ray tomography and other techniques enables the experimenter to analyze specimen by targeting specific regions in

the microstructure, thereby enabling comprehensive microstructural analysis. For example, x-ray tomography can be used to non-destructively scan a specimen and choose within it, a region of interest. Following this, using careful registration operations, the FIB-SEM can be used to perform a variety of operations such as mill into the material in that region of interest and perform microstructural characterization such as with EDS and EBSD.

Based on the introduction and literature review presented above, the objectives of the research are as follows:

1) To study the microstructural evolution of AA 7075-T651 subjected to accelerated corrosion in a saltwater environment using potentiodynamic polarization and correlative microscopy.

2) Thoroughly inspect the role of second phase particles in initiation and propagation of corrosion damage mechanisms in AA 7075-T651 and highly overaged AA 7075 using Transmission X-ray microscopy.

3) Investigate the evolution of pitting corrosion in AA 7075-T651 plates coupled with Ti-6Al-4V screws using *ex situ* lab scale x-ray computed tomography. Additionally, investigate the crack initiation and growth mechanisms in the same under corrosion fatigue.

4) To study the *in situ* crack initiation and propagation mechanisms from corrosion pits in an AA 7075-T651 plate with a Ti-6Al-4V rivet using synchrotron x-ray tomography.

CHAPTER 3

MULTISCALE INVESTIGATION OF DAMAGE INITIATION AND PROPAGATION DURING CORROSION OF AA 7075-T651 USING CORRELATIVE MICROSCOPY

3.1 Introduction

The corrosion and mechanical behavior of aluminum alloys is strongly dictated by the chemical composition, size and distribution of intermetallic particles in the matrix. Electrochemical techniques are ubiquitously used in industry as well as research laboratories to study material performance under a variety of environments. Among these, potentiodynamic polarization is used to extract intrinsic parameters that describe the corrosion behavior of the test specimen such as corrosion potential, pitting potential, corrosion current, corrosion rate etc. It is important to note that given a clearly defined Region of Interest (ROI), these parameters provide a global response of the material to the imposed corrosive conditions. This is critical since it can assist with rapid material selection and testing, imposition of a variety of environments to study material behavior and finally, life prediction[34]. However, in aluminum alloy systems, in addition to the global corrosion behavior, it is also vital to consider the contribution of microstructural features that contribute to the overall corrosion behavior and alloy performance, such as the grain size and texture[82,91,94,95], size and distribution of second phase particles such as inclusions [17,22,27,67,95–103](correlates to the alloy composition, raw material cleanliness and production practices) and precipitates (correlates to the ageing condition in precipitation hardened systems)[28,82,86,104].

AA7075, which is the alloy of interest in this study, contains a combination of metallic inclusions, dispersoids and precipitates. The metallic inclusions can be either Fe- bearing or Si- bearing. In the presence of neutral saltwater environments, Fe- bearing inclusions are cathodic to the matrix and Si- bearing inclusions are anodic to the matrix[22,27,100,103,105]. Dispersoids are deliberately introduced into the material to aid in grain refinement and are observed to be anodic to the matrix[21,83,106]. Finally, precipitates in peak aged AA7075 are composed of particles ranging in sizes of 10s of nanometers and are composed of Mg $(Cu_xZn_{1-x})_2$ and are anodic to the matrix in a neutral saltwater environment[82,104].

Potentiodynamic polarization has been employed to study the corrosion performance of aluminum alloys in a number of studies. Studies that combine electrochemistry and microstructural analysis until now have focused on either observing the microstructure after a complete polarization scan or interrupting the scans to study the microstructure change during the polarization experiment. The anodic polarization curve of mechanically polished AA7075 contains two breakdown potentials which demonstrate a large increase in recorded current for a small increase in applied potential[37,54,56,107–109]. The first breakdown potential has been associated with the dissolution of an active surface layer formed on the surface of the alloy due to polishing[52,109]. This active layer has been observed to contain nano-sized grains devoid of precipitates. Moreover, the polishing action is said to redistribute Zn and Mg to the grain boundaries of these nano-grains thereby aiding rapid intergranular attack until this surface layer is depleted and the actual bulk matrix of the alloy is exposed. Following this, the second breakdown potential has been observed to occur due to stable pit formation after the breakdown of the passive

oxide film formed after the first breakdown potential[53,56,109,110]. Studies aimed at observing the evolution of corrosion damage in aluminum alloys have included a combination of *ex situ* and *in situ* tests. Holroyd performed *in situ* time lapse optical microscopy during the potentiodynamic polarization studies on AA 7XXX alloys and observed hydrogen bubble formation, surface blistering and stable pit formation as the pitting potential was achieved[57]. Pitting corrosion is also accompanied by the presence of intergranular corrosion. Potentiostatic tests conducted at potentials in between the first and second breakdown potentials for extended periods of time has been shown to lead to shallow intergranular corrosion[53]. Liu et. al studied global corrosion behavior of AA 7075-T6 and observed signs of surface dissolution at a potential below the second breakdown potential[54]. Single polarization scans to study pitting behavior in several aluminum alloys including AA7075-T6 indicate that both breakdown potentials increase with increase in alloy ageing time[109,111,112]. Andreatta reported the formation of sub-surface exfoliation corrosion in addition to intergranular corrosion after the second breakdown potential in AA7075-T6 exposed to acidified (pH=4) 3.5 wt.% NaCl solution. It was also hypothesized that intergranular corrosion tends to turn into exfoliation corrosion due to the high susceptibility of grain boundaries (containing high density of $MgZn_2$ precipitates) to intergranular corrosion[56,108,113].

Several studies have also successfully characterized the electrochemical behavior of individual constituent particles commonly found in AA7075. Most of these techniques involve creating large enough specimen of the phase of interest and the use of a microcell technique to study particle corrosion behavior. Fe-rich inclusions for example have been observed to cause the matrix around them to preferentially dissolve without undergoing

dissolution themselves[27,59,100]. Mg_2Si inclusions undergo preferential dissolution of the Mg to leave behind SiO_2[103,105].

While pitting and corrosion damage start off as surface phenomena, increased exposure to corrosion media or increased intensity of attack due to applied potential can manifest in the form of sub-surface damage that can span 10s and possibly even 100s of μm in depth. Previously, sub-surface damage was studied using polishing techniques. However, the number of such regions that can be sampled is severely limited due to the difficulty involved in specimen preparation. Additionally, cross sectioning is a destructive process, prevents the experimenter from sampling specific pits of interest or multiple pits one after another and hence could potentially incorrectly estimate the magnitude of sub-surface damage[114].

Absorption Contrast x-ray Tomography (ACT) has emerged as an excellent technique to non-destructively probe a material at a high resolution in 3D. ACT circumvents these issues by aiding in the non-destructive visualization of sub-surface damage over large areas of the material. In the last decade, ACT has been increasingly gaining popularity in studies focusing on corrosion and cracking behavior in aluminum alloys[17,58,59,65,115–120]. The technique is especially well suited to study sub-surface corrosion phenomena such as intergranular corrosion, exfoliation corrosion and particle dissolution. The release of hydrogen bubbles can also be captured quite effectively using ACT, which can in turn be used to calculate the rate of particle dissolution[103,121]. Using a correlative microscopy-based approach, pitted regions in the specimen can be observed at a high resolution using the ACT and further investigated at smaller length scales by combining the data with targeted Scanning Electron Microscopy (SEM) based techniques such as destructive

Focused Ion Beam (FIB) milling or non-destructive Energy Dispersive Spectroscopy (EDS) and Electron Back Scattered Diffraction (EBSD)[13,28,90,122,123].

The aim of the present study is to thoroughly characterize the microstructural evolution of AA 7075-T651 in the presence of an externally applied increasing potential during the process of potentiodynamic polarization. Owing to the complexity and the speed of microstructural evolution during the scan, specimens were subjected to *ex situ* interrupted tests where the polarization scan was aborted when a predetermined potential was achieved. Each of these interrupting potentials were carefully chosen such that the alloy's behavior at each section of the anodic polarization curve can be analyzed separately. To study the global evolution of the microstructure with increase in applied potential, a correlative microscopy-based approach comprising ACT and SEM were employed to study the microstructural change over multiple length scales, before and after the polarization scan. Additionally, to address the need to further study the effect of microstructural constituents, FIB, EDS and EBSD were extensively used to characterize surface and sub-surface damage associated with metallic inclusions and certain interesting microstructural damage features before and after the scan. The findings address the potential dependent microstructural change on a global scale and additionally, also point to specific local microstructural changes that contribute to the corrosion damage under polarization.

3.2 Materials and Experimental Procedure

1 mm diameter cylindrical rod specimens of AA 7075-T651 were electro-discharge machined from the center of the thickness of a commercially available 25.4 mm thick block (Alcoa, New York, NY, USA) as in figure 1. The longest dimension of the rod specimen

was oriented along the rolling (L) direction. Table 1 shows the chemical composition of the block as provided by the supplier along with tolerances.

Table 1 : Elemental Tolerances (ASTM B209-14) and Measured Chemical Composition of the AA 7075-T651 Block.

AA 7075- T651: Chemical composition(wt.%)									
	Si (max)	**Fe (max)**	**Cu (range)**	**Mn (max)**	**Mg (range)**	**Cr (range)**	**Zn (range)**	**Ti (max)**	**Al**
ASTM B209-14	**0.4**	**0.5**	**1.2–2.0**	**0.3**	**2.1-2.9**	**0.18-0.28**	**5.1-6.1**	**0.2**	**Bal**
Meas-ured	**0.2 ± 0.03**	**0.2 ± 0.04**	**1.5 ± 0.07**	**0**	**2.3 ± 0.03**	**0.2 ± 0.03**	**5.9 ± 0.11**	**0**	**Bal**

The rod specimens were mechanically polished with 600 and 1200-P4000 grit SiC polishing papers. Additionally, the rods were further fine polished down to a 1 µm diamond finish, following which they were thoroughly cleaned with isopropyl alcohol and sonicated to obtain a contaminant free surface. Rubber cement was used to mask out specific regions of the specimen to leave behind an area encompassing a 1 mm height for the relevant study (Figure 4).

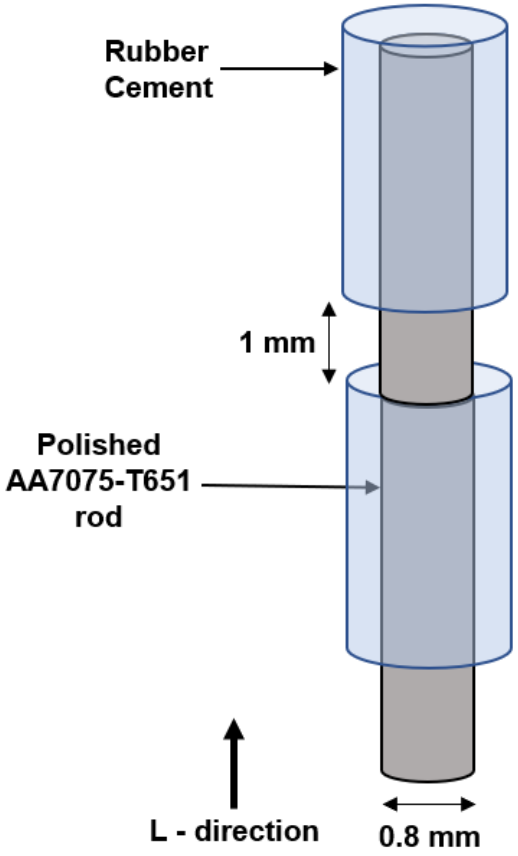

Figure 4: Schematic of the geometry of the cylindrical rod specimen of AA 7075-T651 showing regions covered with rubber cement to expose a ~ 1mm height as ROI.

Potentiodynamic polarization scans were performed using a Gamry Reference 600 potentiostat equipped with a platinum wire counter electrode and a saturated calomel reference electrode in addition to the masked AA7075-T651 rod specimen acting as the working electrode. Each Potentiodynamic polarization scan was preceded by an open circuit potential estimation. Typical duration for this process was 300 seconds, which was adequate for the open circuit potential to stabilize to a value of +/- 30 mV around 730mV. A scan rate of 10 mV/minute was used during all the potentiodynamic polarization tests. Deaerated 3.5wt.% NaCl solution was used as the corrosive medium for all experiments.

Deaeration was performed for a duration of 1 hour by bubbling nitrogen gas into the corrosive medium. Four specimens (excluding replicates at each potential) were subjected to potentiodynamic polarization up to increasing values of anodic potential. Figure 2 shows a schematic of the anodic polarization curve for AA 7075-T651

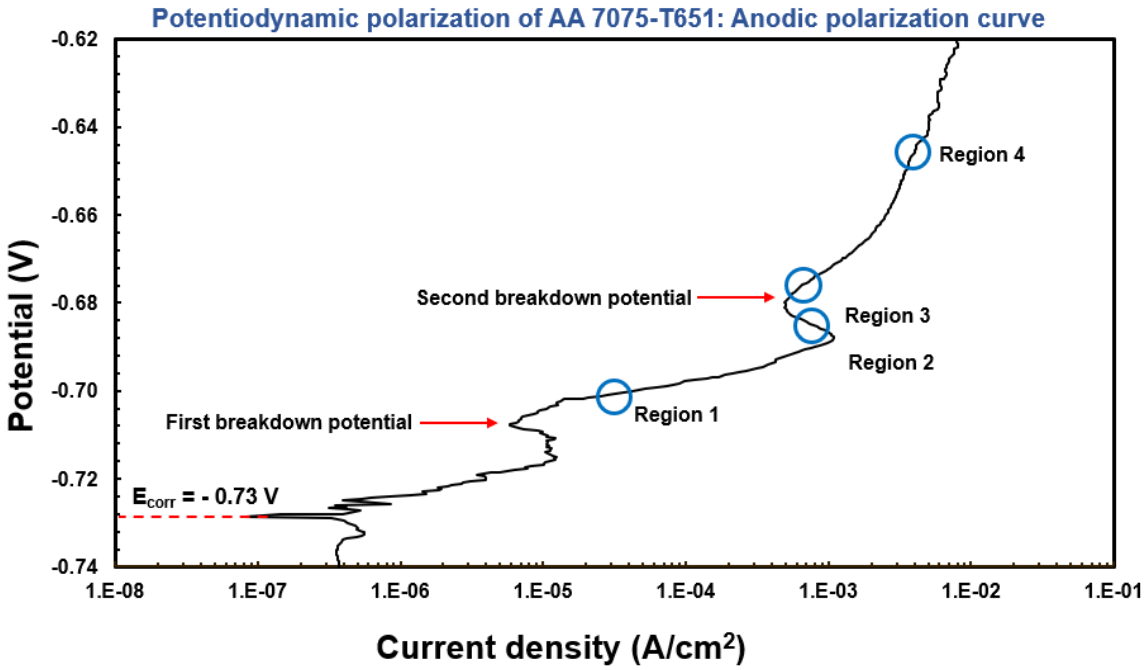

Figure 5. Anodic polarization curve of the Potentiodynamic polarization scan of AA7075-T651 highlighting the four regions at which the scans were interrupted.

For each specimen, the Potentiodynamic polarization curve was started at potential values below the reversible potential of the alloy and terminated at a specific potential in the anodic polarization curve. Figure 5 shows a representative anodic polarization curve on a Potentiodynamic polarization plot of AA7075-T651. Additionally, highlighted in blue circles are precisely the regions where the scans were terminated for each specimen. Specimen 1 was scanned through the reversible potential (E_{corr}) and interrupted at a region immediately ahead of the first breakdown potential, shown as region 1 in figure 2.

Similarly, specimen 2 was terminated at region 2, after the transition potential and immediately before the second breakdown potential. Specimen 3 was terminated at region 3, i.e after the second breakdown potential and specimen 4 was terminated approximately 30 mV beyond the second breakdown potential.

Prior to and after the Potentiodynamic polarization scans, the microstructure of all the specimens was thoroughly characterized non-destructively and in 3D using x-ray microtomography (XCT). X-ray microtomography scans of the region of interest were conducted using a Zeiss Versa 520 x-ray microscope (Carl Zeiss Microscopy Inc. 1 Zeiss Dr. Thornwood, NY). An accelerating voltage of 40 kV was used for all the scans, during which 3201 projections were captured over a stage angular range of -180 to 180 degrees with an exposure time of 10 seconds per projection. A voxel size of 0.95 µm was achieved using the 4X objective lens and a camera binning of 2. Following the scan, the dataset was reconstructed using an in-built filtered back projection algorithm and corrected for beam hardening artefacts. Intermetallic particles and porosities present in the microstructure were registered and used to align the datasets captured before and after the Potentiodynamic polarization scan was performed. A MATLAB (The MathWorks, Inc.) script written in-house was used for the alignment procedure. Visual inspection and comparison of the aligned datasets was performed using ImageJ. A comparison of the two scans (before and after the Potentiodynamic polarization test) yielded information pertaining changes occurring on the surface and sub-surface regions of the specimen in 3D at the millimeter to the micrometer scale.

Additionally, specific regions of the specimens' surface containing second phase particles (metallic inclusions and dispersoids of interest) were visualized and registered in

2D using a Zeiss Auriga FIB-SEM before the Potentiodynamic polarization scan. After the Potentiodynamic polarization scan, the same region was revisited to note structural changes in the microstructure. Energy dispersive spectroscopy (EDS) was used to characterize the second phase particles and to study changes in their composition before and after the terminated Potentiodynamic polarization test. This helped to probe the specimen on the micrometer scale to the nanometer scale. Studying the specimen at this scale helped resolve corrosion damage that could not be visualized using the X-ray microtomography data.

Furthermore, after Potentiodynamic polarization testing, Ga+ Focused Ion Beam (FIB) was used to perform a variety of milling operations at specific second phase particle sites as well as pits to study sub-surface particle morphology, corrosion initiation/progression and pit propagation behavior at the nano scale.

3.3 Results and Discussion

3.3.1 Microstructural Characterization of AA 7075

The AA7075-T651 alloy used in this study comprised metallic inclusions, dispersoids and precipitates distributed throughout the Al rich matrix as in figure 6. EDS was used to confirm the composition of the metallic inclusions to be Fe-bearing (Al_7Cu_2Fe and $Al_{23}Fe_4Cu$) and Si-bearing (Mg_2Si). Further information about the microstructure can be found elsewhere[17].

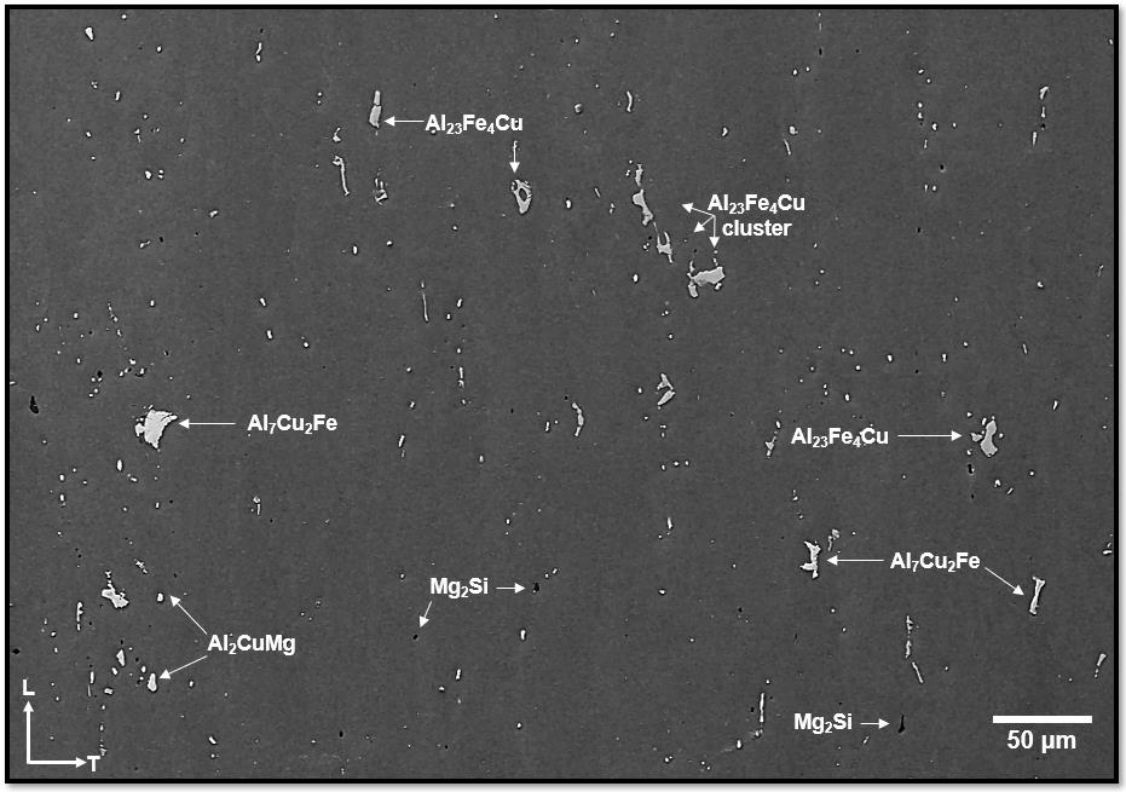

Figure 6: Microstructure highlighting the different constituent particles in the specimen.

3.3.2 X-ray Tomography Observations

Figure 7 shows a comparison of volume renderings of the surface of the specimen captured before and after potentiodynamic polarization from each of the 4 regions considered for this study. Additionally, figure 8 shows a comparison of the corresponding 2D virtual slices within the volume of the 3D microstructure before and after the Potentiodynamic polarization testing.

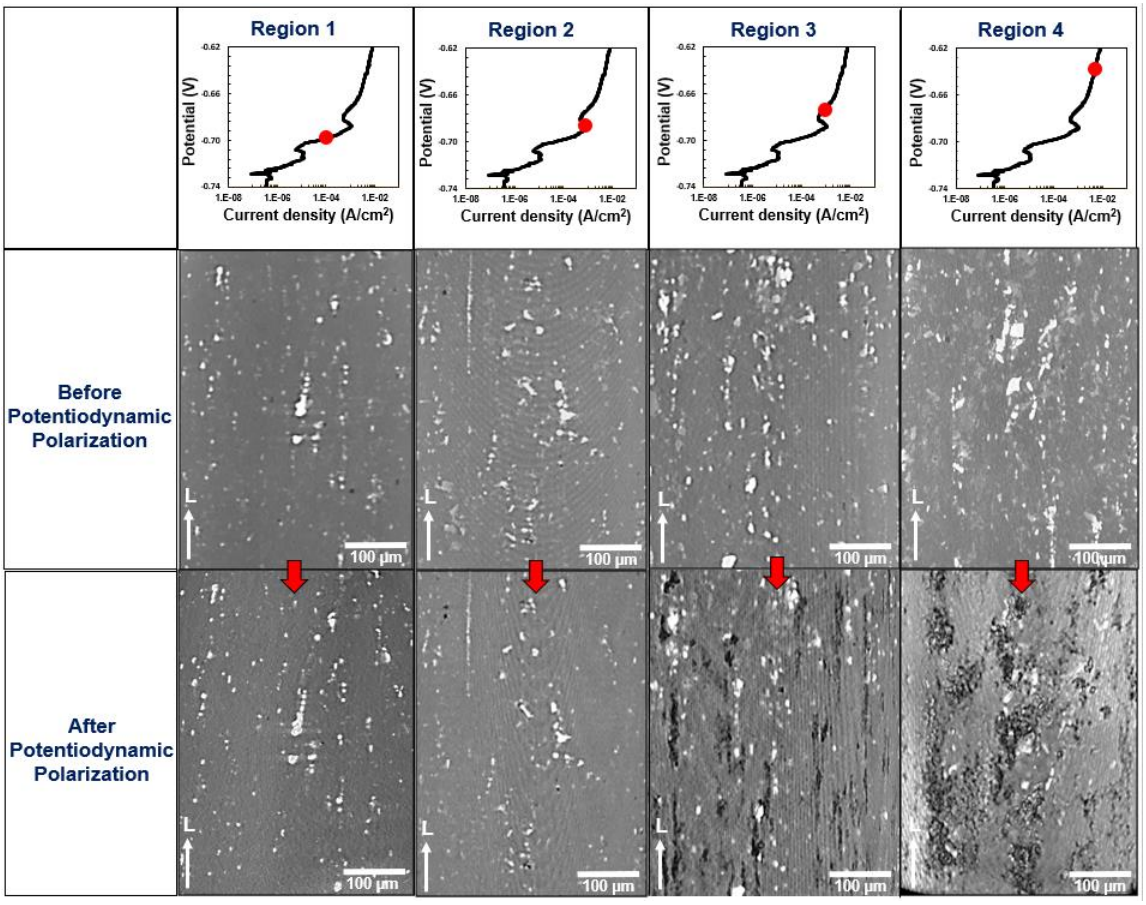

Figure 7: Representative images of the outer surfaces (from the x-ray tomography dataset volume renderings) of the specimens before and after potentiodynamic polarization testing. Macroscopic damage begins only after the second breakdown potential is surpassed.

In Region 1, where the potentiodynamic polarization curve is immediately beyond the first breakdown potential, there is no visible microstructural damage seen and the microstructure before and after the polarization look identical. The Fe-rich inclusions (seen as white particles distributed all over the grey matrix) are often observed to be the starting sites for macroscopic corrosion damage. However, trenching or pitting in the matrix or around inclusions is also not observed in the specimen.

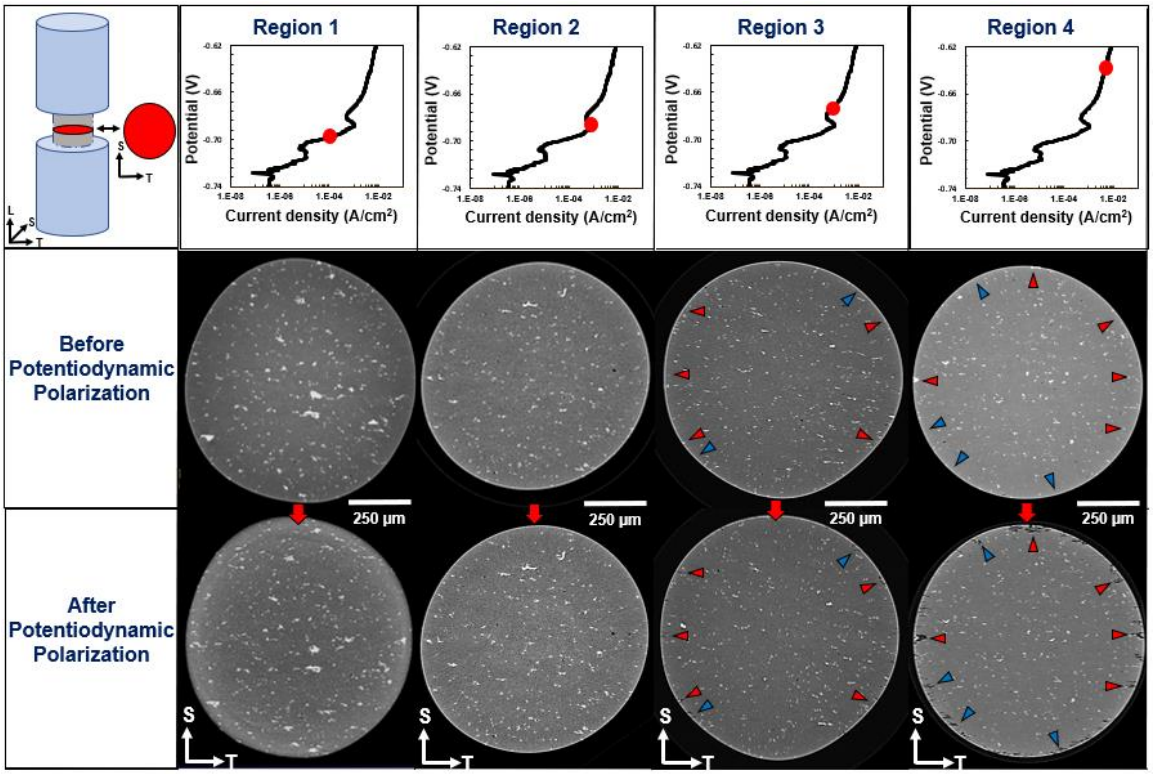

Figure 8: Virtual slice comparison showing the ST plane for each specimen before and after potentiodynamic polarization testing. Red arrows indicate sites where pits initiate clearly from Fe-rich inclusions. Blue arrows indicate sites where pits are not observed (or resolvable) to initiate at microstructural constituents.

Similarly, in region 2, where the potentiodynamic polarization curve is interrupted immediately before the second breakdown potential, there is still no observable microstructural damage in the form of pitting in the matrix or around inclusions. Contrastingly, region 3 which is immediately beyond the second breakdown potential shows a substantial amount of corrosion attack occurring all over the surface. Volume rendering of the pits on the surface from figure 4 show that the damage comprising of

corrosion pitting and fissures, appears to be aligned along the length or L direction (rolling axis of the plate).

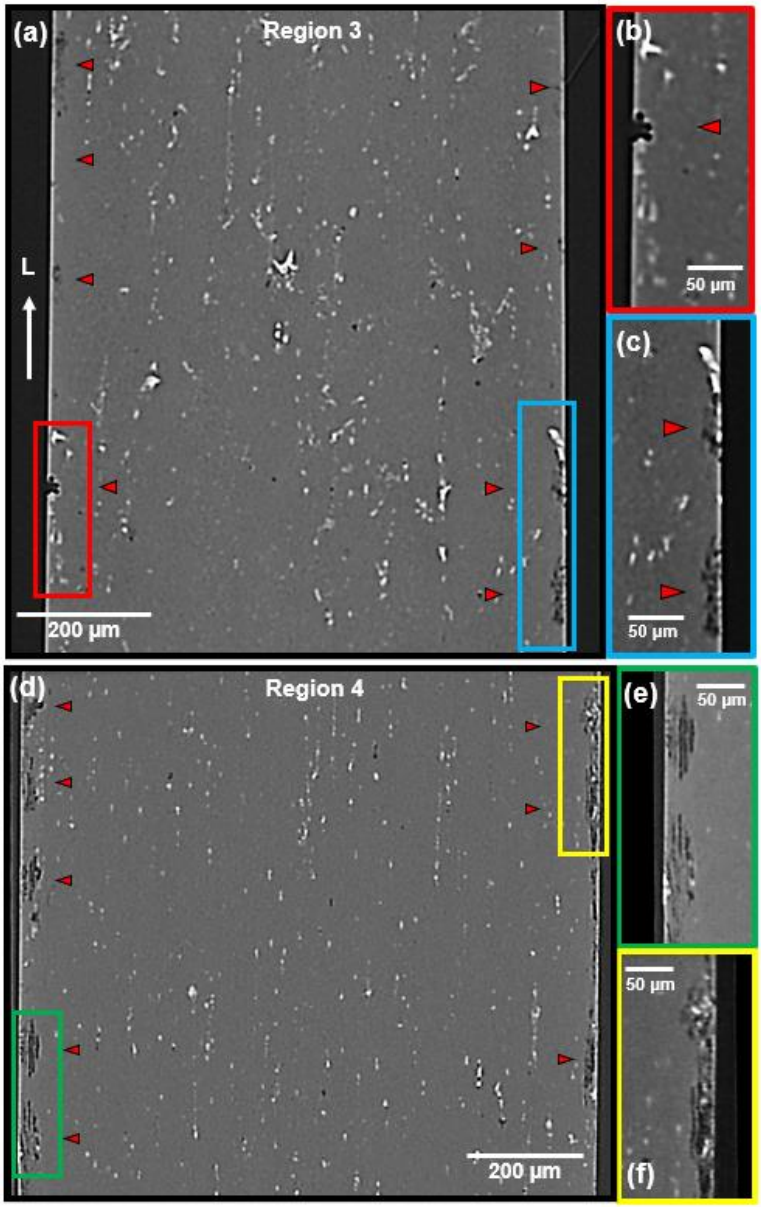

Figure 9: Virtual slices from regions 3 and 4 showing planes parallel to rolling axis (L) for each specimen before and after potentiodynamic polarization testing. Red arrows indicate pits in both conditions.

Moreover, the corrosion pit damage is not restricted to regions surrounding Fe-rich inclusion sites alone. Damage can also be seen in regions that are seemingly not associated with large Fe-rich inclusions or inclusion clusters. These pits may be forming at dispersoid locations or grain triple points. Re-slicing this data and visualizing the cross section parallel to the L-direction as in figure 9(a) shows maximum pit depth immediately beyond the second breakdown potential to be 30 μm.

Lastly, region 4 which is 30 mV beyond the second breakdown potential, shows the most amount of surface and sub-surface damage among the regions studied. Damage in this case is substantially exacerbated in terms of surface area of corrosion as well as max depth of the pitting, which can reach up to 80 μm. Interestingly, pit growth is a strong function of the orientation of the alloy. Pit dimensions are seen to be longest along the L-direction, followed by T- direction and finally the S-direction[124]. Figure 9(b) shows a virtual cross section of the specimen parallel to the L-direction with examples of pits. The corrosion pitting damage has a directional behavior with the longest pit dimensions being along the L direction of the specimen. The pits also demonstrate interesting layered morphologies which will be further discussed.

3.3.3 SEM Observations

Specific regions of the specimen such as inclusion clusters were registered before the potentiodynamic polarization experiment to study localized corrosion and changes in chemical composition. Figure 10 is a comparison of an earmarked area before and after the potentiodynamic polarization scan of a specimen that was interrupted at region 1. No corrosion damage is visible on the surface. Additionally, no trenching or compositional changes were observed in the Fe-rich intermetallics. However, EDS indicated that the Mg

rich particles i.e Mg_2Si and the S-phase (Al_2CuMg) dispersoids show a decrease in Mg concentration.

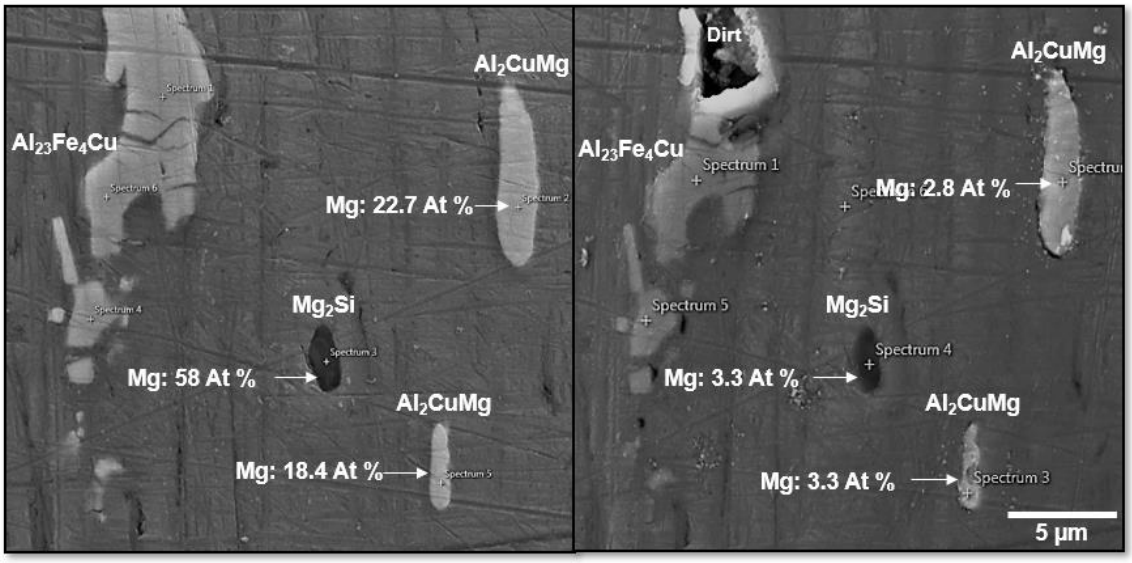

Figure 10: SEM + EDS images from specimen interrupted immediately beyond the first breakdown potential. Comparison of a set of earmarked inclusions shows a decrease in Mg content in Mg_2Si and Al_2CuMg (S-phase) particles as the first signs of observable damage at this length scale

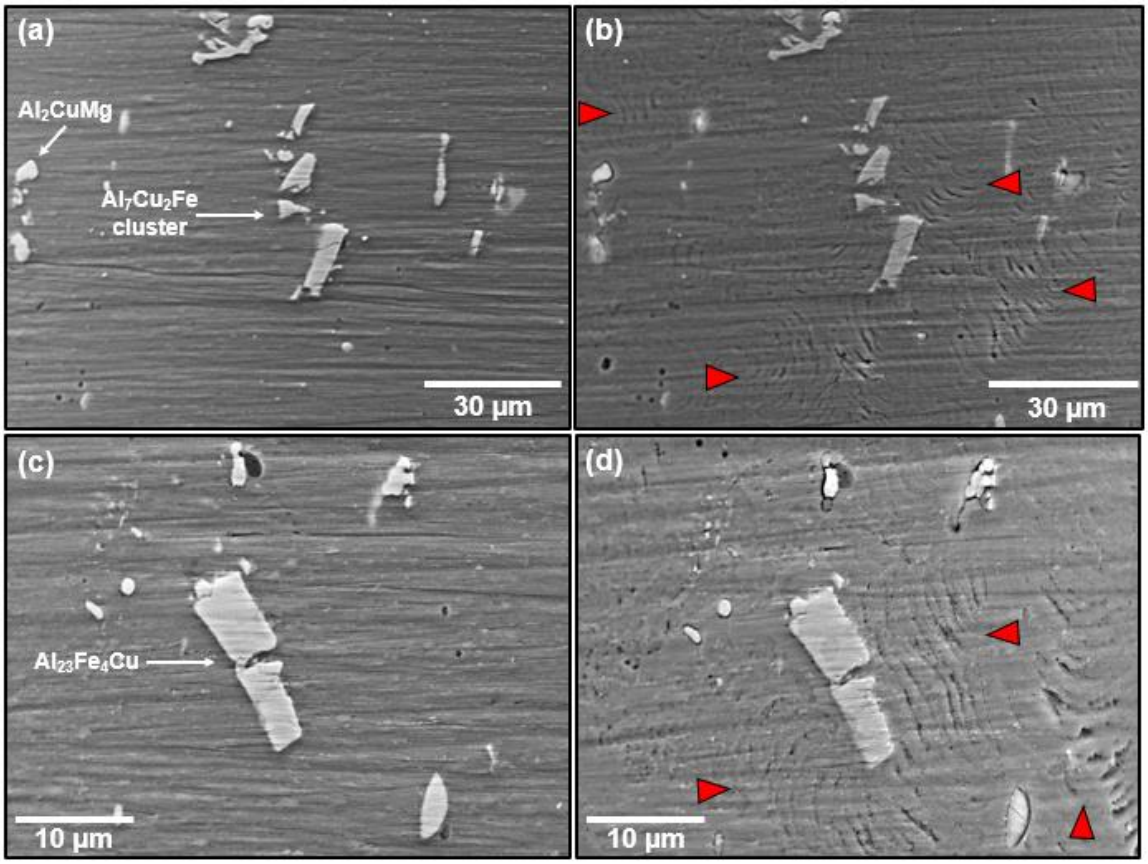

Figure 11: SEM and EDS images from specimen interrupted immediately before the second breakdown potential. Dealloying of S-phase particles and the very first signs surface corrosion are seen at this potential with the formation of concentric corrosion patterns around Fe-rich inclusions.

Figure 11 shows a comparison of multiple regions sampled in the specimen terminated at region 2. From the EDS data, a similar compositional change as in region 1 is observed. Figure 11(a) and (b) shows an example of an S-phase particle that has undergone Mg dissolution from 19 at. % to 0 at. %. A combination of reduction in Mg concentration and trenching around the particle is observed to occur. Fe-rich inclusion particles do not undergo any compositional changes at this potential. However, the area

surrounding these particles clusters undergoes surface damage in the form of concentric corrosion patterns that appear similar to lacy patterns (Figures 11(c) and (d)). This serves as evidence to show that the very first signs of surface damage are observed before the second breakdown potential of the specimen.

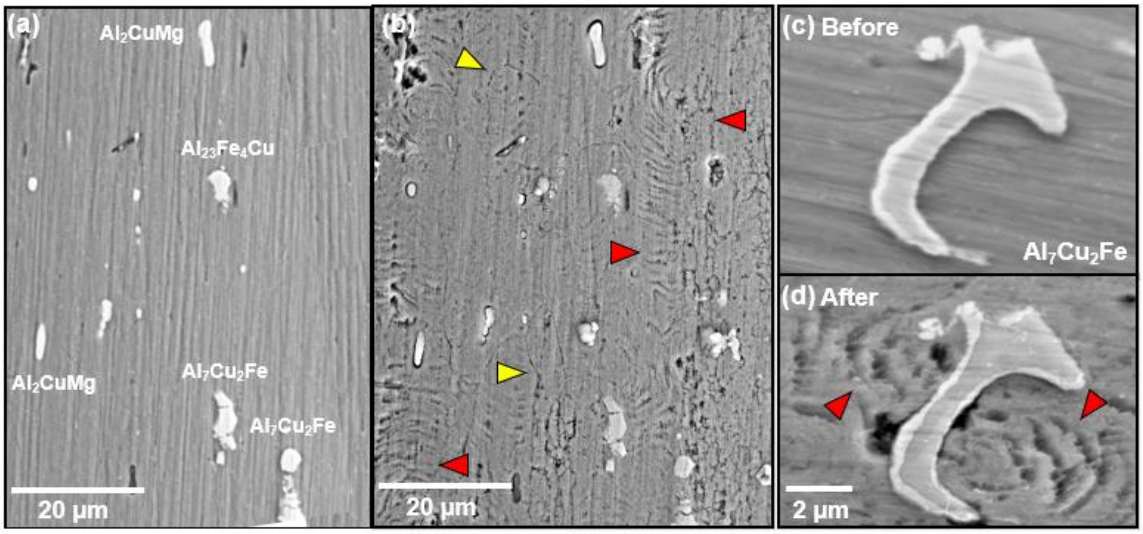

Figure 12: SEM images from specimen interrupted immediately after the second breakdown potential. (a) and (b) show an earmarked portion of the specimen with inclusion clusters of various compositions. A combination of intergranular corrosion (Yellow arrows), trenching at Fe-rich inclusions and Al_2CuMg particles and concentric corrosion patterns (Red arrows) is seen to be acting simultaneously. (c) High magnification image of an Al_7Cu_2Fe particle that has undergone peripheral trenching and is also accompanied by concentric corrosion patterns.

Region 3 showed uniform macroscopic corrosion damage as per the X-ray microtomography data with pitting observed in regions with and without being associated with inclusions. These tomographic observations are corroborated by observations with the SEM which show a combination of mechanisms acting simultaneously to corrode the

specimen. Figure 12 shows examples of each of these phenomena. Figures 12(a) and (b) show an earmarked region before and after the polarization scan. A combination of intergranular corrosion (yellow arrows), S-phase dissolution and periphery trenching and concentric corrosion patterns (red arrows) is seen.

Trenching around Fe-rich inclusions is observed to start at this region in the curve. Figure 12(c) and (d) shows an example of an Fe-rich inclusion that has undergone trenching and is also surrounded by the concentric corrosion patterns that was first observed in region 2. Trenching is a well-studied phenomenon acting in association with Fe-rich inclusions[100]. In a neutral saltwater environment, Fe-rich inclusions are cathodic with respect to the aluminum matrix surrounding it. This can lead to the formation of a local galvanic cell thereby causing preferential dissolution of the aluminum matrix surrounding the inclusion. Additionally, dealloying and trenching of S-phase dispersoids is also observed.

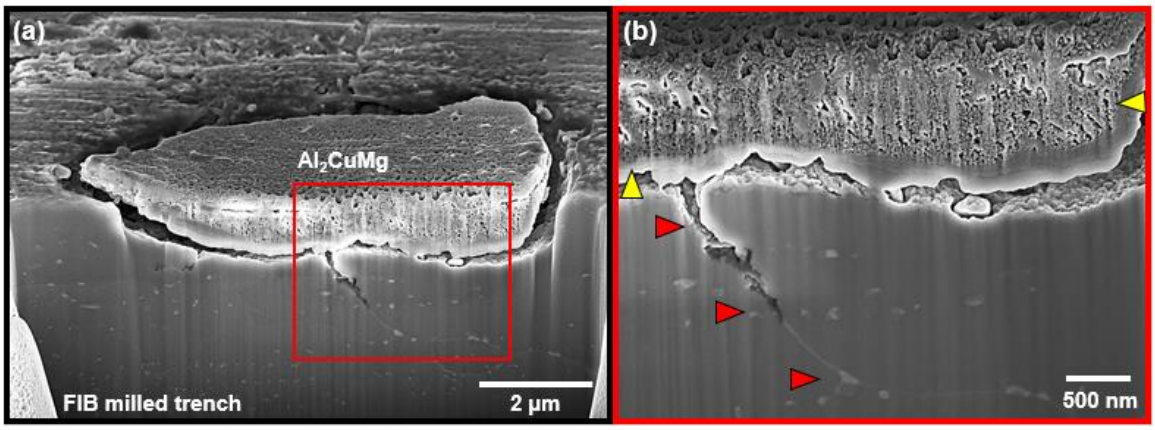

Figure 13: FIB cross section of an S-phase dispersoid particle. Trenching, dealloying and intergranular corrosion has been observed beneath the particle assisted by the presence of grain boundary precipitates.

Figure 13(a) shows an Al_2CuMg dispersoid cross sectioned using a FIB Ga+ beam. Three phenomena are seen to act simultaneously to enhance localized corrosion. The decrease in Mg concentration as per EDS measurements combined with the cross section of the particle shows that it has undergone selective anodic dissolution of Mg to leave behind a Cu-rich structure[21,83,127]. With increased dealloying, the particle can behave cathodic to the matrix and lead to trenching around its periphery. Additionally, further damage in terms of intergranular corrosion assisted by the presence of grain boundary precipitates is seen to initiate underneath the particle (figure 13(b)).

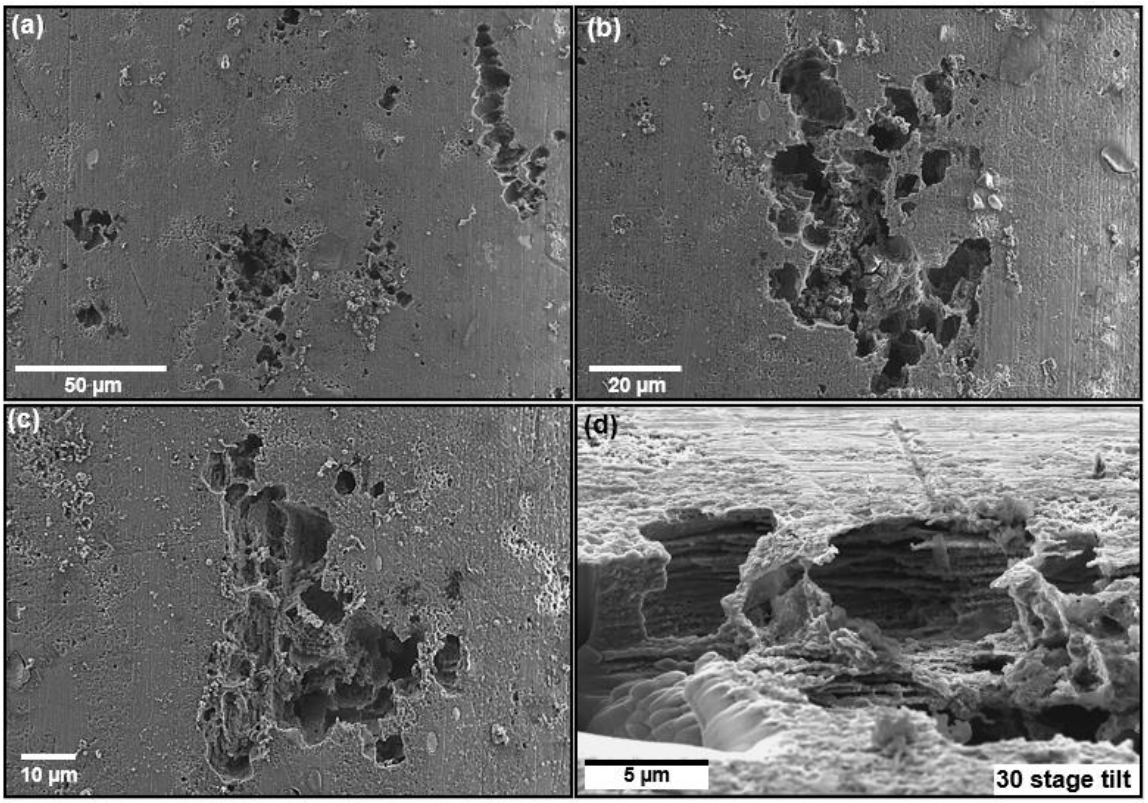

Figure 14: Region 4: SEM images from specimen interrupted roughly 30 mV beyond the second breakdown potential. Apart from the corrosion mechanisms acting in region 3, extensive pitting with layering is also observed at this potential.

Region 4 shows the maximum amount of corrosion damage as compared to the other 3 regions. Corrosion features like those seen in region 3 i.e Trenching around Fe-rich inclusions, S-phase dissolution and intergranular corrosion were substantially exacerbated at this potential. As in figure 14(b), pitting corrosion was also observed all over the specimen with maximum pit depths reaching values of ~80 μm. Additionally, some of these pits seem to be formed through the coalescence of smaller pits (Figure 13(b) and (c)). The layered morphology of pits as observed in the tomography results for this specimen can be seen in figure 13(d). With worsening pitting and such layering, rampant sub-surface grain dissolution is also observed in the specimen and is elaborated on later.

At this point, it is clear that as the potential is increased during the Potentiodynamic polarization test, several corrosion processes act simultaneously to contribute toward surface and sub-surface damage. Here, we discuss three such microstructural damage mechanisms- pitting corrosion, concentric corrosion patterns and Fe-rich inclusions:

3.3.4 Pitting Corrosion and Exfoliation Behavior

At region 4 of the Potentiodynamic polarization curve, the region of interest of the AA 7075-T651 rod is characterized by the presence of extensive surface damage and deep corrosion pitting. These pits are characterized by the presence of “banded” or “lamellar” structures within them[117,125].

Figure 15(a) shows an example of two virtual views (cross section view or ST plane and another plane parallel to the L-direction) of a single pit in the specimen. The pit initiated at an Fe-rich inclusion site and was surrounded by other pits in the near vicinity as shown in the volume rendering in figure 15(b). The pits and sub-surface corrosion damage were

carefully segmented to visualize the layered structural damage and are colored red in figure 15(b).

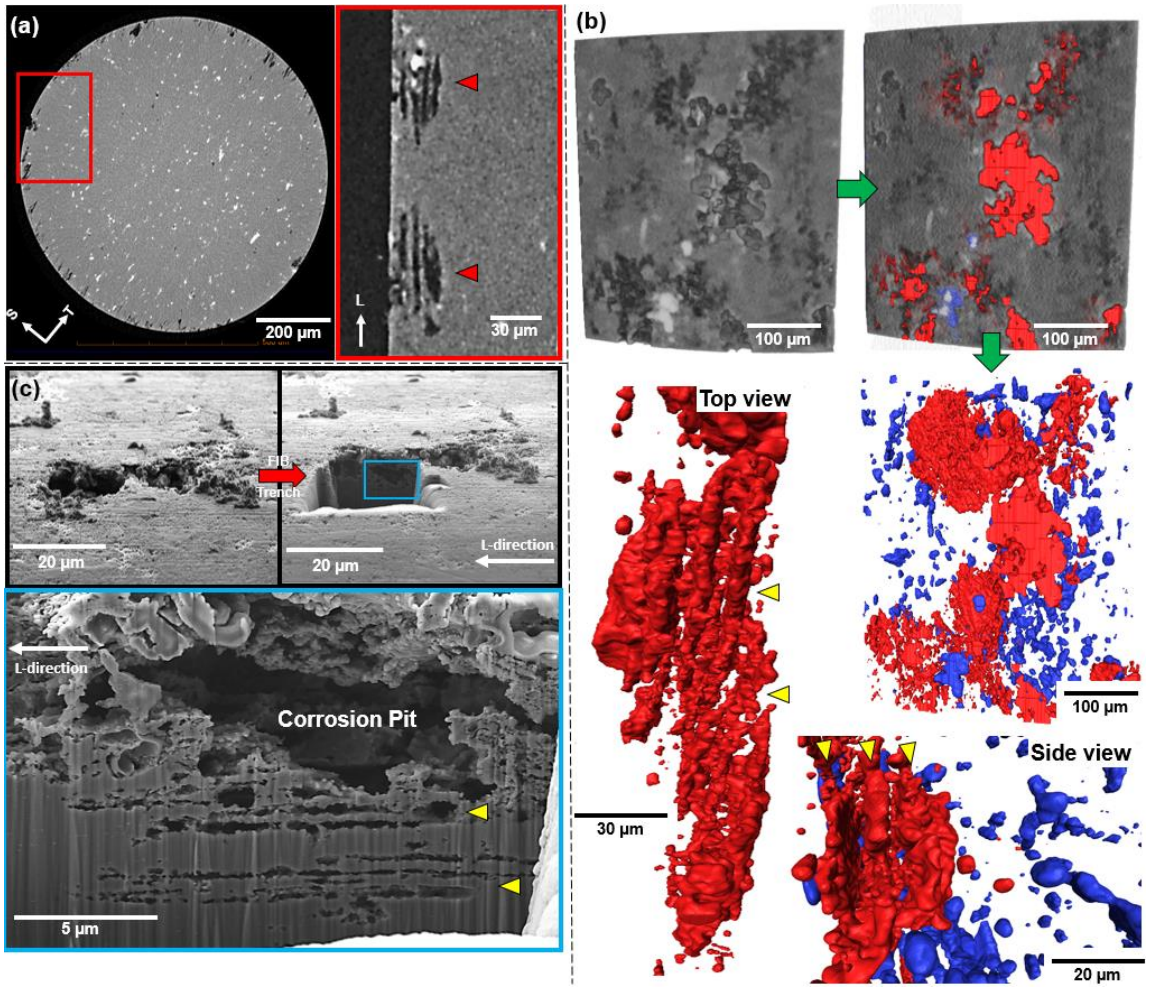

Figure 15: Exfoliation corrosion, (a) Observation of exfoliation like action in x-ray tomography datasets hinted at lamellar structure formation underneath corroding pit surface. (b) Sequence of images showing the segmentation and rendering of pit and sub-surface exfoliation. (c) Example of a corrosion pit where a FIB trench was milled using Ga+ ions showing sub-surface transgranular exfoliation like action.

Top and side view of sub-surface corrosion damage clearly show the presence of the banded structure and help understand the 3D morphology of the exfoliation attack. Amidst the pit and layers are remnants of Fe-rich inclusion particles through which the exfoliation attack passed through. FIB-SEM was used to mill trenches into multiple pits to study sub-surface damage. An example of this is shown in figure 15(c) where a ~20 µm wide trench was milled at a pit site. Layers in this specimen involved attack along a direction parallel to the rolling direction, akin to Exfoliation Like Action (ELA) as observed by Eckermann et. al. Sub-surface damage in the form of transgranular ELA (shown with yellow arrows) can be seen underneath the pit on this cross section. In both the tomography scans and SEM images, no blistering and grain etching/lift-out was observed. The spacing between layers of the ELA damage can be equivalent to or lesser than the resolution of x-ray tomography scans making it highly likely that they will not be resolved individually and hence appear merged into thicker layers within the pit.

Exfoliation attack has been observed and documented in aluminum alloys. Robinson and Jackson observed that exfoliation attack is a form of intergranular corrosion[128]. According to them, grain aspect ratio played an important role in determining the severity of exfoliation attack, indicating that grain boundaries corresponding to elongated grains (as can be seen in the AA7075-T651 material used in this study) were highly susceptible. Zhao et. al used 2D x-ray radiography to observe exfoliation attack in AA2024 and AA7178 and concluded that grain boundary composition was critical to determining susceptibility to attack[129,130]. Additionally, Eckermann et. al studied exfoliation attack in AA 6XXX alloys and argued that while solution aggressivity is critical to the extent of exfoliation attack, it was independent of grain boundary elongation, intermetallic particle alignment

and texture. Microstructurally, most of these studies point to a strong correlation between grain boundaries and exfoliation attack. The specimen which was interrupted at region 3 of the Potentiodynamic polarization curve showed trenching, surface pitting at Fe-rich inclusion and Al_2CuMg sites and intergranular corrosion (figure 16(a)). But no ELA damage was observed in the vicinity of the inclusions/intergranular corrosion, like in the specimen from region 4 (figure 16(b)). This indicates that pit formation and intergranular corrosion are pre-requisites to sub-surface exfoliation attack in the specimen[108,131]. Additionally, the exfoliation attack was parallel to the L direction of the plate as in figure 15(a), (c) and (d). The amount of sub-surface damage in the form of ELA and grain dissolution is abundantly clear. However, the precise local mechanism by which intergranular corrosion is linked to ELA and what conduces ELA corrosion is still unclear.

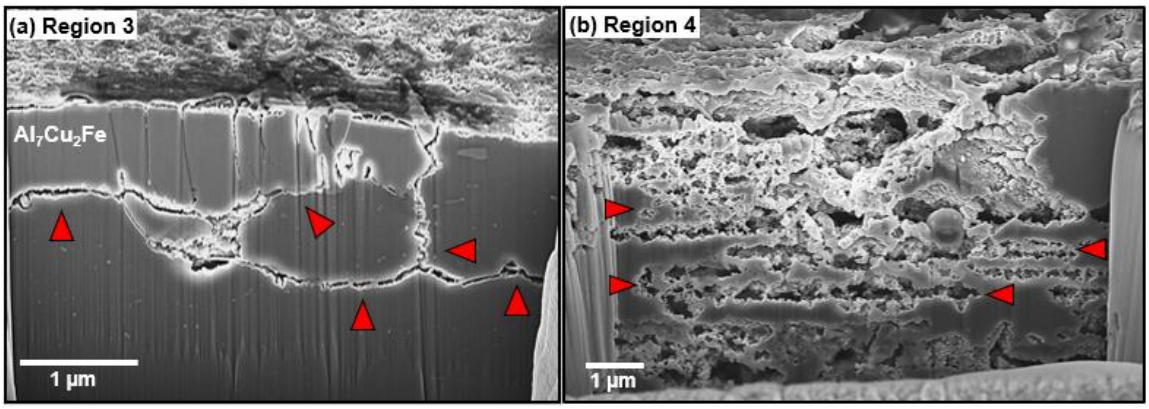

Figure 16: Comparison of sub-surface damage from specimens interrupted at (a) region 3 showing intergranular corrosion around the Al_7Cu_2Fe particle, and (b) region 4 showing extensive ELA and grain dissolution.

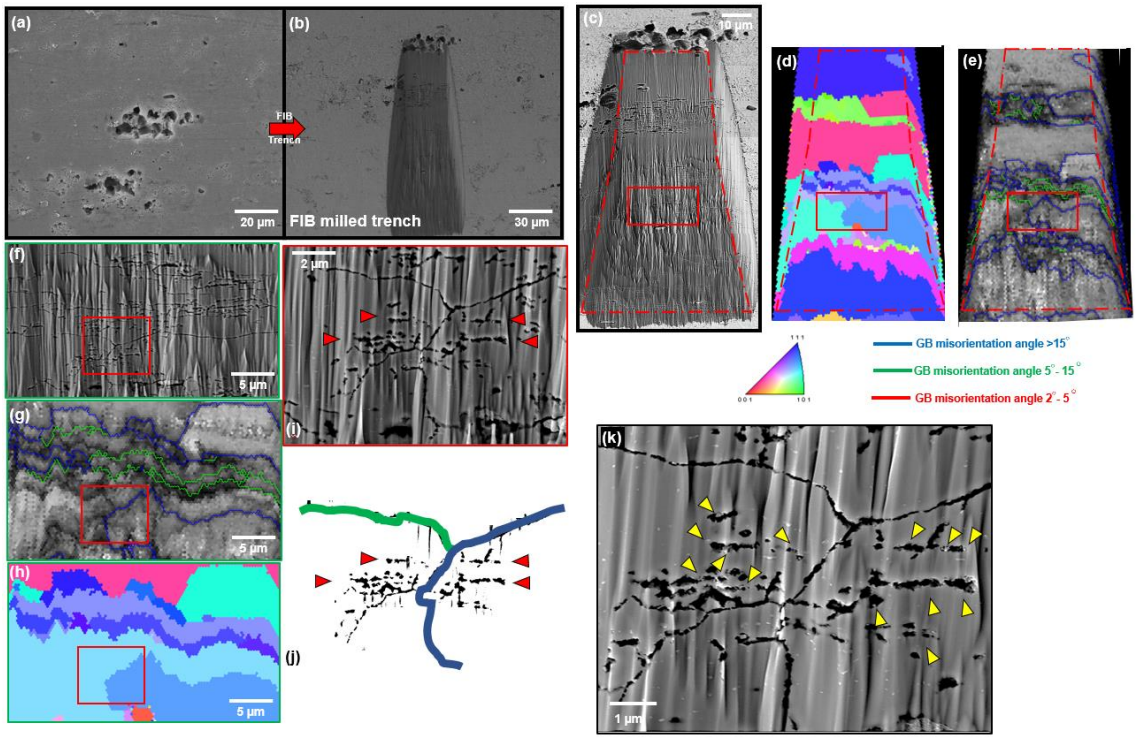

Figure 17: (a) Pit of interest that was chosen for Ga+ milling by grazing incidence, (b) Milled surface exposing multiple exfoliation sites and grain boundary attack, (c),(d) and (e) show the ROI, corresponding EBSD IPF map and the corresponding grain boundary misorientation map, (f), (g), (h) and (i) highlight a specific region within the area showing representative ELA initiation behavior,(j) Segmented image of (i) highlighting the low and high angle grain boundaries accompanied by ELA (red arrows), (k) Yellow arrows pointing to precipitate remnants within the ELA hinting at the ELA's propagation mechanism.

Figure 17 shows a FIB milled cross section of a large portion of the matrix sub-surface intergranular corrosion and exfoliation corrosion acting simultaneously. Figure 17(a) and (b) show a pit cluster that was sectioned using Ga+ ions at grazing incidence (milled at 0° stage tilt as opposed to the standard 54° stage tilt), thereby enabling the observation of a large sub-surface area. To observe the correlation between exfoliation

damage and grain character, EBSD of the milled surface was performed. Figure 17 (d) and (e) shows the IPF pattern and grain boundary misorientations of the grains on the FIB milled surface. Figures 17(f), (g), (h) and (i) highlight a region within this large surface area where the mechanism of initiation of exfoliation like action is clear. Highlighted are the high angle and low angle grain boundaries.

Comparing sub-surface attack in region 3 and 4, a hypothesis for the initiation and propagation of ELA can be made. First, the high angle grain boundaries are observed to undergo intergranular corrosion immediately beyond the second breakdown potential. With increasing potential, low angle grain boundaries are also observed to be attacked. This is evidenced by the fact that all FIB cut regions sub-surface were observed to contain high and low angle grain boundary attack (figure 17(e) and (g)). Figure 14(j) shows a segmented view of the figure 17(i) highlighting the nature of the boundaries involved and red arrows points to exfoliation attack within grains. Contained within such attack are remnants of precipitates(yellow arrows) providing a clear path for the transgranular propagation of the attack, thereby indicating that ELA attack begins at grain boundaries and in some cases at triple points and furthermore, propagates within grains with the assistance of precipitates (figure 17(k)). Continued ELA leads to grain dissolution. While it is not clear if the exfoliation corrosion damage leads to grain removal in these specimens, it is expected that under an increased applied potential, due to the large volume of corrosion product and gaseous hydrogen generated sub-surface, substantial wedging stresses could be generated and lead to grain removal [63,132,133].

The observation of exfoliation in the x-ray tomography data was vital as it pointed out the peculiar nature of the sub-surface corrosion attack. Without the x-ray tomography

data, it would have been easy to miss out on the sub-surface behavior of the pits at this applied potential. This goes to show the advantage of using such a correlative microscopy-based approach to studying the evolution of microstructures in corrosion studies.

3.3.5 Concentric Corrosion Patterns

Concentric corrosion patterns were observed in regions 2 and 3 of the scan. While they were also observed in region 4 in trace amounts, the extent of general surface corrosion and localized pitting around constituent particles was large enough to obscure the observation of these patterns.

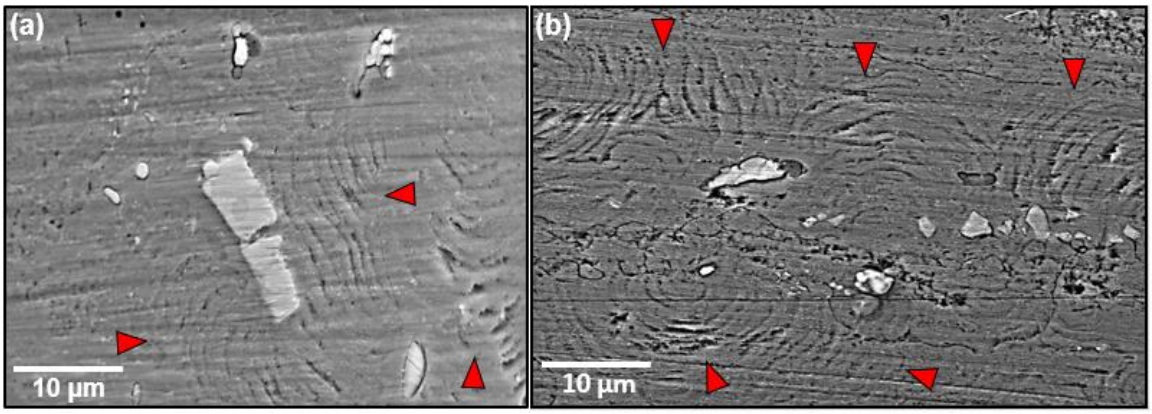

Figure 18: Concentric corrosion patterns are observed in region 2(around Fe-rich inclusions) and region 3 (almost all over the surface).

The concentric corrosion patterns were restricted to regions around inclusion clusters in region 2 and were observed uniformly all over the surface of the region of interest in region 3. The patterns appear very similar to lacy cover formation that are observed during pitting of certain steels [134–136]. However, lacy patterns contain active pits underneath the surface of the cover while FIB sectioning has shown that these

concentric corrosion patterns do not contain a pit underneath the surface and that they are purely a surface phenomenon.

The first breakdown potential is associated with the dissolution of a surface layer that is formed due to polishing. Polishing has been hypothesized to cause severe plastic deformation on the surface thereby leading to breaking down and redistribution of precipitates to the grain boundaries. This redistribution has been observed using Molecular Dynamic (MD) simulations, to occur in the form of a rotational flow manifesting in eddies or vortices in regions where strain is high[52,137]. Coincidentally, the patterns observed in the specimen of this study resemble vortices or eddies. Although it is not clear what the extent/range of such rotational flow assisted redistribution on the surface is, this microstructural anomaly only partially explains the presence of the concentric corrosion patterns. It is still not clear why only the regions around the inclusion clusters get attacked first.

Pattern formation during corrosion attack has also been observed in AA2024 wherein rings of corrosion product were formed around areas containing inclusion clusters[138,139]. Areas within these rings showed increased sub-surface intergranular corrosion. The authors hypothesized that hydrogen evolution within corroded grain boundaries forces anolyte solution (solution rich in Al^{3+} ions) into the bulk solution. Subsequent neutralization in the bulk solution makes the newly formed corrosion product to form the ring. With regard to the AA7075-T651 used in this study, hydrogen evolution is a critical observation that takes place at cathodic particles on the surface of the alloy such as at Fe-rich inclusion sites. However, the specimen in this study shows selective erosion of the matrix as opposed to deposition. One possible hypothesis involves the occurrence of

local magnetohydrodynamic phenomena on the surface[140]. Electrochemical reactions in the presence of an external magnetic field have been reported to lead to the formation of a Lorentz force that can induce electrolyte convection and aid corrosion[141–145]. Here, the specimen is essentially a current carrying conductor which can induce a weak magnetic field parallel to its surface around itself (Maxwell's right-hand thumb rule). Local electrochemical cells with small magnitudes of current are present on the surface at Fe-rich inclusions due to the presence of galvanic coupling with the matrix. The induced magnetic field combined with the surface current values could potentially lead to the formation of a weak Lorentz force that is orthogonal to the surface around these inclusions. This Lorentz force acting on the ionic solution immediately above the inclusion particle could induce repeated convection in the fluid and thus, attack the region immediately around the particle preferentially. This phenomenon, in conjunction with the polishing induced particle breakdown and redistribution could lead to the formation of such a pattern.

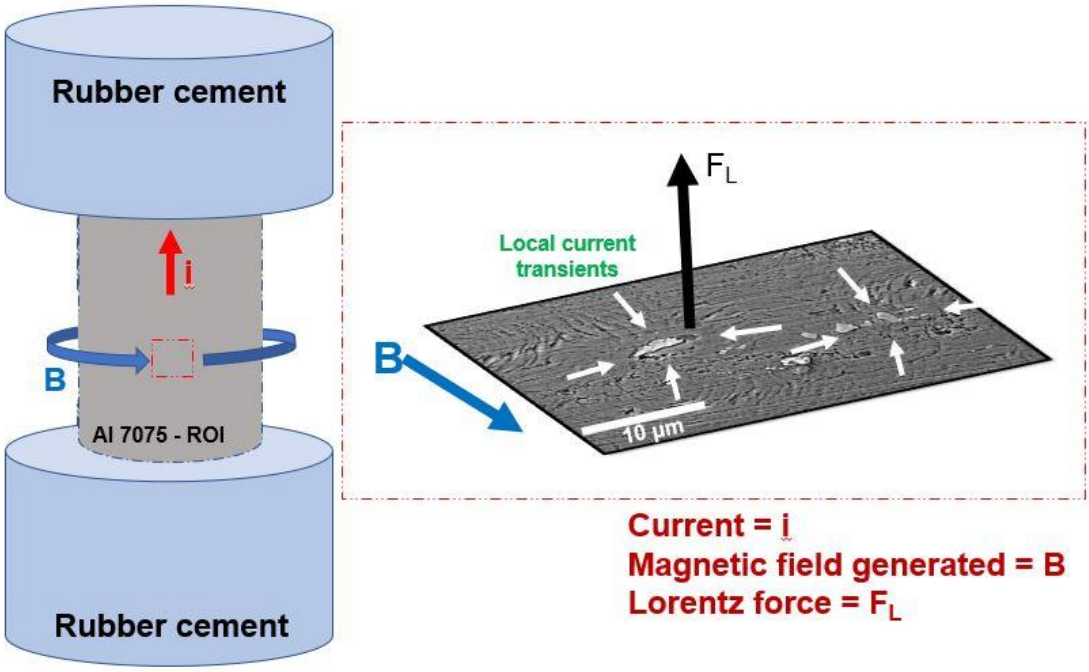

Figure 19: Hypothesized mechanism for the formation of concentric corrosion patterns. A combination of induced magnetic field and local surface current transients could potentially induce a Lorentz force acting orthogonally to the surface which can induce a convective action in the fluid.

3.3.6 Fe-rich Inclusion Dissolution Behavior

The role of Fe-rich inclusions (Al_7Cu_2Fe and $Al_{23}Fe_4Cu$) has been investigated in many research works till date. It has been shown unequivocally that in neutral 3.5 wt.% NaCl solution, they are cathodic to the aluminum matrix. A local electrochemical cell/ galvanic couple is created between inclusion and the surrounding matrix leading to the selective dissolution of the matrix adjacent to the particle, thereby leading to trenching. Fe-rich inclusions contain cracks that are created during the rolling process as they are harder than the nearby matrix. During this study, FIB assisted destructive serial sectioning nano-

tomography was used to section through an Al_7Cu_2Fe inclusion particle to observe the sub-surface corrosion attack.

Figure 20(a), (b) and (c) shows a schematic of the serial sectioning nano tomography procedure that was employed at the inclusion of interest. First, the Al_7Cu_2Fe inclusion particle was identified and a trench was milled adjacent to it using Ga^+ ion beam (figure 20(a)). Next, a layer of Pt was deposited on it to ease FIB milling and minimize surface roughness induced curtaining (figure 20(b)). The nano-tomography procedure involved alternating between the Ga^+ beam and the e^- beam to mill and image the region of interest (figure 20(c)). A slice thickness of 50nm was used to mill through a volume of 14 µm (width) x 10 µm (height)x 4.2 µm (depth). The serial sectioning procedure yielded a stack of images as a function of mill depth. Figure 20(d) shows an example of images obtained from different depths within the region of interest.

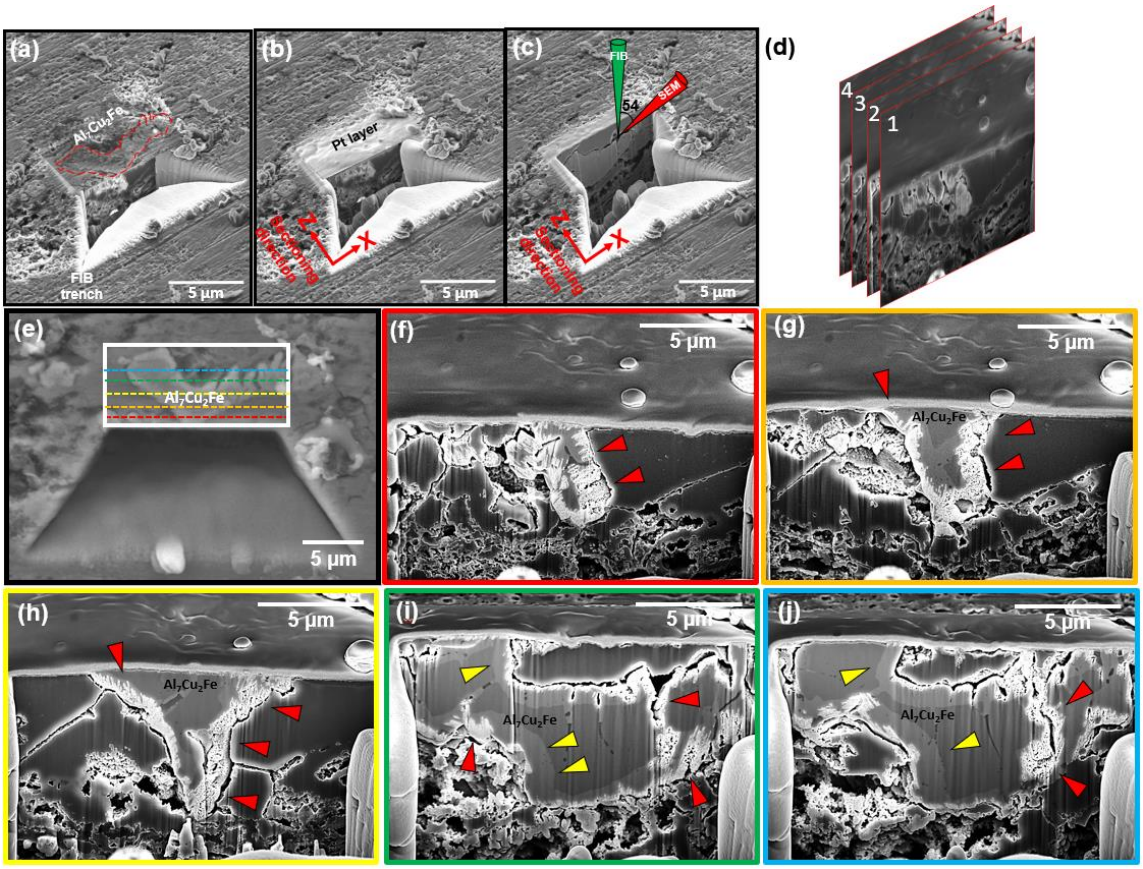

Figure 20: (a) (b) (c) (d) show the serial sectioning nano-tomography procedure employed to obtain a 3D array of closely spaced images that can be used to analyze small volumes. (e) Top view of the ROI as in (a) with color coded lines pointing to the position of specific slices, (f)(g)(h)(i)(j) show five representative slices that show sub-surface corrosion mechanisms existing at this potential. Extensive trenching, exfoliation like action and grain dissolution are seen. Additionally, red arrows point to locations where the Fe-rich inclusion particle (Al_7Cu_2Fe) is seen to be dissolving under the imposed potential.

Figure 20(e) shows a top view of the Al_7Cu_2Fe inclusion wherein the white box indicates the region that was sampled for the nano-tomography. The lines in different colors show the locations where representative images of the milling process are shown

from figure 20(f) to (j). Several corrosion damage features are prominent over the course of the analysis of the serial sectioning nano-tomography. Trenching along the periphery of the Fe-rich inclusion, sub-surface intergranular corrosion and grain dissolution are rampant. Interestingly, there exists within the particle a transition region with a lighter grey value (yellow arrows) as compared to the interior of the inclusion, which shows the relatively darker grey value. Additionally, the edges of the inclusion particle as well as the regions of the particle adjacent to the cracks in the inclusion show dissolution of the inclusion particle (red arrows). This indicated that the imposed potential is high enough to start observing the dissolution of the inclusion particle.

Figure 21(a) shows another example of a subs-surface Al_7Cu_2Fe inclusion particle that had undergone dissolution. Figure 21(b) shows a high magnification image of the right edge of the dissolving particle. Contained within the remnant particle are clusters of particles held by corrosion remnant regions (light grey) amidst porosities that are indicative of dissolved regions (dark grey). It is important to note that Al_7Cu_2Fe particle dissolution was not observed in an AA7075-T651 specimen immersed in the same corrosive medium under open circuit conditions[100]. However, selective dissolution of Al_7Cu_2Fe has been observed by Lebouil et. al. under a 2M H_2SO_4 acidic environment plus an imposed potential and Atomic emission spectroelectrochemistry (AESEC) was used to study the dissolution of Al_7Cu_2Fe [146]. It was observed that the Fe/Al ratio during the dissolution process remained constant at 1:7, indicating that both Fe and Al dissolve simultaneously during the polarization experiment. This would indicate that the dissolution observed at the edges of the inclusion particle would leave behind Cu particles. Thus, the corrosion mechanism acting here is anodic dissolution of the particle, which is similar to the dissolution of

Al_2CuMg dispersoid particle. In other words, while the required potential for Al_7Cu_2Fe dissolution is more noble than that of Al_2CuMg, the dealloying mechanism is observed to be the same. Figure 21(c) shows a schematic of the remnant portion of the particle after anodic dissolution. Cu clusters are held together by either corrosion product or undissolved regions of the particle. Also shown are the porosities formed due to dissolution.

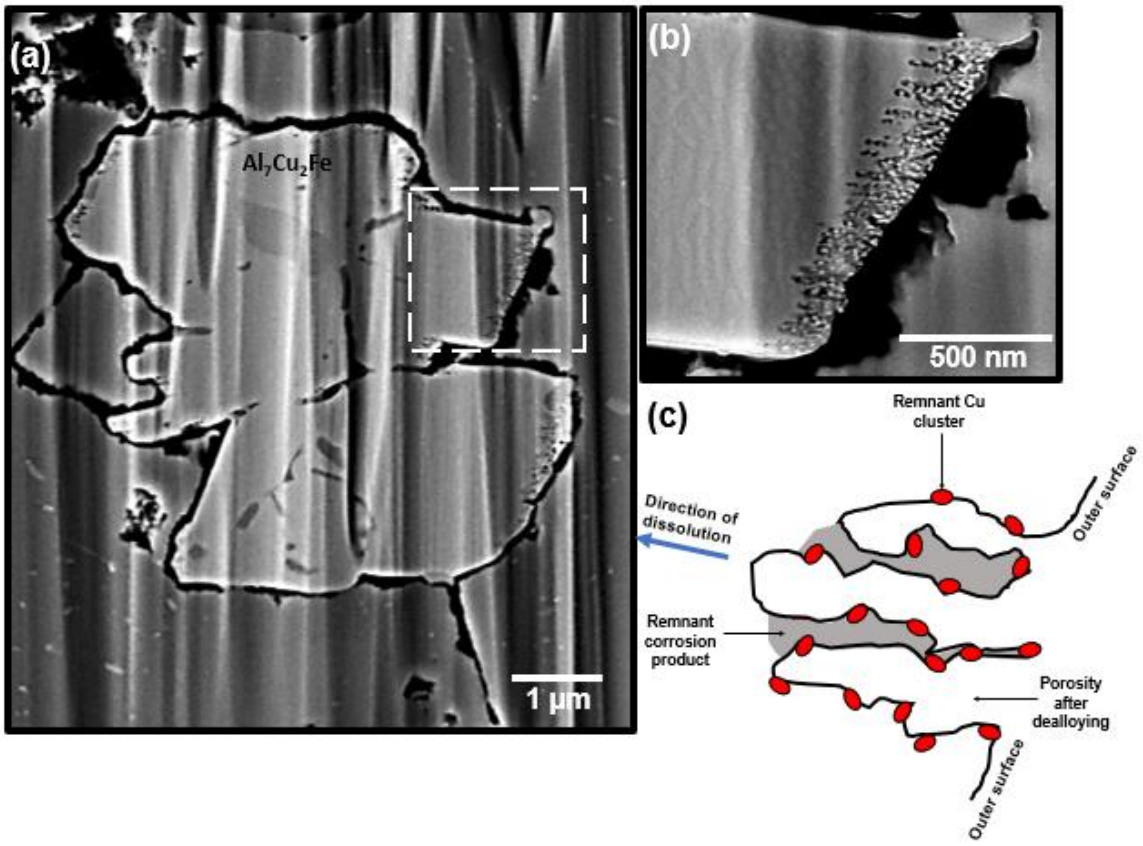

Figure 21: Mechanism of dissolution of Al_7Cu_2Fe, (a) Example of a sub-surface Al_7Cu_2Fe particle that was sectioned using FIB milling. Curtaining effects visible on the cut surface due to uneven open surface above. (b) High magnification image of one edge of the particle that shows directional dissolution. (c) Schematic of remnant Al_7Cu_2Fe particles dissolution to leave behind Cu clusters and pores.

Interestingly, the Al_7Cu_2Fe particle also has a directional preference for dissolution. Figure 18(b) shows this directional preference. Directional dissolution has been observed in Al_2CuMg particles as well and it was hypothesized that this dissolution was along certain crystallographic directions[127].

3.4 Summary

The aim of this study was to study microstructural evolution during the course of the potentiodynamic polarization scan in AA 7075-T651. Four regions in the curve were identified and interrupted tests conducted at each of these sites. A combined correlative microscopy-based approach comprising of non-destructive 3D x-ray tomography and 2D electron microscopy proved to be very beneficial in visualizing corrosion damage over 3 orders of magnitude.

- X-ray microtomography results yielded information pertaining damage on the millimeter to the micrometer length scales. Volume rendering, image segmentation and analysis indicated that microstructural damage is seen to initiate and exacerbate right after the second breakdown potential is achieved. Corrosion damage in the form of trenching, corrosion pitting, intergranular corrosion and exfoliation like attack are observed.
- 2D electron microscopy results yielded information pertaining damage on the micrometer to the nanometer length scales. Selective dissolution of Mg from Mg rich metallic inclusions was observed using EDS starting from region 1. With increase in potential, attack of the matrix is seen to initiate via concentric corrosion patterns. Once the second breakdown potential is reached, features similar to those observed in the tomography data were noted.

- FIB was used extensively to study sub-surface damage. Anodic dissolution of Al_7Cu_2Fe particles was observed to leave behind Cu clusters, similar to the dissolution of Al_2CuMg.
- Exfoliation was observed using the tomography data and was further investigated using FIB-SEM and EBSD. While grain lift out or removal was not seen in this study, extensive transgranular exfoliation like attack was observed. With increase in potential, pitting is seen to initiate at inclusion particles or clusters and propagate into the material via intergranular corrosion (via high and low angle grain boundaries). Exfoliation like attack is then initiated when precipitates closest to the grain boundaries begin to undergo dissolution and propagate ELA to their nearest neighbors.
- Lastly, concentric corrosion patterns were observed to initiate in the vicinity of inclusion clusters before the second breakdown potential and all over the surface with increase in potential. A polishing induced strained microstructure in combination with convection of corrosive fluid (initiated by a local micro hydrodynamic effect) is hypothesized to play a role in the formation of such patterns in the vicinity of clusters at first and then continue to occur all over the specimen.

CHAPTER 4

NANOSCALE 4D MICROSTRUCTURAL CHARACTERIZATION OF CORROSION IN ALUMINUM ALLOYS USING TRANSMISSION X-RAY MICROSCOPY (TXM)

4.1 Introduction

Constituent particles play a critical role in determining the corrosion behavior of AA 7075 in all ageing conditions. Fe-rich inclusions are cathodic to the matrix. Due to this, they cause the local dissolution of the anodic matrix in their vicinity and enable trenching[27,29]. With increased corrosion time, these particles can be dislodged from the matrix, although they do not undergo dissolution at open circuit potential in saltwater solution[29]. Si rich inclusions are anodic to the matrix. Mg is observed to selectively dissolve from the matrix leaving behind a Si rich remnant that remains inert and does not contribute to further pitting under AA 7075's open circuit conditions[105,147]. Al_2CuMg dispersoids are anodic to the matrix at first and become cathodic after the selective dissolution of Al and Mg, leaving behind a spongy Cu remnant[21,83,148]. Lastly, the precipitates are anodic to the matrix. They are composed of $Mg(Cu_xZn_{1-x})_2$ with specific compositions changing from peak aged to overaged condition[104]. Precipitates are critical as their dissolution behavior determines the alloy's susceptibility to intergranular corrosion and Stress Corrosion Cracking. In saltwater, the intergranular corrosion of precipitates leads to the formation of hydrogen under anodic dissolution and further, the hydrogen can enable stress corrosion brittle cracking in the presence of a monotonic external load[104]. F. Andreatta et. al documented that the open circuit potential and the breakdown potentials

for as-quenched, peak aged and highly overaged AA 7075 and concluded that with ageing, these potential values increase because of the fact that the matrix had a higher content of Mg and Zn in the matrix in the super saturated as quenched specimen vs peak aged and overaged specimen[56,108]. This was hypothesized due to the larger availability of Zn and Mg in the solid solution aiding general corrosion of the alloy. Goswami et.al studied the composition of precipitates with ageing and observed an increase in Cu content in the precipitates from 15.1 at. % in peak aged condition to 20 at. % in the overaged condition. Additionally, a thicker PFZ was observed with increase in ageing time [51,104]. This indicates that with further ageing, localized corrosion could be much more exacerbated in the overaged specimen due to larger precipitates behaving more cathodically with respect to the matrix, a wider precipitate free zone and weakened/absent native oxide layer at the location of the particles.

Until now, almost all studies pertaining the composition and behavior of precipitates has been performed using TEM[104,149]. TEM provides excellent spatial resolution combined with the ability to perform chemical analysis. However, it is a 2D technique and it is destructive. Additionally, corrosion tests performed on TEM foils do not provide a statistically relevant understanding of the corrosion mechanisms at play. Atom probe tomography has been used to study the precipitation behavior of a 7XXX alloy[150,151]. However, the specimen preparation procedure is also very challenging and the region of interest that is observed in 3D is extremely limited.

In this study, Transmission X-ray Microscopy (TXM) has been employed to study the initiation and progression of corrosion damage in 4D non-destructively. TXM does not have extremely stringent specimen size requirements and enables the study of a statistically

relevant volume (FOV ~ 45 μm in this study) of material, where the observations can be scaled up to macro sized specimens. Alternate immersion experiments were performed on peak aged and highly overaged micropillar specimens to study the relevant corrosion mechanisms.

4.2 Materials and Experimental methods

Two Blocks of AA 7075-T651 were machined from the center of the thickness of a 76.2 mm (three inch) slab of AA 7075-T651. Block 1 was kept as is and was used to fabricate as received peak aged specimens. Block 2 was subjected to an over ageing heat treatment operation designed to grow the precipitates significantly. This involved solution treating the block at 510 C for a duration of 2 hours followed by water quenching. Next, the block was brought to an over aged condition by immediately ageing at 107 C for 6 hours and 163 C for 40 hours and furthermore, ageing at 300 C for 86 hours. This heat treatment protocol was the result of extensive heat treatment trials keeping in mind that the Transmission X-ray Microscope (TXM) has a resolution limit of 40 nm in our experiment. Hence, the precipitates were grown such that 95 % of the precipitates were beyond the 40 nm size minimum limit, as per calculations performed using SEM images of precipitates captured from FIB cross sections. Figure 22 shows the distribution of precipitate sizes as a function of ageing time as observed in the fabricated trial specimens.

Figure 23 shows the procedure involved in fabricating the micropillars used in this experiment. A diamond saw was used to fabricate rods with a square cross section from both blocks. Each rod was cut such that the longest dimension of the rod was parallel to the rolling axis (L) of the plate. Each needle had a cross section of 1 mm^2 and a length of

25 mm as in figure 23(b). The needles were then sharpened using a conventional polishing setup using a grinding wheel. 1200 grit SiC paper was used to achieve large amounts of material removal and fabricate the sharp tip at the top of the needle as seen in figure 23 (c). In order to ensure that the final fabricated pillars contained a population of Fe-rich inclusions in them, short absorption contrast tomography scans of the tips of each needle were obtained using a Zeiss Versa 520 system (Carl Zeiss Microscopy Inc. 1 Zeiss Dr. Thornwood, NY). The scans provided a 3D non-destructive view of the microstructure inside the needle tip and hence an understanding on the locations of the nearest Fe-rich inclusions. With the knowledge of the locations of Fe-rich inclusions in the pillar, fine diamond polishing of the needles could be carefully performed so as to accommodate the inclusions ~20 µm from the tip of the needle.

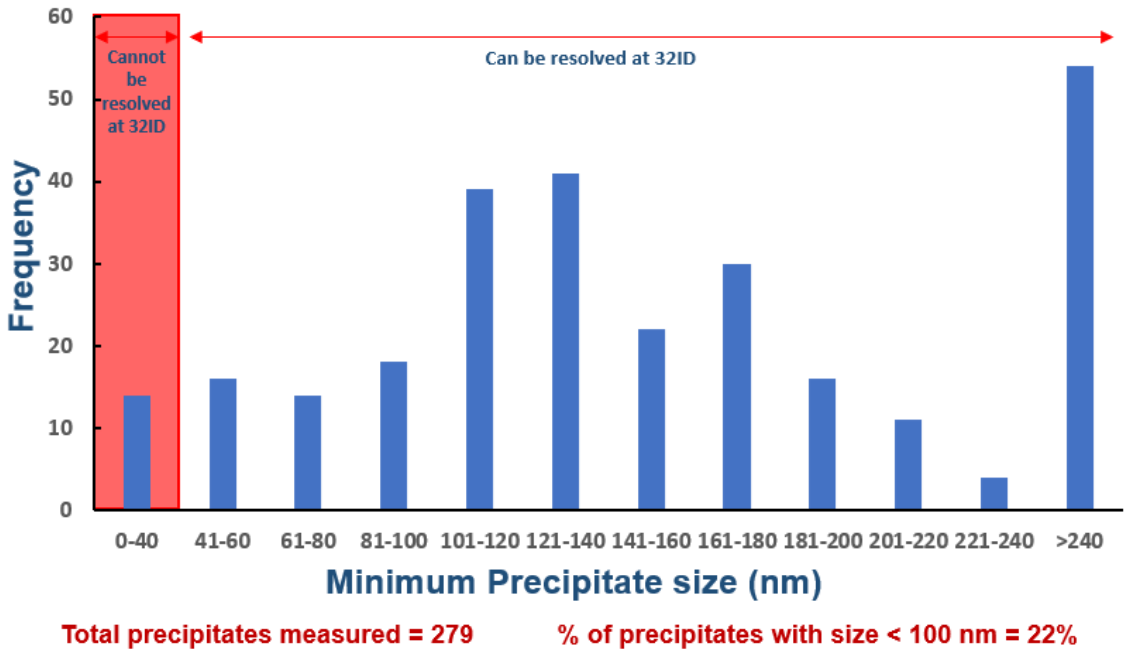

Figure 22: Size distribution of resolvable precipitates observed using the SEM. Precipitates below 40 nm could not be resolved during the TXM experiment.

A dual beam Zeiss Auriga Focused Ion Beam with a Ga+ ion source was used to fabricate large micropillars (15 -20 µm diameter and 30 µm height) from both the AA 7075-T651 needles as well as AA 7075 highly overaged needles. The needles were placed on a 45° specimen stub to mill the cylindrical portion of the pillar. A 16nA beam current was used to perform course milling of the pillars. Following this, finer currents from 4nA up until 1nA were used to obtain a cylindrical surface and fine surface finish. In order to obtain a flat and clean top for the micropillar, the stage was tilted such that the Ga+ beam would be orthogonal to the surface of the cylindrical polished face. A 2nA milling current was used to flatten the top of the pillar and subsequently the current was lowered to 1nA to obtain the final surface finish on the top.

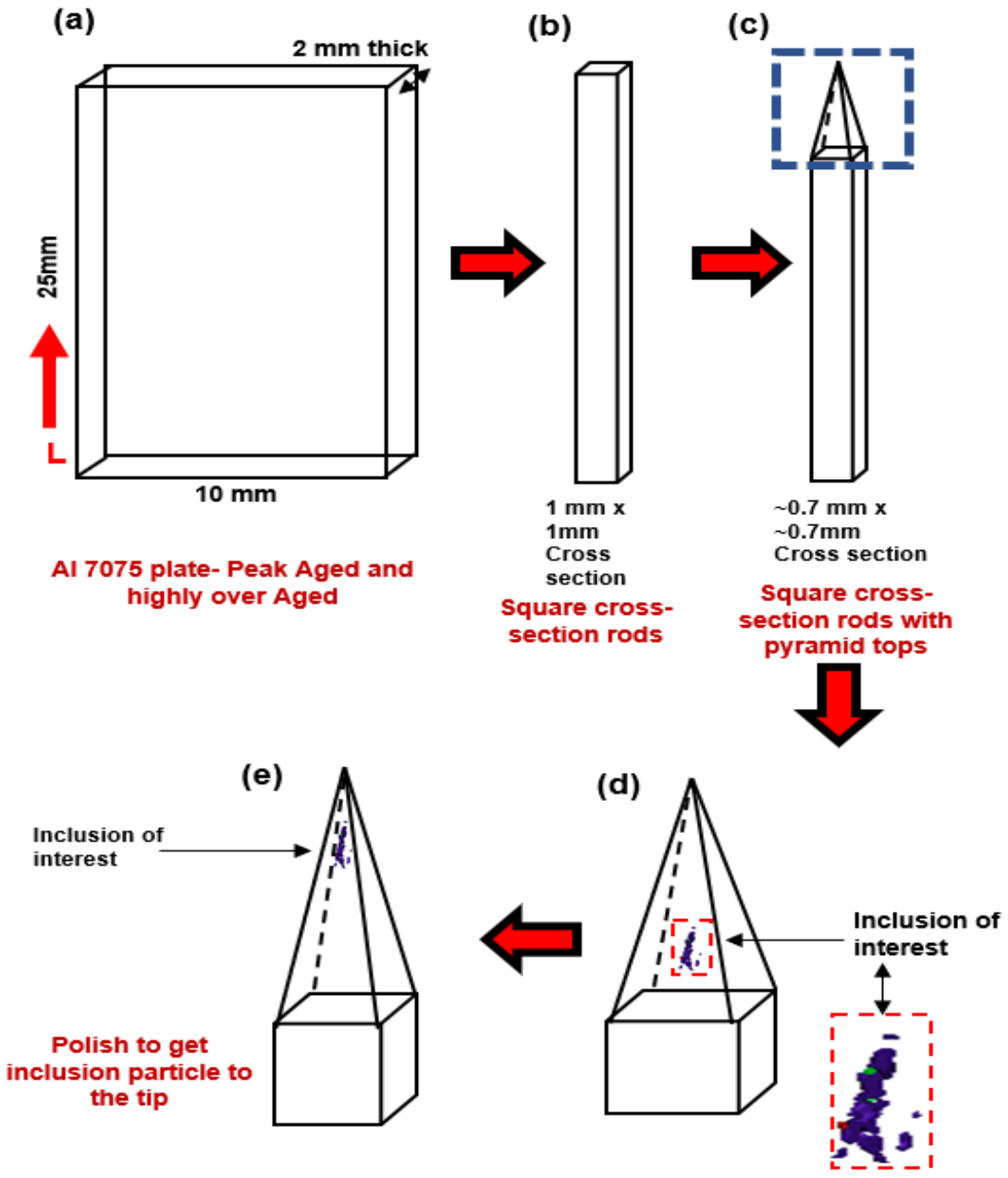

Figure 23: Procedure involved in the preparation of micropillars from rods of AA 7075

Figure 24 shows an example of a micropillar from a peak aged and a highly overaged needle. Note the clear visibility of precipitates (green arrows) and Fe-rich inclusions (red arrows) on the surface of the pillar.

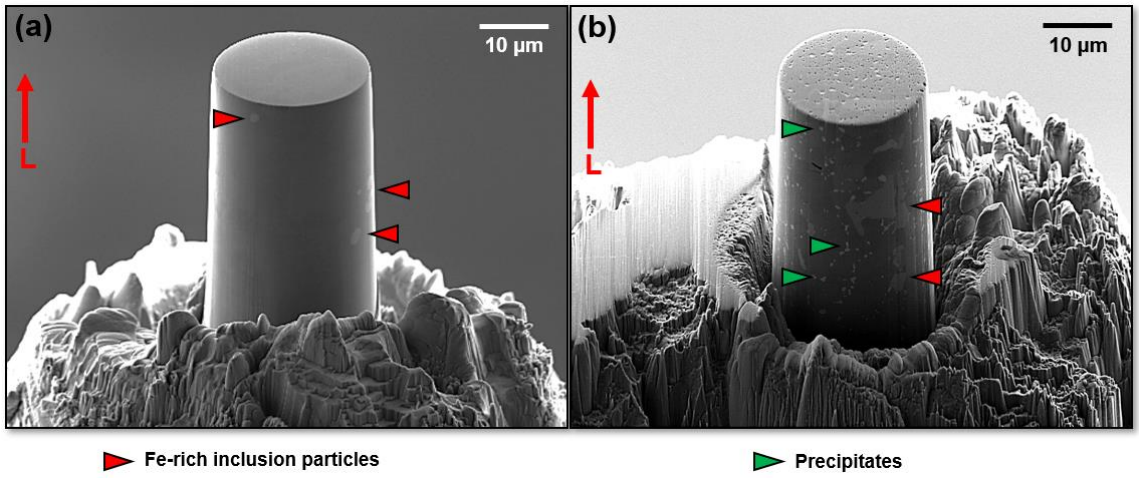

Figure 24: (a) Micropillar of AA 7075-T651 and (b) Micropillar of highly overaged AA 7075

Ex situ corrosion experiments were conducted on all the pillars at the 32-ID-C beamline at the Advance photon source at Argonne National Laboratory. Figure 25 shows a schematic of the geometry of the optics at the beamline. Due to the combination of a condenser lens and custom-made Fresnel zone plates, a pixel size of 18 nm could be achieved for this experiment with a camera binning value of 1. Further details about the beamline can be found elsewhere[86,152]. An x-ray energy of 9.75 keV was used during the experiment as it was above the Zn absorption edge. This ensured good contrast between the precipitates and the Fe-rich inclusions. Prior to the corrosion experiment, a pre-scan of the specimens was captured in order to obtain an understanding of the microstructure before corrosion. Each scan involved capturing 1200 projections over an angular range of 0-180 degrees with an exposure time of 1 second/ projection, thereby making the duration of each scan to be 20 minutes.

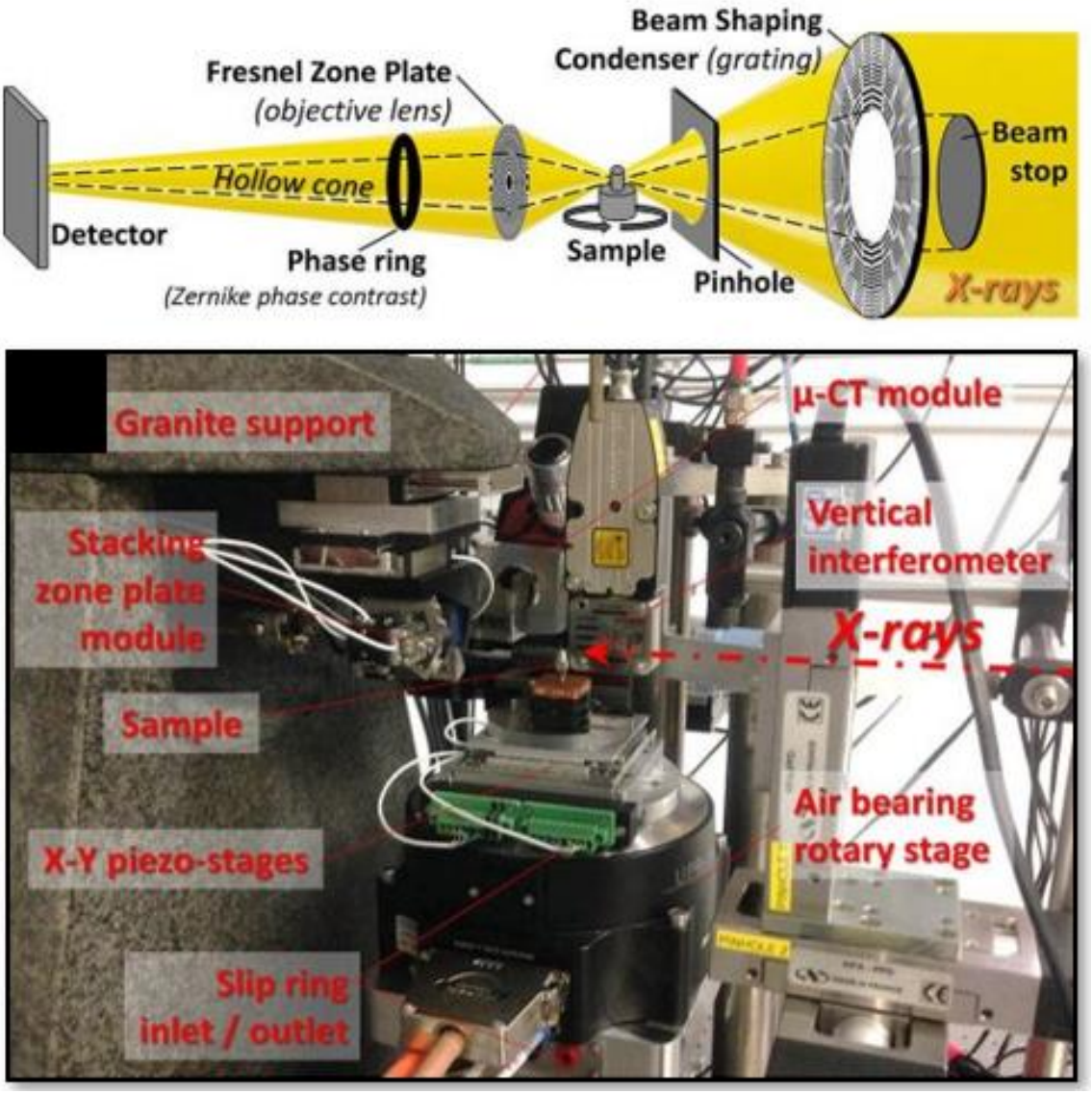

Figure 25: Schematic showing the components of the beamline at APS 32-ID-C[152]

The needles containing the micropillars were then subjected to an alternate immersion experiment wherein the entire needle was dipped in a corrosive fluid composed of neutral 3.5 wt.% NaCl solution. The needle was mounted on to a kinematic mount and care was taken to handle the mounts only using tweezers and not manually as the temperature of the body (being at a higher temperature than room temperature in the

beamline hutch) could lead to thermal drift during the tomography scans. Figure 26 shows the setup used to perform the alternate immersion experiment. Immediately after the pre-determined immersion times, the needle was rinsed with DI water and dried carefully with flowing nitrogen gas. The alternate immersion tests were conducted in conjunction with data reconstruction to visualize the corrosion damage mechanisms acting on the specimen as the experiment progressed. The process was stopped once an acceptable level of damage was achieved and the needles were carefully preserved for further correlative microscopy-based analysis.

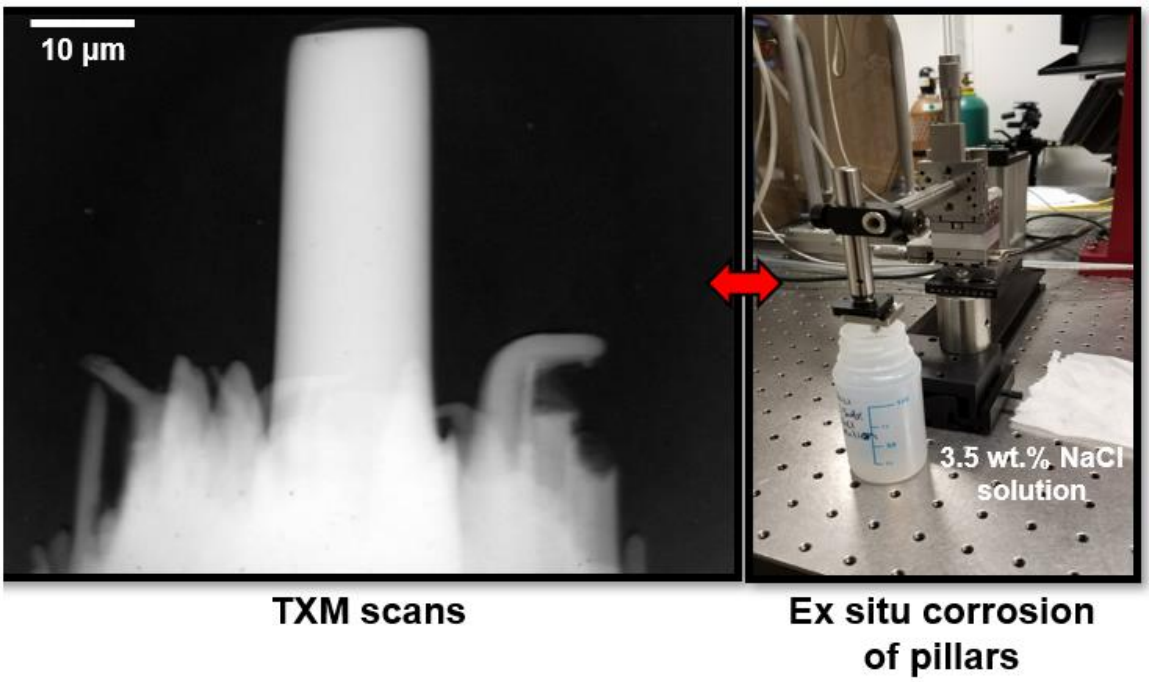

Figure 26: The alternate immersion experiment involved scanning the specimen using the TXM and alternate immersion of the pillars by using a custom made setup for immersion.

The datasets for both the peak aged and overaged specimens were reconstructed using Tomopy, a python-based toolbox used to reconstruct and analyze synchrotron tomography-based data. A filtered back projection algorithm was used to reconstruct the

projections into a reconstructed microstructure. The datasets were then cropped appropriately, and a series of filters were applied on the datasets to reduce noise and sharpen the data on Avizo 9 (Bethesda, MD). Non-local means was used to reduce noise in the data and unsharp mask was used to sharpen the relevant features in the images, such as the inclusion and precipitate particles. Non-local means is a denoising filter that involves searching for pixels of similar grey values (i.e pixels with grey values within a specified range) in a pre-determined area of interest in the dataset. Once the pixels are identified, the noise (i.e differences in the grey values) in each of these pixels is averaged out according to the variance law in probability theory. The unsharp mask filter involves creating a high pass filtered negative of the original image and combining it with the original to obtain a sharper image. A MATLAB (The MathWorks, Inc.) script written in-house was used for aligning the alternate immersion datasets to the original pre-corrosion dataset. Avizo 9was then further used to perform image segmentation on these datasets to visualize and quantify the distribution of precipitates, inclusions and the corrosion damage.

On completion of the alternate immersion tests, the pillars were characterized using the Zeiss Auriga Scanning electron Microscope. The tomography results showed extremely clearly the preference of corrosion in certain boundaries and certain grains over others. In order to study the pillar microstructure further and perform grain mapping, FIB and EBSD were used. Ga+ beam from the FIB at 1nA milling current was used to carefully mill the pillar starting from the top of the pillar along a direction parallel to the top face of the pillar, similar to the milling process involved in milling the pillar flat. The stage was tilted to 70° to face the EBSD detector. EBSD was performed at a landing voltage of 20 kV, 20 mm working distance, 120 µm aperture and using the high current mode. Additionally, Energy

Dispersive Spectroscopy (EDS) was performed on each of these slices to obtain the chemical composition of the inclusion particles, dispersoids and large precipitates. A landing voltage of 15 kV, 60 µm aperture and high current were used to obtain the EDS maps. Following this, trends relating to the misorientation of grain boundaries was correlated with corrosion damage observed in the pillars.

4.3 Results and Discussion

4.3.1 X-ray Tomography Data and Post Processing

Figure 27 shows a comparison of a slice from a highly over aged specimen before and after the application of the filtering scheme. The resultant dataset clearly has significantly lesser noise and has sharper features that aid in easy segmentation of the relevant features in the dataset.

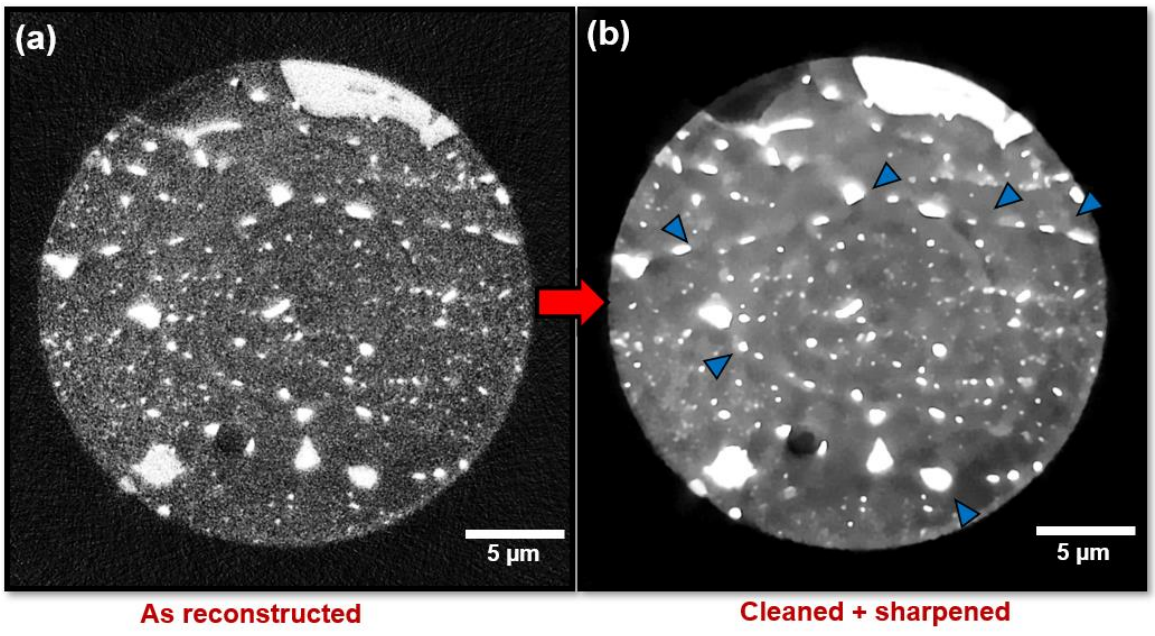

Figure 27: Comparison between as reconstructed slice vs the same slice filtered

Due to the high spatial resolution offered, TXM enables the 3D non-destructive visualization of precipitates that would otherwise require destructive 2D techniques and hence defeat the purpose of this study. Figure 27 shows precipitates located in orderly manner indicating the presence of a grain boundary as shown by blue arrows. It is also possible to identify the location of grain boundaries easily from these datasets. This was extremely helpful during the process involving EBSD to tomography dataset correlation.

4.3.2 Corrosion Visualization and Quantification

Figure 28 shows a comparison of the two pillars as shown in figure 24(a) and 24(b) captured using the SEM before and after the alternate immersion experiment. Both cases show significant surface damage in the form of general corrosion of the entire surface and localized attack as can particularly be seen in the highly overaged condition around the bright precipitates.

The tomography datasets were made to perfectly aligned so as to obtain one to one comparison of the datasets with increase in corrosion time. As a result, it was possible to compare the initiation and propagation of corrosion damage in the specimens. Figure 29 shows a virtual slice of the cross section of the pillar from the ST plane as a function of immersion time in the AA 7075-T651 pillars. A number of microstructural features become apparent on witnessing the corrosion behavior on this slice with time. The Al_2CuMg particle as shown by the red arrow is observed to shrink in size with continue immersion time. Al_2CuMg particles undergo anodic dissolution when in contact with 3.5 wt.% NaCl solution leading to the removal of Al and Mg to leave behind a spongy Cu remnant. This remnant has been shown behave cathodically with respect to the matrix until the matrix around the particle undergoes dissolution.

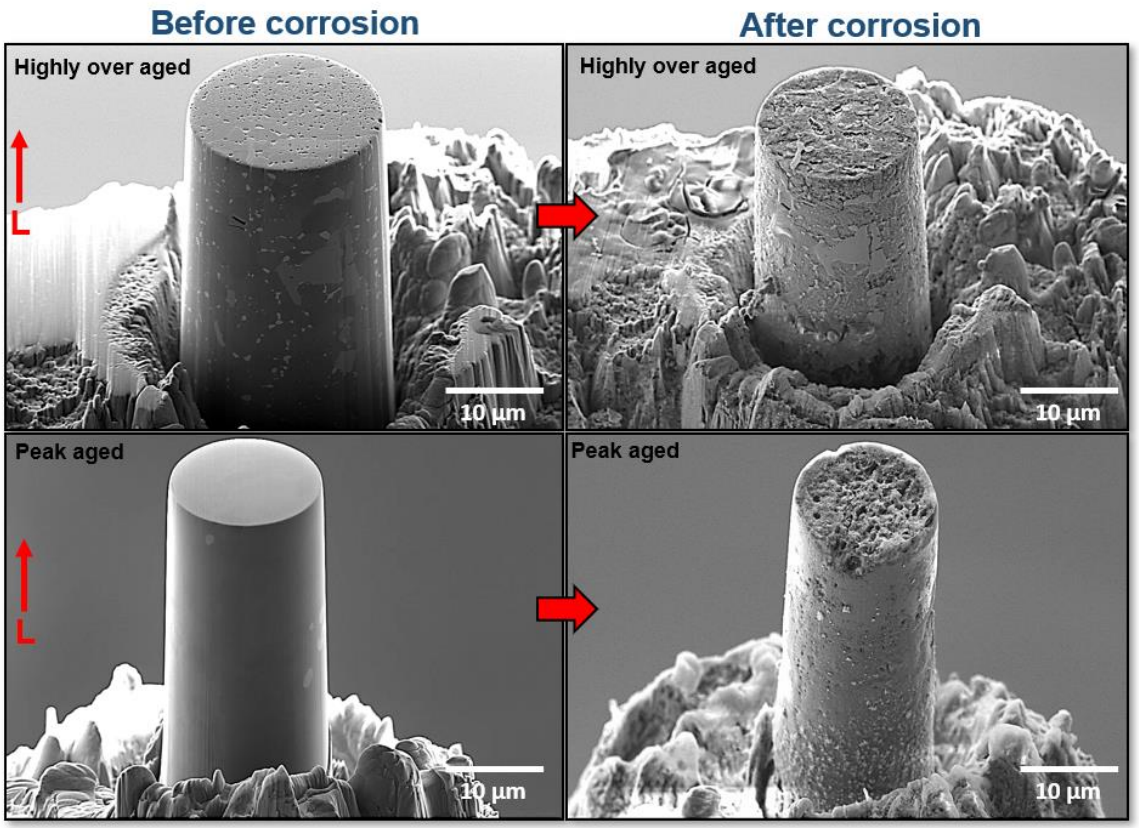

Figure 28: A comparison of the peak aged and highly overaged pillars before and after corrosion documented using the SEM

Once the electrical contact between the particle and matrix is eliminated, the pit formed by the particle becomes inactive and the particle can be removed in chunks over time or completely get removed at once. Additionally, interestingly, another particle cluster is seen shown with blue arrows is observed to allow trenching around itself. This particle is observed to be an Fe-rich inclusion cluster that leads to the formation of a trench around itself leaving a deep trench around itself with observable corrosion product inside the trench. Interestingly, another bright inclusion particle appears to be completely immune to any form of corrosion attack (yellow arrows).

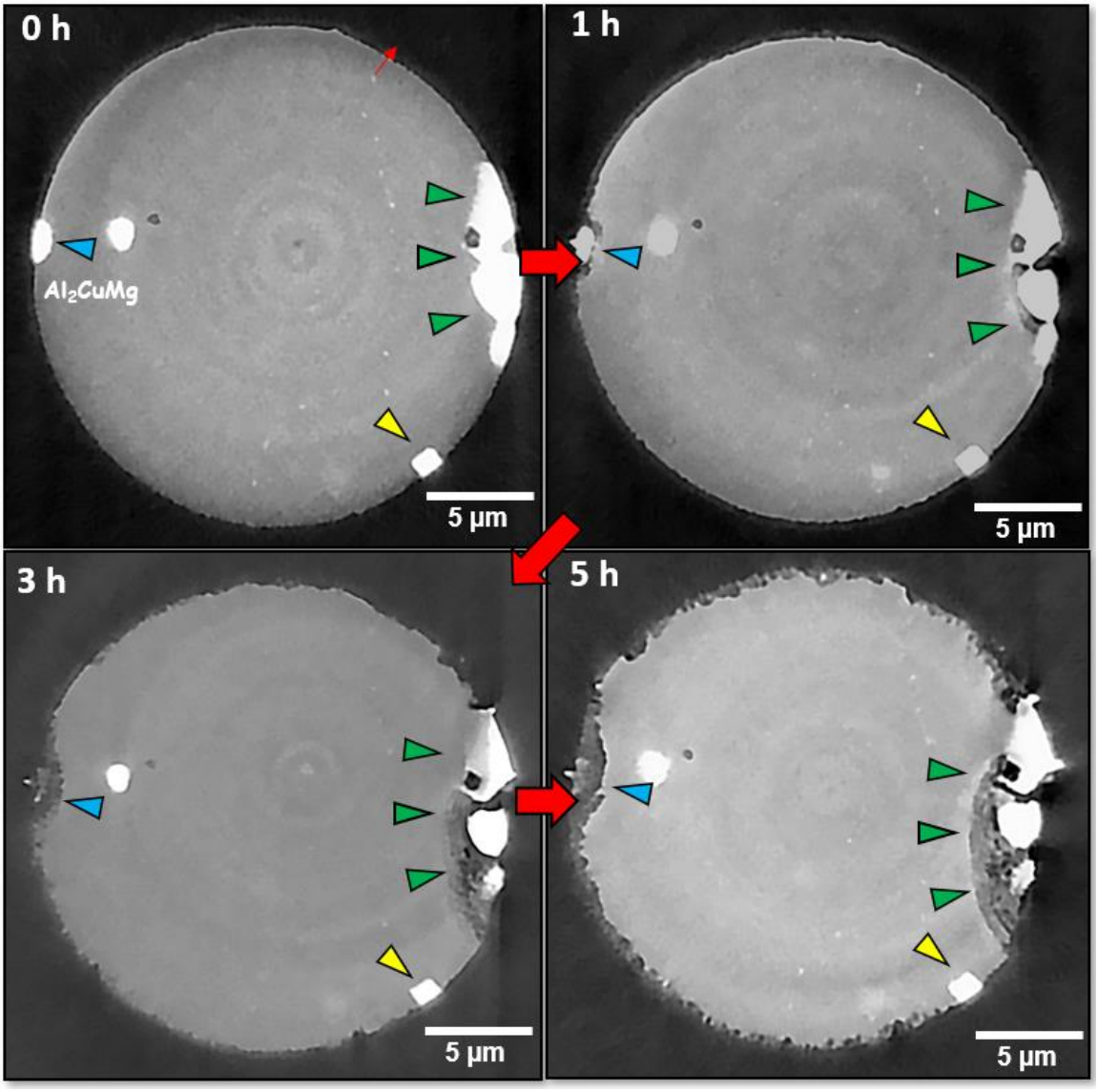

Figure 29: Virtual slice cross section of the ST plane showing progress in corrosion damage with immersion time (0, 1, 3 and 5 hours). Blue arrows show the Al2CuMg particle, green and yellow arrows show an Fe-rich inclusion particle.

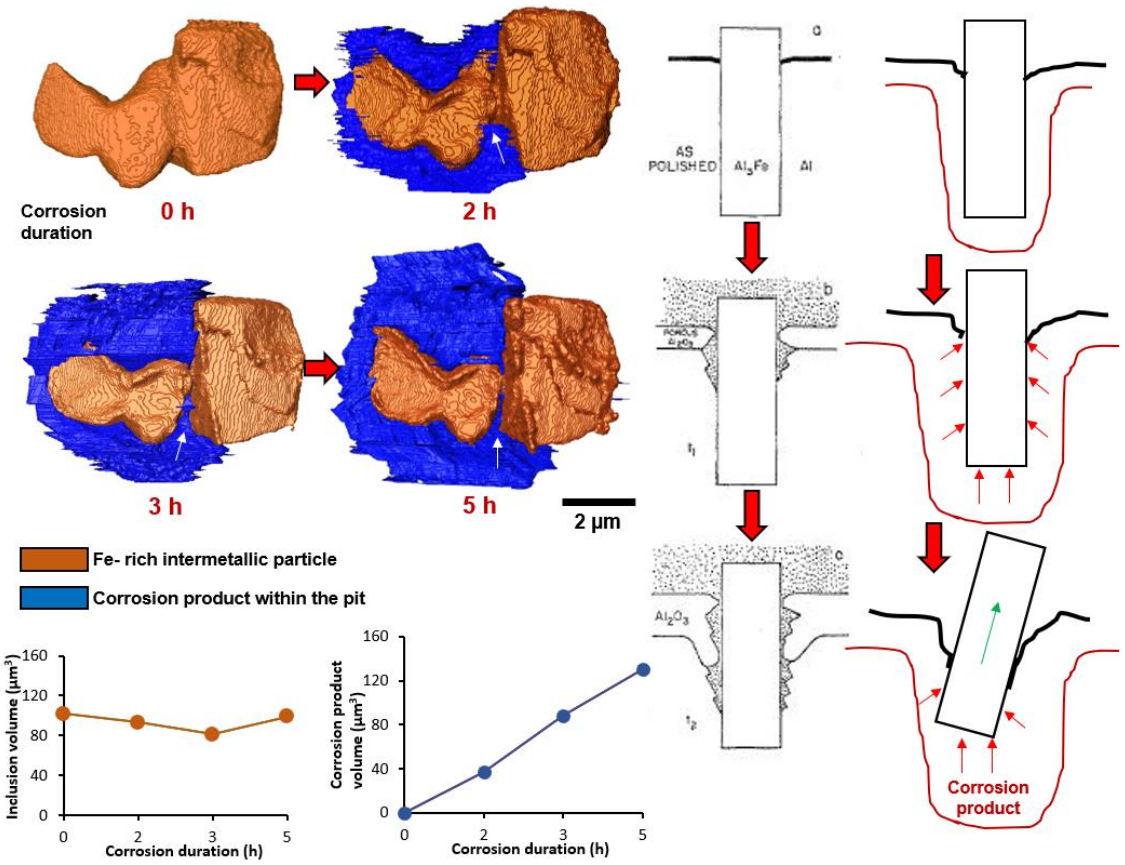

Figure 30: Evolution of localized corrosion around the Fe-rich inclusion cluster from figure 29. Inclusion volume is seen to be relatively constant while the amount of corrosion product is measured to increase linearly. The dissolution model proposed by Metzger and Zahavi are improved upon using observations from this particle.

Figure 30 shows the local evolution of the corrosion damage around the particle through the use of a segmented volume rendering of the inclusion particle looking face on from the side. It can be clearly seen that the particle leads to the formation of a large volume of corrosion product underneath itself that is shown in blue in the rendering. In the last dataset that was captured for this specimen, the particle was still held in place with the matrix. However, give more corrosion time, it is possible that the particle could have

debonded from its neighboring matrix leaving behind a pit filled with corrosion product. While the particle is still held by the matrix, due to the fact that the corrosion product has a volume greater than the aluminum matrix that forms the product, this corrosion product formation underneath the particle would apply a net resultant stress orthogonal to the outer surface on the particle that could lead the particle to debond and further exacerbate trenching around the particle. Once the particle is completely unattached to the matrix, the particle could be entrapped in the corrosion product and not contribute to the pit growth process underneath. The matrix dissolution and particle removal can be compared to that proposed by Zahavi et. al. Due to the fact that continued corrosion around and underneath the particle is visible, the model can be further extended to include the formation of corrosion product underneath and due to the large volume of the product as compared to the matrix, the inclusion particle can experience a stress, pointing radially outward in this case.

The highly overaged needles showed interesting corrosion attack as well. The behavior of the precipitates vs cathodic inclusions is very noteworthy. Figure 31 shows an example of a comparison of the same slice in 5 different aligned datasets of the specimen with an increase in immersion time. Cathodic trenching around precipitates near the surface is seen to be the method by which corrosion begins to initiate in this ageing condition. Additionally, extensive networks of intergranular corrosion are seen to form with increase in corrosion duration. Figure 32 shows another example of a slice from all the datasets. The Fe-rich inclusion indicated by the red arrows shows little to no trenching around it while the rest of the specimen undergoes extensive intergranular corrosion. Another interesting aspect of the corrosion observed in both the peak aged and the highly overaged specimens

is the time of exposure to the corrosive fluid. Note the amount of time the highly overaged specimen was exposed to (total of 17.5 minutes) as opposed to the amount of time the peak aged as received specimen was exposed to (total of ~5 hours) to show the amount of corrosion damage as seen.

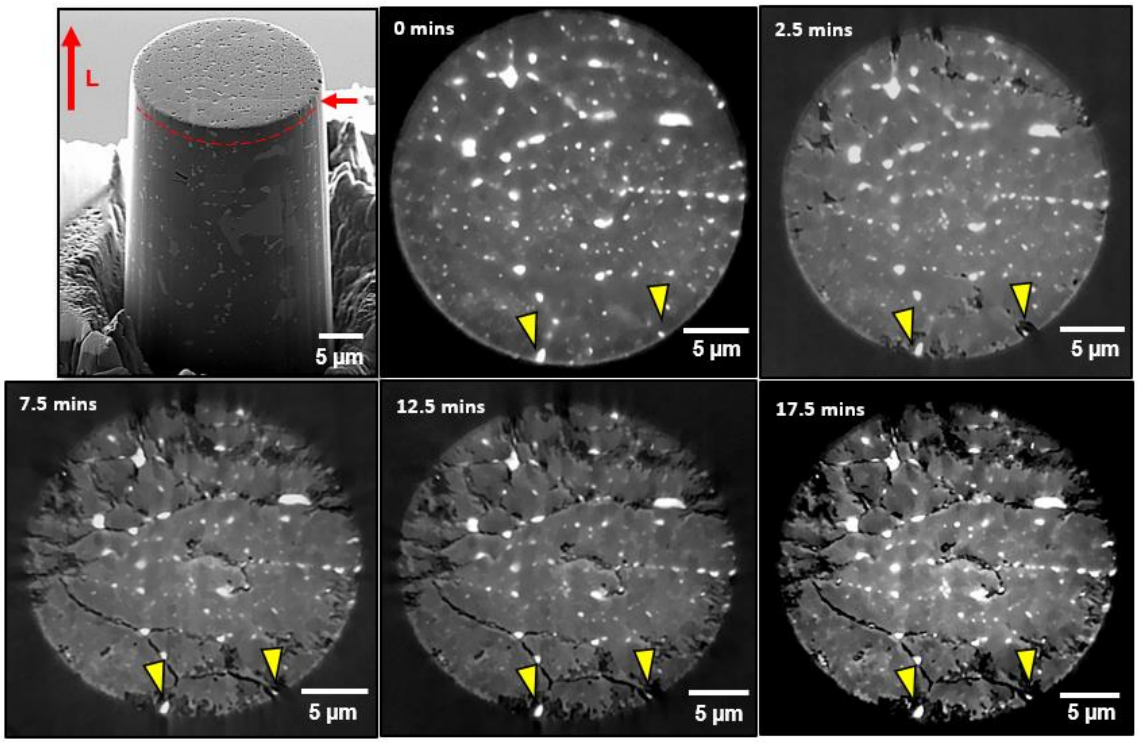

Figure 31: Example of corrosion damage seen in highly overaged specimens along the ST plane. Yellow arrows show example locations of initiation of intergranular corrosion at grain boundaries indicating significant trenching around these particles.

This implies two aspects pertaining the corrosion behavior of the two ageing conditions, a) The precipitates are significantly more active in the highly over aged specimen, behaving strongly cathodic to the matrix and b) the Fe-rich inclusions that are generally observed to play a strong role in initiating pitting corrosion in the peak aged condition are seen to play a secondary role as compared to the precipitates which dominate

as the leading cathodic constituent particles in the matrix and grain boundaries. Interestingly, the susceptibility to intergranular corrosion in overaged AA 7075 has been reported to be lesser than that in peak aged AA 7075[108,153]. Goswami et. al also reported a higher resistance to SCC in overaged AA 7075 and attributed it to the increase in corrosion potential of the precipitates and hence led to a decrease in driving force for anodic dissolution, due to increased Cu content[104]. Sun et. al studied the intergranular corrosion and SCC susceptibility of peak aged, overaged and highly overaged alloy and reported that while the overaged specimen had a higher resistance to IGC, the highly overaged specimen showed substantial intergranular corrosion[149]. They hypothesized that a mechanism change occurs between overaged and highly overaged specimens which impacts intergranular corrosion and SCC susceptibility. The significant increase in Cu content from peak aged to over aged condition and beyond can explain this increased susceptibility. The precipitates behave substantially more cathodically as a result of the increase Cu content. So much so, that they appear to be the dominant cathodic particles in the microstructure, more so than the Fe-rich inclusions which seems to not undergo trenching around themselves, given the corrosion duration. This chain of cathodic precipitates that decorate the grain boundaries makes it conducive for intergranular corrosion to initiate and propagate.

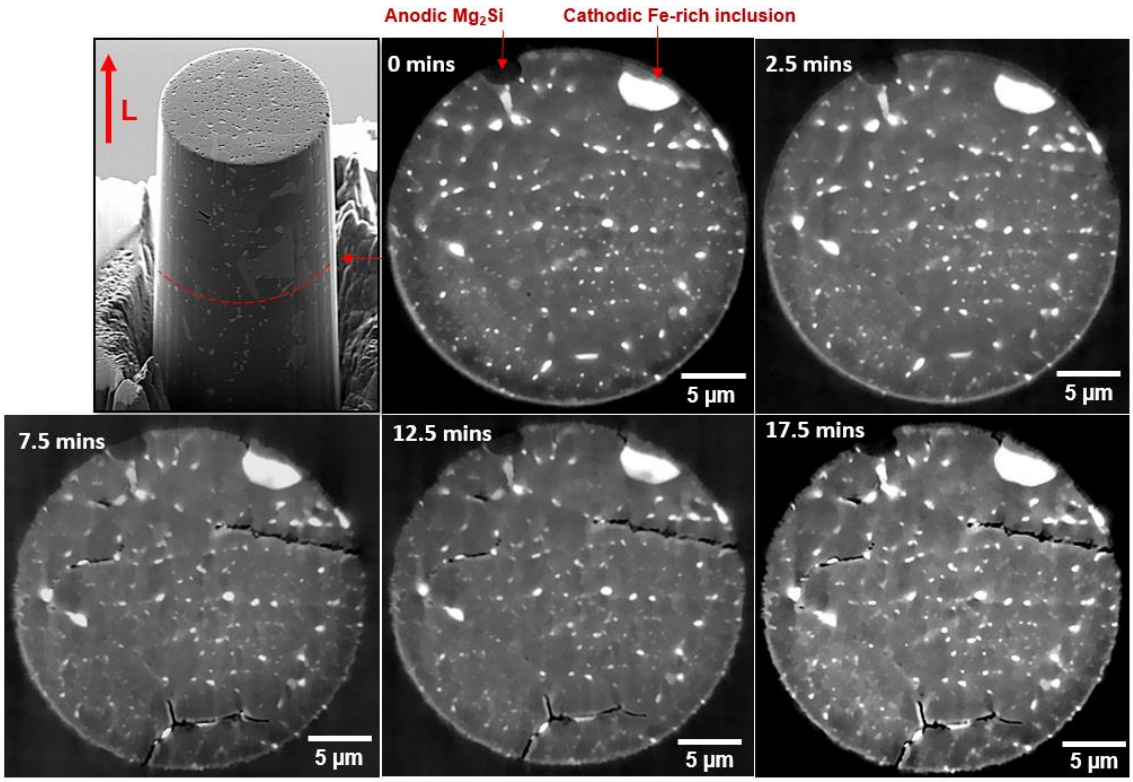

Figure 32: Another example of corrosion damage observed in highly overaged specimens along the ST plane. Fe-rich inclusion particle is observed not play as important a role in this specimen compared to the precipitates.

Certain grain boundaries and grains are observed to be far more susceptible to intergranular corrosion / grain dissolution compared to others in both ageing conditions. This behavior is hypothesized to be due to differences in grain orientation and grain boundary misorientation. In order to understand this discrepancy, a serial sectioning EBSD procedure was employed in order study the grain structure at different portions of the pillar. Owing to the fact that the region of interest was small, the step size for each EBSD scan could be minimized significantly. Figure 33 shows an SEM image looking at the ST plane of the pillar showing signs of intergranular corrosion. Additionally, included are the grain

map and the grain boundary misorientation map. On this slice, it is very evident that the high angle grain boundary shown running across the center of the pillar is the most preferred boundary for intergranular corrosion.

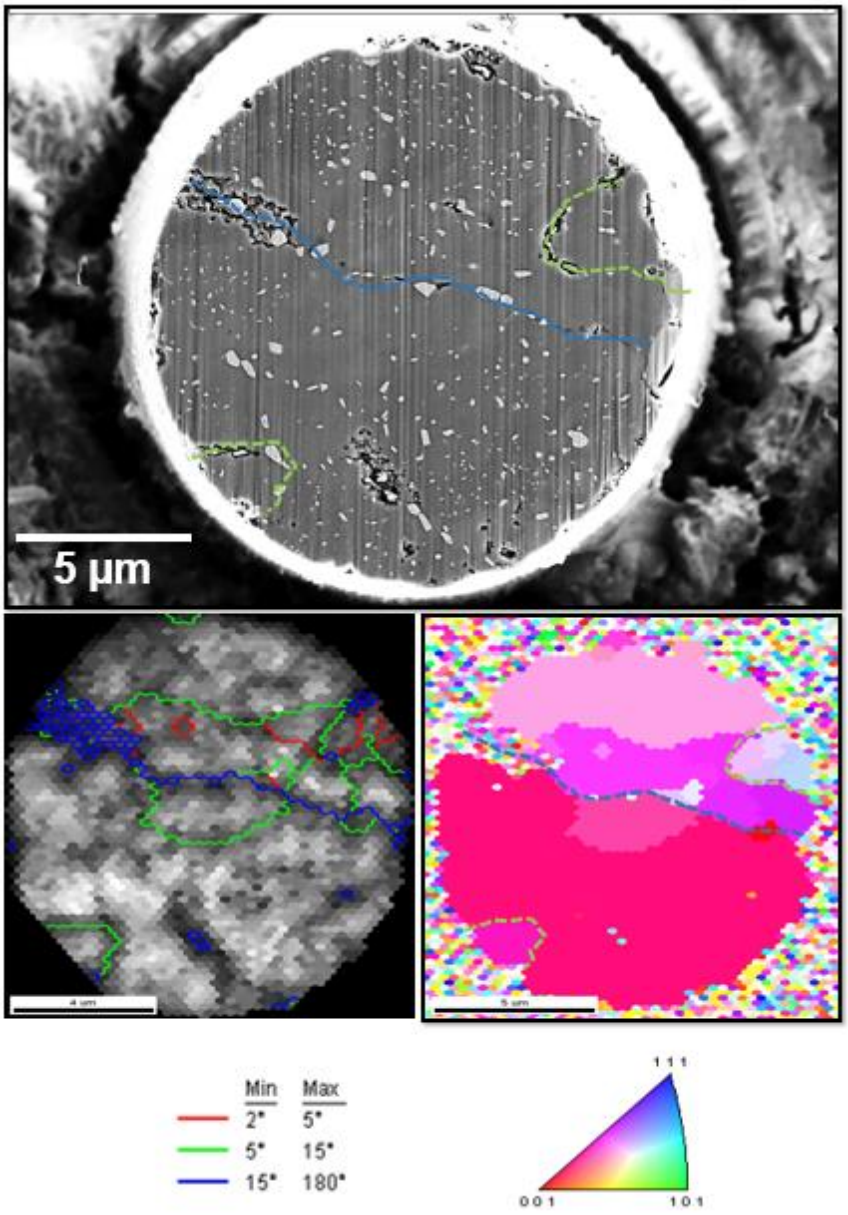

Figure 33: SEM image and corresponding IPF and grain boundary misorientation maps for a serially sectioned slice of a highly overaged pillar. Intergranular corrosion preference is abundantly clear with the high angle grain boundary (blue dotted line) corroding

diametrically through the pillar. Low angle grain boundaries (green dotted lines) selectively undergo intergranular corrosion.

4.4 Summary

Transmission X-ray microscopy of AA 7075-T651 and highly overaged AA 7075 subjected to alternate immersion tests was performed in this study. The high spatial resolution offered by this technique enabled the observation of microstructural second phase particles such as precipitates in 3D non-destructively. Extensive intergranular corrosion and grain dissolution was observed, and this was correlated with ageing condition and grain structure. Precipitates in the highly overaged condition are seen to be much more cathodic compared to the peak aged condition and assist in exacerbating the intergranular corrosion by acting as the dominant cathodes in the specimen. Grain orientation measurements with the EBSD after corrosion indicate a clear preference for high angle grain boundary corrosion.

CHAPTER 5

4D MICROSTRUCTURAL CHARACTERIZATION OF CORROSION AND CORROSION-FATIGUE IN A TI-6AL-4V / AA 7075-T651 JOINT IN SALTWATER

5.1 Introduction

Aluminum 7XXX alloys are used extensively in aeronautical and naval applications due to their high strength-to-weight ratio. These alloys are exposed to harsh in-service conditions such as a corrosive environment, mechanical stresses, and varying ambient temperatures, often acting simultaneously. Multiple aircraft teardown analyses have revealed the synergistic combination of corrosion and fatigue to be very detrimental to the performance of the aluminum alloys in service [7,154,155]. The corrosion and mechanical behavior of AA 7XXX alloys has been studied in detail over the last few decades [28,31,65,103,156–159]. Much of the open literature has focused on trying to understand the microstructural features that contribute to the initiation and propagation of damage in 7XXX aluminum alloys. AA7075, which is the alloy of interest (as the anode) in this study, contains second phase particles that strongly influence the corrosion and cracking performance of the alloy. These second phase particles have a composition different from the aluminum matrix and can be primarily of 3 types: (a) metallic inclusions, (b) dispersoids, and (c) precipitates. Each of these particles are of different sizes (metallic inclusions > dispersoids > precipitates) and have a critical role to play in determining the corrosion behavior of the alloy and its performance in service. In a saltwater environment, Fe-rich inclusions are cathodic to the aluminum matrix and cause pitting corrosion locally

via trenching [22,27]. On the other hand, particles such as dispersoids, Mg- rich inclusions and precipitates are anodic to the aluminum matrix [104,105]. Additionally, inclusion particles play a strong role in determining the mechanical behavior of the alloy and can act as crack initiation sites. When these alloys are subject to stress corrosion cracking or corrosion-fatigue, in service, pits that nucleate as a result of these metallic inclusions can act as crack initiation sites and lead to premature failure [58].

The corrosion behavior in alloy couples containing aluminum alloys has been experimentally investigated primarily using electrochemical methods and in two dimensions (2D). Fastener-plate specimen couples are a particularly unique subset of dissimilar alloy couples due to their complex geometry. Area ratio, nature of the corrosive environment, composition of alloys, and their individual corrosion potentials affect the magnitude of galvanic corrosion damage observed between a variety of cathodic materials couples with AA7075[160–162]. Computational methods in combination with experiments have been key in improving our understanding of the corrosion behavior of galvanic couples. Techniques such as phase field modeling and FEM have been used to map the local pH, potential, and galvanic current density distribution in a variety of specimen geometries [163–167].

Destructive techniques prevent the observation of microstructural evolution during the initiation and propagation of corrosion during the course of the experiment. Additionally, disassembling the geometry to study the corroded anode can disturb the structural integrity of the specimen geometry and potentially lead to the damage of the remnant specimen and loss of corrosion product. Owing to the complexity of the geometry, employing 2D methods to study corrosion damage in the remnant anode can be limiting.

2D methods severely restrict the surface area of the anode that can be imaged (without further destroying the anode specimen), require cleaning methods to clear out the obscuring corrosion products and provide no information about corrosion attack below the surface. Moreover, the use of 2D imaging techniques for analyzing and modeling cracks can grossly under-estimate the actual size of the crack underneath the surface [114]. All these factors can severely limit our understanding of the corrosion process in such complex geometries. Due to these reasons, 3D non-destructive characterization techniques are needed to study corrosion damage in these geometries.

X-ray computed tomography has evolved into an excellent technique to study the microstructure of materials non-destructively and in 3D. Absorption contrast tomography is particularly well suited to study microstructural evolution and damage in a variety of material systems. Aluminum alloys have been studied quite extensively using computed tomography techniques. Specifically, processes such as initiation and propagation of corrosion, stress corrosion cracking, and corrosion fatigue have been examined in 2XXX and 7XXX alloys [16, 26–28].

X-ray computed tomography is ideal for studying the microstructure and evolution of damage in fastener-plate joints as it has the potential to provide high resolution 3D data non-destructively. This enables the experimenter to perform multiple iterations of corrosion and quantify the initiation and propagation of damage on the mating surfaces inside the plate. Additionally, localized corrosion due to the presence of intermetallic particles within the aluminum alloy plate can be visualized as well. Recently, the viability of using synchrotron x-ray tomography to study corrosion fissure formation in a AA7050/Stainless steel couple, replicating a rivet-plate couple exposed to saltwater

environments, has been demonstrated [119,170]. The presence of a dense fastener can cause image aberrations such as metal artifacts and beam hardening. Furthermore, time at synchrotron facilities is limited, so most corrosion experiments at the synchrotron are accelerated and of relatively short duration.

A dissimilar alloy couple of AA 7075-T651 plate fastened with a Ti-6Al-4V screw was studied in this paper. Ti-6Al-4V has been shown to drastically exacerbate corrosion attack when in contact with AA 7075 [162,171]. The experiments were conducted with a lab-scale source to study the evolution of damage, *ex situ*, up to a long period of time, i.e., 20 days. A comprehensive understanding of how the microstructure evolves in these materials during the corrosion process is lacking. Critical information such as the role of intermetallic particles on the surface and bulk of the aluminum alloy anode, initiation of pits in the region between the male and female threads and how material loss occurs in such alloy couples is still not understood. To address this concern, corrosion testing of the alloy couple was conducted by exposing the specimen to a saltwater environment in this study. 3.5 wt.% NaCl solution was used to replicate sea water conditions. No surface protective coatings were used to be able to simulate the worst-case scenario in the couple geometry. X-ray absorption contrast tomography enabled the visualization of corrosion initiation and propagation non-destructively for a period of 20 days. The datasets obtained at increasing corrosion times were analyzed to quantify the magnitude of corrosion damage with respect to corrosion time and location.

Additionally, cracking behavior of dissimilar alloy couples warrants further understanding and attention from the community. If the corrosion damage is aggressive enough and goes undetected, multiple pits within the alloy couple geometry can act as

crack initiation sites depending upon the nature of applied mechanical stresses. In this study, uniaxial corrosion-fatigue was performed on the 20 days corroded specimen to microstructurally examine the crack initiation and propagation behavior in the couple. Crack initiation sites were identified during failure analysis of the fractured specimen and were correlated with their respective positions in the specimen volume prior to fracture using the x-ray tomography data.

5.2 Materials and Experimental Procedure

The dissimilar metal couple specimen was comprised of two components namely an AA 7075-T651 anode and Ti-6Al-4V cathode. Plates of AA 7075-T651 (Alcoa, New York, NY, USA) were electro-discharge machined from the center of the thickness of a commercially available 25.4 mm thick block, as shown in Figure 34 (a). The longest dimension of the plate specimen was oriented along the Long-Transverse (LT) direction. An M1x0.25 threaded hole was machined into the center of the width of the plate specimen. The plate was mechanically polished with 600 and 1200-P4000 grit SiC polishing paper. The plate was further fine polished down to a 1 µm diamond finish. The specimen was thoroughly cleaned with isopropyl alcohol and sonicated to obtain a contaminant- free surface and threading.

A commercially available M1x0.25 screw of Ti-6Al-4V (US-microscrew, Seattle, Washington, USA) was fastened to the AA 7075-T651 plate as in fig. 34 (b). Tables 2 and show the composition of the as-received AA7075-T651 and Ti-6Al-4V specimen as reported by the supplier and as measured *via* Energy Dispersive Spectroscopy (EDS) for comparison.

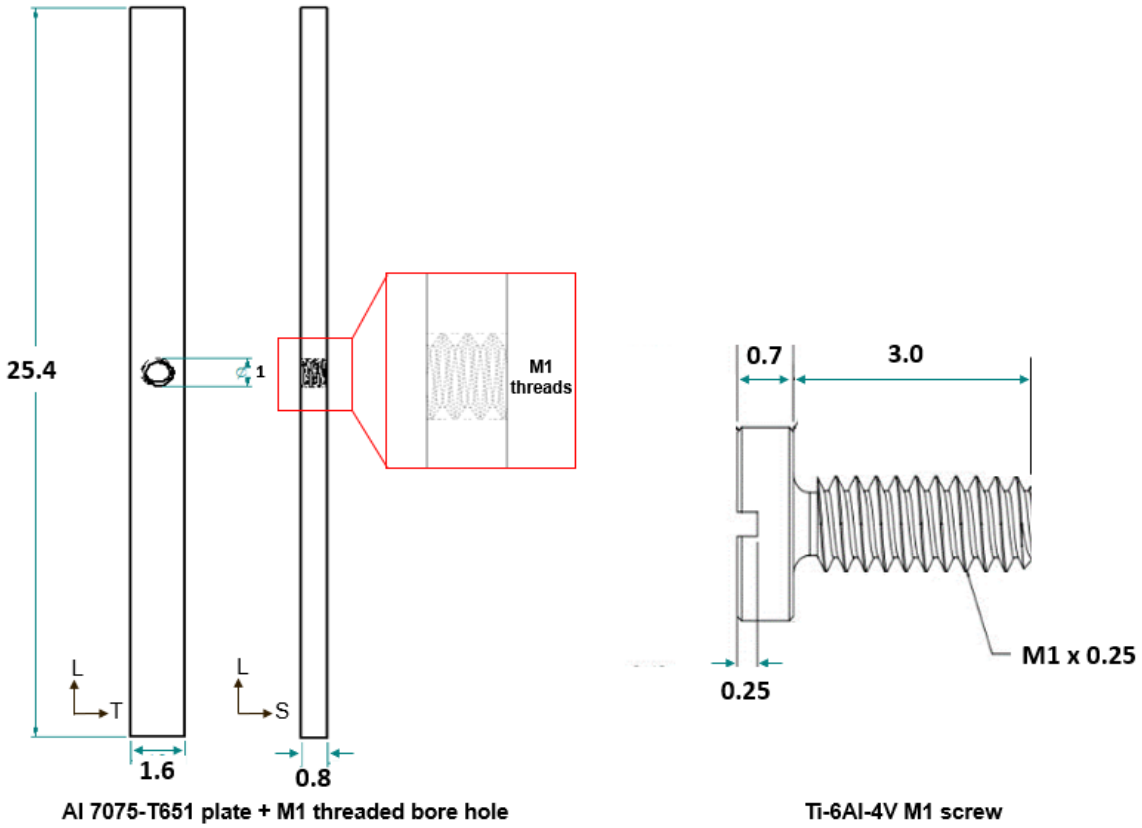

Figure 34. Schematic showing the geometries of the AA 7075-T651 plate and Ti-6Al-4V screw (All dimensions in mm)

Table 2: Elemental Tolerances (ASTM B209-14) and Measured Chemical Composition of the AA 7075-T651 Block

AA 7075- T651: Chemical composition(wt.%)									
	Si (max)	**Fe (max)**	**Cu (range)**	**Mn (max)**	**Mg (range)**	**Cr (range)**	**Zn (range)**	**Ti (max)**	**Al**

ASTM B209-14	**0.4**	**0.5**	**1.2–2.0**	**0.3**	**2.1-2.9**	**0.18-0.28**	**5.1-6.1**	**0.2**	**Bal**
Measured	**0.2 ± 0.03**	**0.2 ± 0.04**	**1.5 ± 0.07**	**0**	**2.3 ± 0.03**	**0.2 ± 0.03**	**5.9 ± 0.11**	**0**	**Bal**

Table 3: Elemental Tolerances (ASTM B265-15) and Measured Chemical Composition of the Ti-6Al-4V Screw.

Ti-6Al-4V: Chemical composition(wt.%)								
	Al (range)	**V (range)**	**Fe (max)**	**C (max)**	**O (max)**	**N (max)**	**Others (max)**	**Ti**
ASTM B265-15 (wt.%)	**5.5 - 6.75**	**3.5 - 4.5**	**0.4**	**0.08**	**0.2**	**0.05**	**0.4**	**Bal**
Measured	**6.0 ± 0.12**	**4.1 ± 0.09**	**0.15 ± 0.03**	**0 ± 0.04**	**0**	**0**	**0.2**	**Bal**

The Ti-6Al-4V screw was carefully screwed into the AA 7075 plate to prevent the formation of scratches on the plate surface and a snug fit was ensured. Regions of the couple specimen geometry were covered with rubber cement to allow a specific area of the couple to be exposed to the corrosive fluid. This exposed region of the couple specimen was chosen as the region of interest for corrosion and the subsequent tomography scans. The precise masking with the rubber cement ensured a cathode/anode area ratio of 0.5.

An alternate immersion corrosion experiment was performed on the couple in a bath containing 3.5 wt.% NaCl solution (pH=7). The specimen was positioned such that the region of interest was completely immersed in the NaCl solution throughout the duration of the corrosion experiment. The progressively dropping level of the corrosive fluid (due to evaporation) was replenished with deionized (DI) water. The specimen was corroded for a period of 5 days at a time for a total of 20 days. After each 5 day period of corrosion, the specimen was cleaned with DI water and dried with compressed air to ensure that no corrosive fluid was retained in the crevices within the threading of the couple specimen.

X-ray microtomography Full Field of View (FFOV) scans were conducted prior to performing corrosion and at the end of each five-day period of corrosion, thereby yielding a total of 5 tomography datasets with an increasing magnitude of corrosion damage. X-ray microtomography scans of the region of interest were conducted using a lab-scale Zeiss Versa 520 system (Carl Zeiss Microscopy Inc. 1 Zeiss Dr. Thornwood, NY). An accelerating voltage of 80 kV was used for all the scans, during which 1600 projections were captured with an exposure time of 1 second per projection. A voxel size of 1.7 μm was achieved using the 4X objective lens and a camera binning of 2. Following the scan, the dataset was reconstructed using an in-built filtered back projection algorithm and corrected for beam hardening artefacts. ImageJ [172] was used to filter the as reconstructed tomograms. A combination of the anisotropic diffusion filter and unsharp mask were used to denoise and sharpen the images respectively. Avizo 9.0 (Bethesda, MD) was used to visualize, segment and quantify various features of interest in the datasets. A combination of the region-grow technique and the paint brush tool was used to segment the inclusions

and pits within the corroded microstructures to understand the role of corrosion time on pit initiation and growth. The label analysis tool was used to quantify the volume, surface area, and number of pits at each timestep.

Once 20 days of corrosion were completed, the couple specimen was subject to corrosion-fatigue to understand the mechanism of crack initiation and propagation. Corrosion fatigue of this specimen was conducted using a loading fixture that was custom built and tested at the Center for 4D Materials Science. The loading fixture is comprised of a stepper motor connected to a linear actuator that was responsible for applying the load on the specimen *via* specially designed 440 steel grips. Further details about the loading fixture can be found elsewhere [68]. A specially designed miniature bath comprising of a Kapton tube and PEEK base were mounted onto the specimen close to the region of interest. The bath was made leak-proof and held in place using epoxy. 3.5 wt.% NaCl solution was poured into the bath using a dropper, thereby exposing the region of interest to the corrosive environment during the fatiguing process

Corrosion-fatigue was conducted at an R-ratio of 0.1 with a s_{max} of 200 MPa being well within the elastic limit for LT AA 7075-T651(475 MPa along the L direction). A loading frequency of 1 Hz and a sinusoidal waveform were used. The specimen was corrosion-fatigued to failure. The fracture surface of the specimen was thoroughly cleaned with 3% HNO_3 [173] to clear out any remnant oxide that could inhibit the fracture surface from being imaged. Tomography scans of each half of the fractured specimen were captured to enable further analysis pertaining to crack initiation sites.

A correlative approach was used to link the initiation and propagation of damage with fractographic analysis. Fractography was performed on the fracture surfaces of the

failed specimen using a dual-beam Zeiss® Auriga focused ion beam (FIB) workstation. Locations of initiation of the fracture-inducing cracks were determined and an understanding of the various stages of the fatigue crack propagation were mapped out. Combining this with the tomography data, before and after specimen failure, the precise locations for crack initiation were obtained. Following this, the mechanisms leading to crack initiation and crack propagation were examined.

5.3 Results and Discussion

5.3.1 Microstructural Characterization of the Aluminum Alloy 7075-T651 Plate (Anode)

The AA7075-T651 alloy used for this study is composed of intermetallic inclusions, dispersoids, and precipitates distributed throughout the Al rich matrix. Figure 35 shows a secondary electron micrography of a representative region of the microstructure that contains metallic inclusions and dispersoids. EDS was used to confirm the composition of the inclusions to be Fe-bearing: Al_7Cu_2Fe (Size of top 25% by volume: 13.2 µm[L], 10.9 µm [T], 6.5 µm [S]) and $Al_{23}Fe_4Cu$(Size of top 25% by volume: 12.3 µm[L], 11.7 µm [T], 6.1 µm [S]) and Si-bearing: Mg_2Si (Size of top 25% by volume: 9.1 µm[L], 9.8 µm [T], 5.8 µm [S]). The composition of dispersoids was measured to be Al_2CuMg (Size of top 25% by volume:9.1 µm[L], 7.3 µm [T], 6.5 µm [S]). Further details pertaining the microstructure of the source material can be found elsewhere[17].

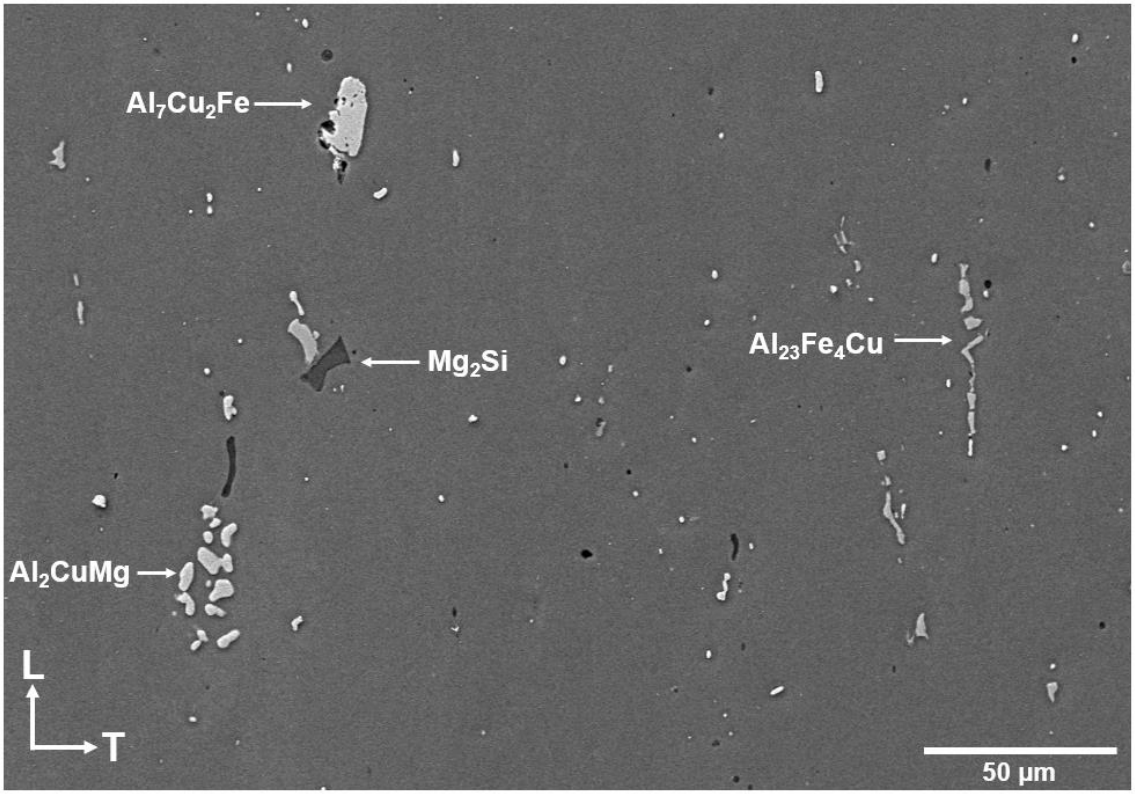

Figure 35: Microstructure of the AA 7075- T651 plate showing metallic inclusions and dispersoids oriented along the rolling axis of the plate.

5.3.2 X-ray Microtomography Scans and Data Processing

The reconstructed datasets were corrected for beam hardening during the reconstruction procedure and filtered for denoising and sharpening features of interest as a part of the post-processing operation using imageJ. Figure 36 shows the post processing workflow that was employed on a virtual vertical cross section of the specimen geometry.

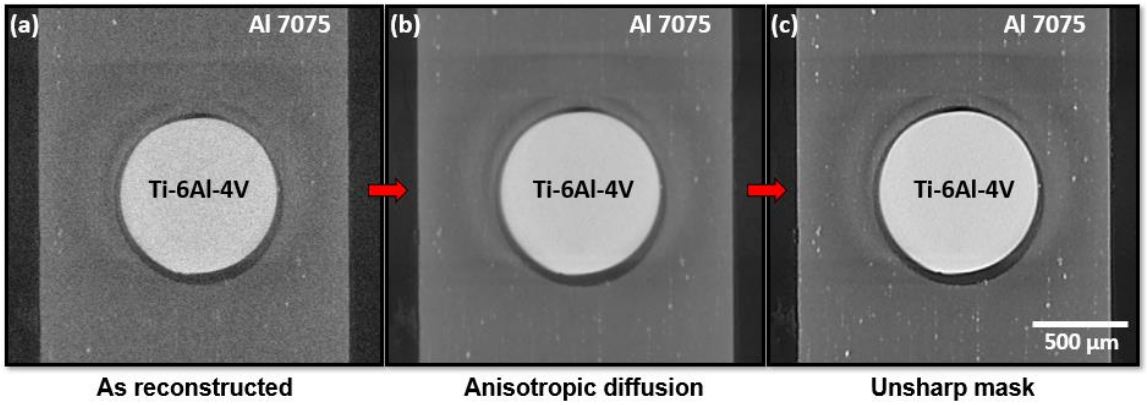

Figure 36. Vertical cross section of the AA 7075-T651 plate and Ti-6Al-4V screw. a) As reconstructed tomography dataset b) Dataset after anisotropic diffusion c) Dataset after anisotropic diffusion + Unsharp mask.

During the segmentation procedure, a pit was segmented and statistically significant only if its size was ≥ 3 voxels or ≥ 5µm along x, y, and z directions. The dataset being analyzed was also compared with the pre-corrosion dataset taken at zero days to ensure that the feature being segmented was a corrosion induced pit and not a reconstruction artefact or a microstructural defect that was already present in the microstructure.

5.3.3 Microstructure Evolution of Pitting Corrosion

Figure 37 shows the evolution of corrosion damage in the AA 7075 alloy plate due to contact with the Ti-6Al-4V screw. For ease of visualization, Figure 4(a) depicts only the segmented Fe-rich inclusions and pits (the outline of the AA 7075 plate and the segmented Ti-6Al-4V screw are not included in this image to better view the pits around the threads) as a function of corrosion time of AA 7075-T651 plate ranging from 5 days to 20 days. After 5 days of corrosion, the segmented profile shows the very beginnings of corrosion on the aluminum alloy plate.

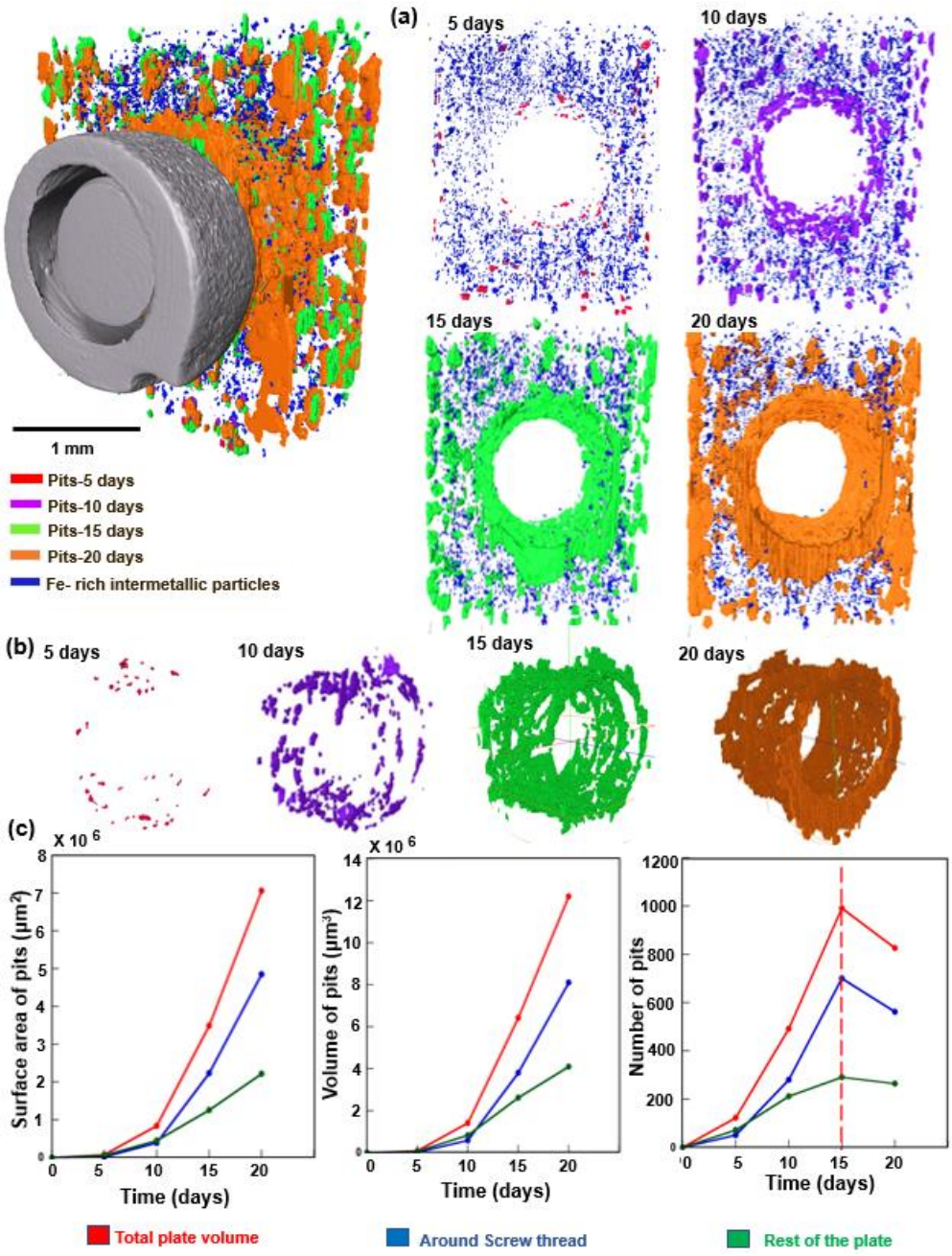

Figure 37: Evolution of the AA 7075 microstructure with increase in corrosion time. (a) Formation of pits on the AA 7075 plate during the corrosion experiment. (b) Pits only around the threading of the plate. (c) Plots of surface area of pits, volume of pits and number of pits as a function of corrosion duration.

The corrosion in the form of pitting is largely restricted to the outer surface of the AA 7075 specimen while the regions around the threading of the fastener show little to no resolvable pitting. Most of these pits initiate at sites containing Fe-rich inclusions. The likelihood that these pits initiate at Mg_2Si particles is low due to the fact that these particles undergo selective dissolution of Mg to leave behind a Si-rich remnant[147]. This remnant has been observed to not contribute to further corrosion propagation in the form of pitting. On the other hand, the Al_2CuMg dispersoid particles undergo dissolution of Al and Mg to leave behind a Cu-rich spongy structure that is reported to behave as a local cathode and lead to dissolution of the matrix in the form of trenching around itself. However, due to continued matrix dissolution, once the remnant particle electrically disconnects from the matrix, it can leave behind a shallow pit (that can be resolved using x-ray tomography) and arrest continued corrosion attack[21,127,174]. However, due to the relatively high x-ray energy used for scanning the specimen, the contrast between these particles (Al_2CuMg and Mg_2Si) and the matrix was poor and hence the precise location of Mg_2Si and Al_2CuMg particles could not be determined.

After 10 days of corrosion, the surface corrosion further increases leading to new pit formation and deeper pits as compared to the 5 days of corrosion. Additionally, pits are observed on the aluminum alloy plate underneath the head of the screw and in contact with the threading of the screw. On further corrosion to 15 days, pitting underneath the head of the screw and on the female threads rapidly increases and can be seen clearly from the segmented profile view images. Lastly, the tomogram from 20 days of corrosion shows a large increase in the size and depth of pits. Tracking pits from 15 days of corrosion and

comparing them to the 20 day corrosion dataset shows a removal of significant volume of the aluminum alloy in close proximity to the fastener.

Figure 37(c) shows plots of surface area of pitting, volume of pitting and number of pits plotted against time of corrosion. The lines in blue on all the plots indicate data from pits segmented in regions around the screw threading and on the plate surface underneath the head of the screw. The green lines in each plot is data from pits segmented in regions of the plate that do not include regions around the threading or under the head of the screw, i.e., regions on the outer surface of the plate. Lastly, the lines in red on all the plots indicate total plate volume, i.e., sum of the data represented in blue and green. The plots representing the surface area and volume of pits for all timesteps show an identical trend. Regions around the threading and underneath the head show a large increase in pit surface area and volume compared to the pits in the rest of the plate which show a linear increase. Interestingly, the number of pits around the threading and underneath the head of the screw show an increase until 15 days, similar to the surface area and volume plots, and then exhibit a decrease. The number of pits in the rest of the plate remains approximately the same for the 15 day and 20 day corrosion timestep.

The decrease in number of pits in the 20 days corrosion data can be attributed to pit coalescence. Mating surfaces are particularly susceptible to localized corrosion due to small volumes of fluid that can penetrate and remain trapped within the specimen geometry. Trapping of corrosive fluid within fastener-plate gaps is often observed in aircraft structures as well [175]. Figure 37(b) shows segmented pits for each time step in the regions only around the fastener threading and underneath the head of the screw. The density and number of pits present in this area is seen to clearly increase with corrosion

time. Localized corrosion also leads to the formation of remnant corrosion products in the gap between the male and female threads. This further reduces contact between mating surfaces, thereby leading to a weaker joint.

5.3.4 Fractographic Analysis of the Fractured Specimen after Fatigue

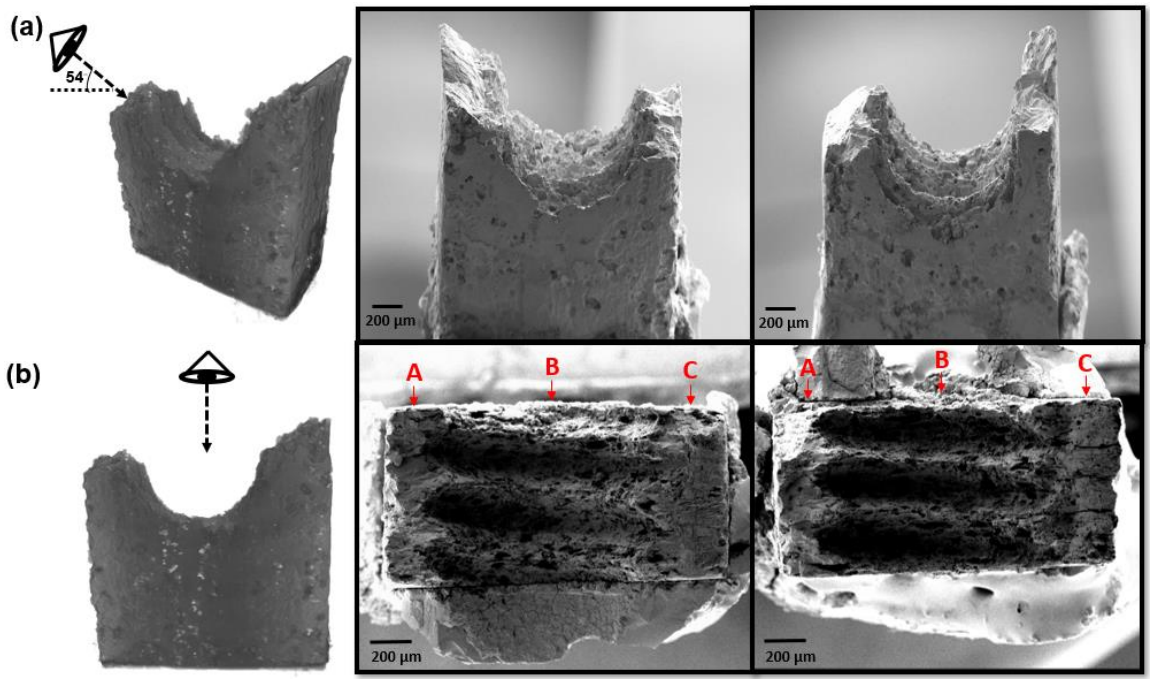

Figure 38: Visualization of fracture surfaces. (a) Angled view of the fracture surface. (b) Top down view of the fracture surface showing three regions A, B and C for each half.

The specimen lasted 1780 cycles before undergoing failure. Figure 38(a) and (b) shows an angled and top down view of the fracture surfaces as indicated by the adjacent schematic. These large field of view fracture surfaces shows three regions associated with each half of the fractured specimen. Two of these regions are symmetrical in terms of dimensions (Regions A and C) and are on either side of the threaded region (Region B). The threaded region (Region C) shows extensive amount of pitting corrosion damage just as the tomography datasets depicted. Under an external mechanical stress, it can also be

seen that the female threads on the plate act as natural stress concentrators owing to their helical structure. Additionally, the fracture surface topography on both regions A and C exhibit an extremely rugged surface.

On closer inspection of region A and region C, of both fracture surfaces, three crack initiation sites could be identified. These sites are in close proximity to the female thread mating surface of the AA 7075-T651 plate and originate from stress concentrating corrosion pits.

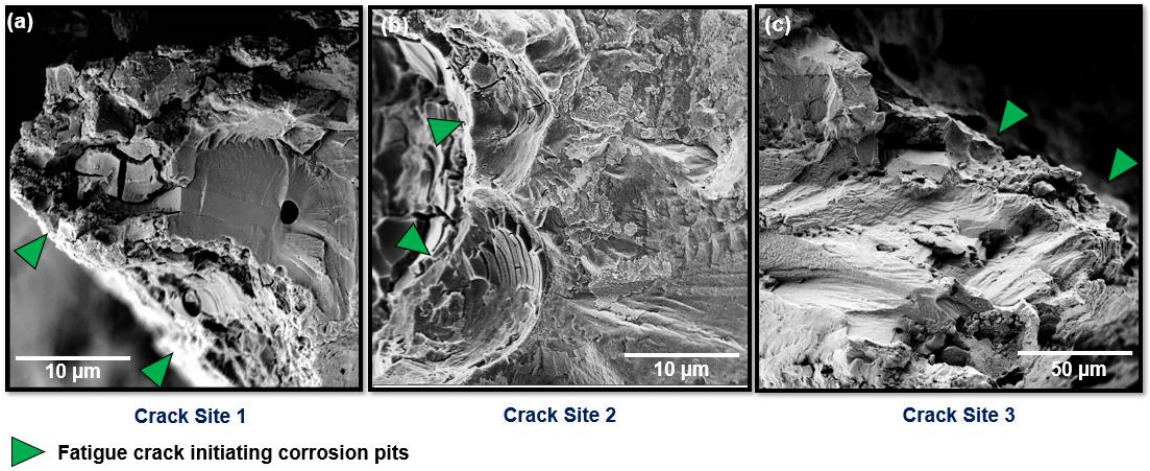

Figure 39. Fatigue crack initiation sites, (a) (b) (c) Crack initiation sites showing the presence of crack initiating pit clusters.

Figures 39 (a), (b) and (c) show the locations of the three crack initiating pits. In all three cases, more than one pit was responsible for crack initiation. Identification of these crack initiating pits was possible due to (a) their shape, which appear in the form of incomplete circles in 2D on the fracture surface, (b) by the presence of corrosion product at the bottom of the pits, and (c) by carefully studying the region ahead of the corrosion pits in the direction of crack growth. Figure 40 shows an example of one such pit that was responsible for initiating a crack at site 2. Figure 7(a) shows the pit and ahead of the pit,

the crack path which is characterized by the presence of river patterns. Figure 7(b) shows a higher magnification image of the same pit. Mud cracking of the corrosion product within the pit is clearly visible.

Figure 41(a) shows a large FOV low magnification image of the location of the crack initiation site (marked with a white box). Also marked is the outline of the female threads on the plate(red).

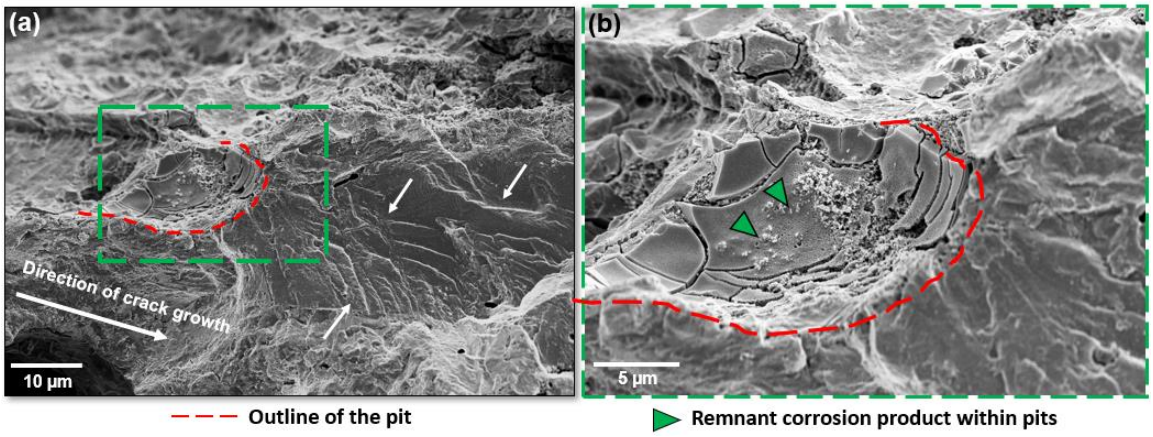

Figure 40: Pit from crack site 2 showing the presence of corrosion product within the pit and signs of crack propagation ahead of it.

Figure 41(b) is a stitched image of the crack from its initiation site until the fast fracture region. At the crack initiation site (Figure 41(c)), two pits adjacent to an Fe-rich metallic inclusion particle and its associated pore were identified to be the starting points for the crack initiation. The inclusion particle was composed of Al, Fe, and Cu according to EDS measurements. A limited number of fatigue striations can be seen near the initiation site.

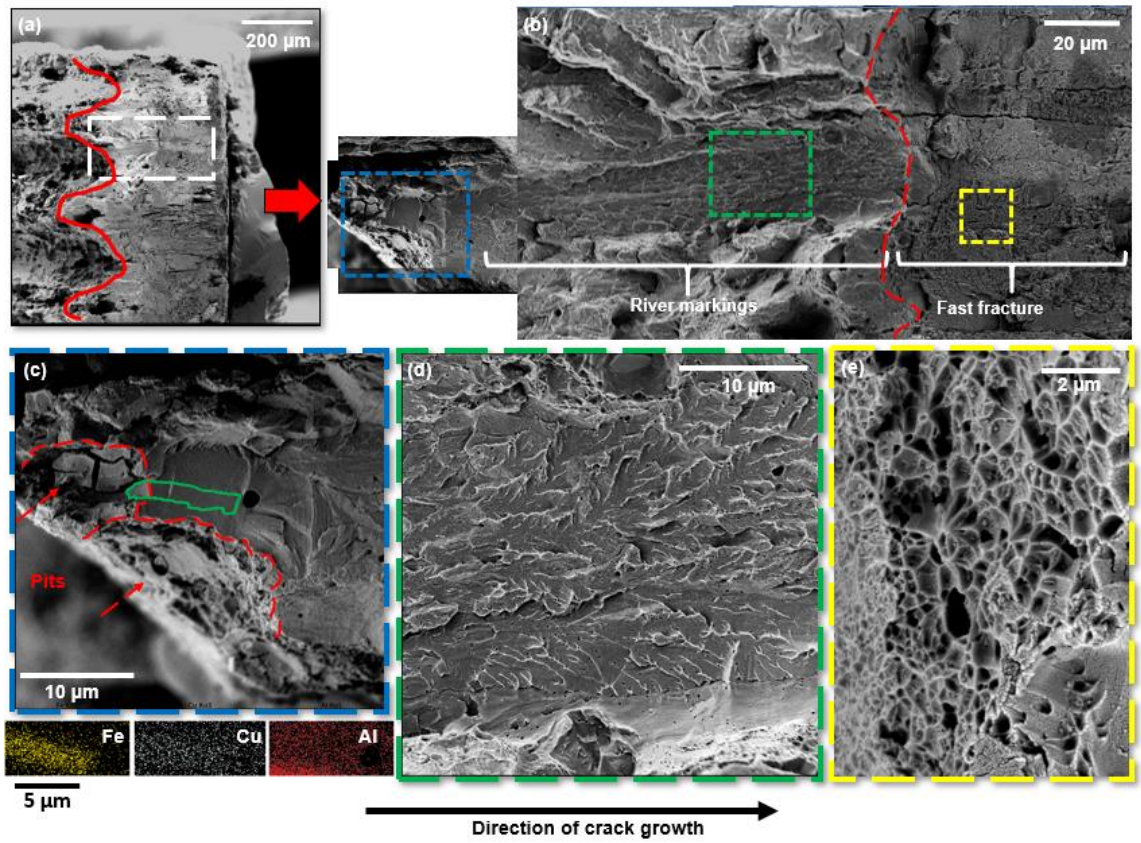

Figure 41: Crack initiation site 1. (a) Large FOV low magnification image of ROI, (b) Stitched image of crack- from initiation to fast fracture, (c) Crack initiation site- 2 pits with an Fe rich metallic inclusion, (d) River patterns ahead of the initiation site, (e) Fast fracture characterized by the presence of dimples. Black arrow at the bottom of the figures specifies direction of crack growth.

Following the striations, river markings can be seen originating and propagating away from the threaded region indicating the direction of crack growth (Figure 41(d)). The river markings lead into the fast fracture region and is characterized by the presence of the presence of dimples (Figure 41(e)). Additionally, many these dimples were formed at precipitate sites indicated by the presence of precipitate remnants at the base of the dimples.

Crack initiation site 2 contains two crack initiating regions in close proximity to one another. Figure 42(a) highlights the location of this crack initiation site (marked with a white box). Figure 42(b) shows the precise locations of the two crack initiating regions shown in red and green boxes. Region 1 contains a cluster of three crack initiating pits as in figures 42(c) and (d). Region 2 contains a single crack initiating pit (Figure 42(f) and (g)). Steady state crack growth ahead of the pits in both regions is characterized by striations ahead of both regions' crack initiating pits and are also indicative of the crack growth direction. The striation spacing immediately ahead of the pits in both regions was 80 ± 5 nm. While the cracks initiate independently from both regions, tracing the crack growth with the help of the striations indicates that the cracks merge, which is why these regions have been clubbed into one crack initiation site. This is followed by the fast fracture region, which is characterized by the presence of dimples, similar to what was observed in site 1. Crack initiation site 3 contains a corrosion pit cluster on the female thread. As in the case with crack initiation site 1, an inclusion particle is observed adjacent to this pit cluster. EDS measurements(Figure 43(c)) indicated the particle to be Si-rich indicating that this particle was an Mg_2Si inclusion prior to being exposed to the corrosive fluid during crack growth[105].

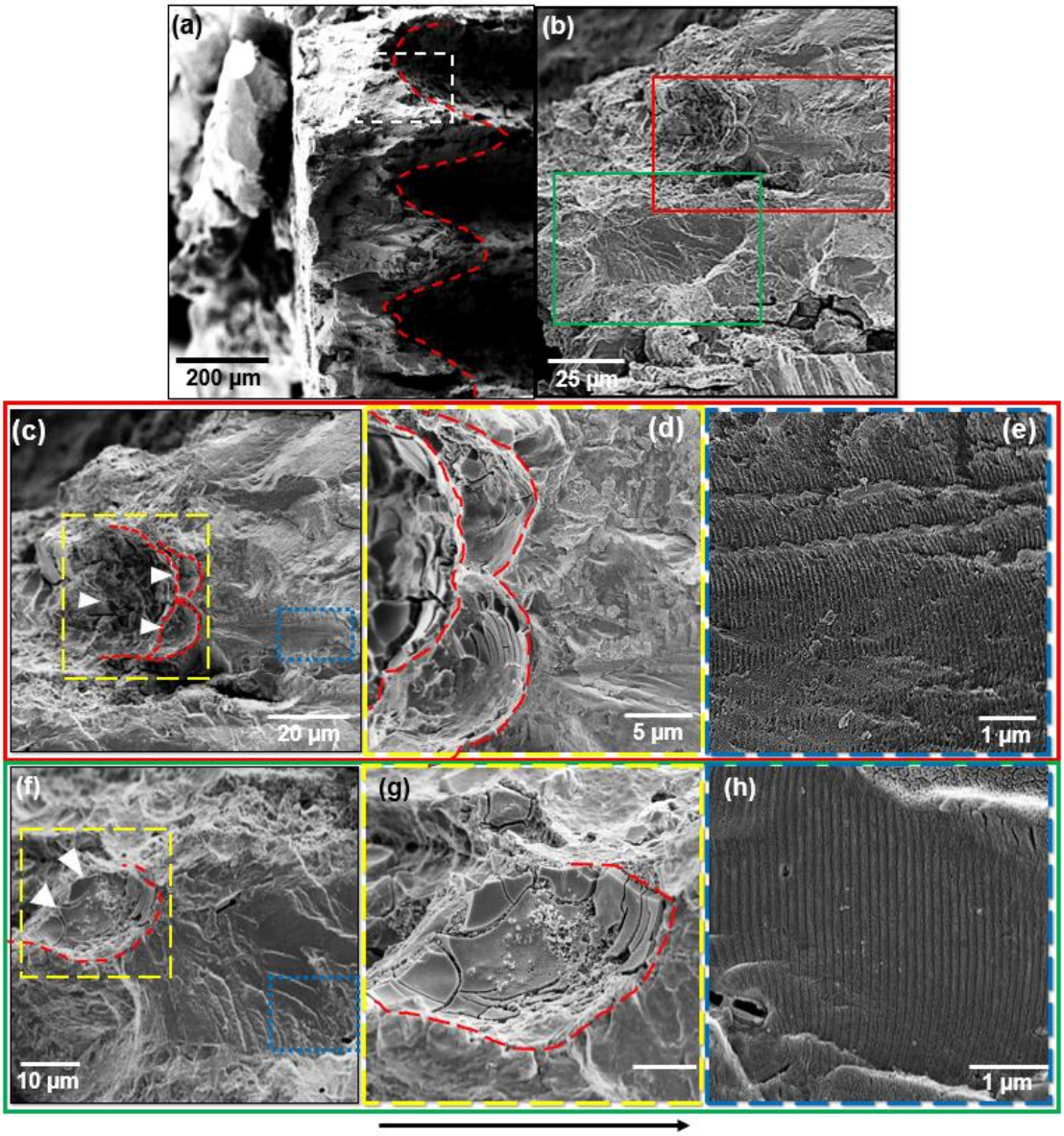

Figure 42. Crack initiation site 2, (a) Large FOV low magnification image of ROI, (b) Crack initiation site highlighting the two regions in red and green boxes, (c)(d)(e) Region 1- Three pit cluster(yellow box) and the striations(blue box) ahead of the pits, (f) (g)(h) Region 2- Single pit (yellow box) and the striations (blue box) ahead of the pit. Black arrow at the bottom of the figures specifies direction of crack growth.

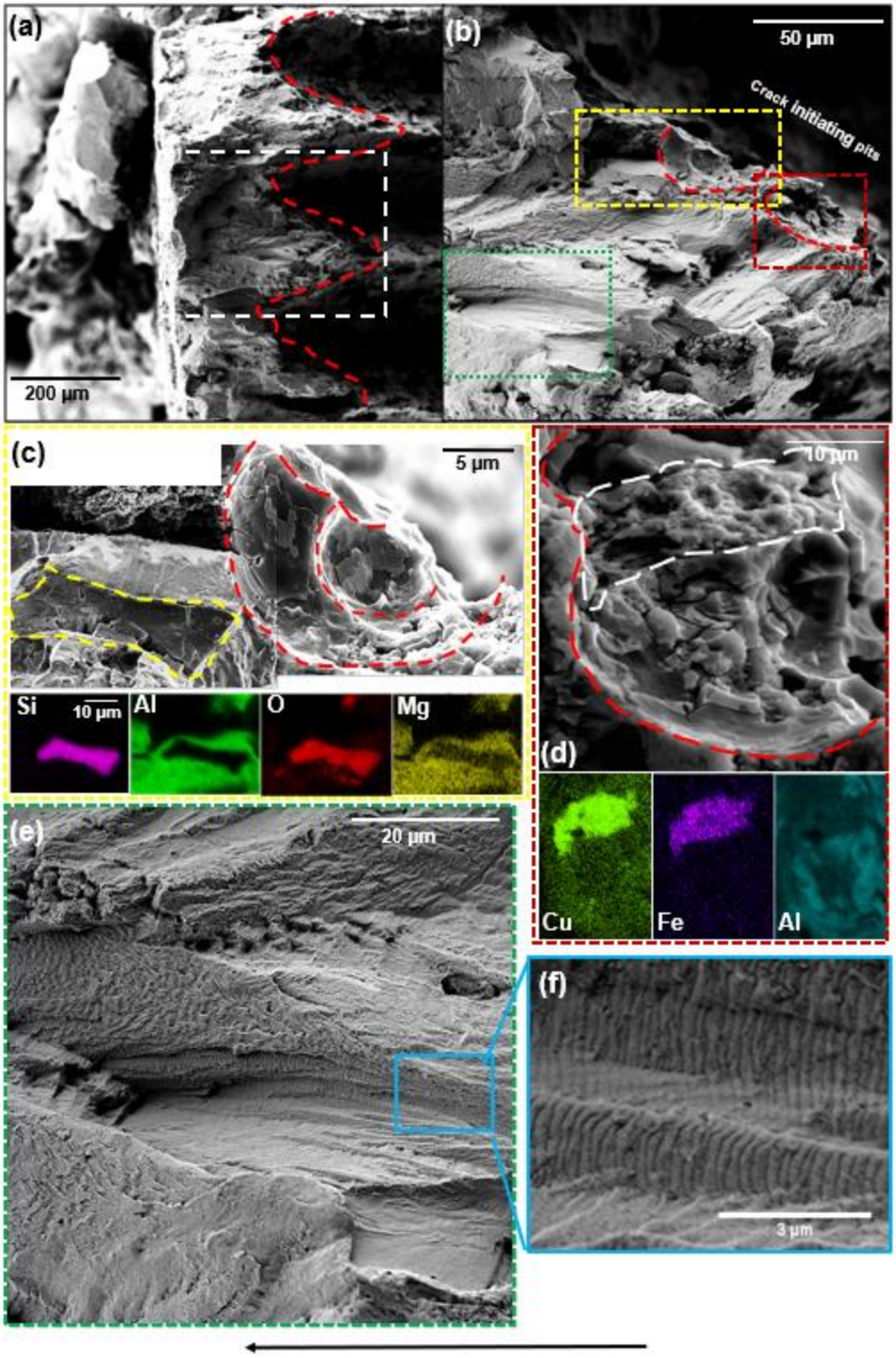

Figure 43: Crack initiation site 3, (a) Large FOV low magnification image of ROI, (b) Higher magnification image of the ROI highlighting crack initiating pits, (c) Stitched image

of a crack initiating pit(yellow box) and the adjacent Si-rich inclusion particle + EDS map, (d) Image of the other crack initiating pit (brown box) showing Cu and Fe-rich inclusion particle remnant + EDS map, (e) Higher magnification image of the green box from (b) showing striations ahead of the crack initiation site. Black arrow at the bottom of the figures specifies direction of crack growth.

Figure 43(d) shows the presence of a remnant Fe-rich inclusion particle at the base of the second pit in the cluster. The crack growth direction is informed by the presence and shape of fatigue striations. The striation spacing immediately ahead of the initiation sites is observed to be 220 ± 5 nm. This is followed by the fast fracture region.

The use of x-ray tomography helps to visualize the evolving corrosion damage in excellent detail in regions that would be inaccessible to the experimenter even after specimen fracture, such as between threads of the plate and immediately sub-surface. From this data, it is clear that corrosion rate drastically increases with more time. The volume of corrosive fluid that can seep into the crevices of the couple underneath the head of the screw and near the tail also increases with corrosion damage and is expected to lead to the large increase corrosion damage between threads. This can further reduce contact of the female threads of the plate with the fastener's male threads. In service, the screw fastener and a nut would ideally hold two plates together. Such exacerbated attack between threads could further disengage the threads leading to the application of undesirable loading conditions on the screw. Furthermore, the damage to the plates themselves in terms of crack initiation and propagation could be very severe. It is thus critical to be able to identify potential locations of crack initiation in the scenario where such loading sequences may be found.

5.3.5 Crack Initiation Sites

The corrosion fatigue behavior of AA 7XXX has been studied extensively in recently published works [28,58,72,96,97,114]. As in previous studies, crack initiation from pits has been exclusively seen to originate from sites containing Fe-rich inclusions[28,58,176]. A zone of relative planarity exists ahead of the pits at the start of the crack which is then followed by severe surface ruggedness in topography indicating the role of hydrogen ingression during the 20day corrosion period (H formation due to pre-corrosion) and/or during the corrosion fatiguing (H release from corrosion of freshly created matrix surfaces during cracking)[73,177]. Furthermore, once the crack starts propagating, striations observed in the specimen shows larger areas of brittle striations as opposed to ductile striations indicating a large environmentally assisted cracking behavior[65,178,179].

A thorough analysis was conducted on the three crack initiation sites to understand the local microstructure that contributed to their initiation and evolution. The location of crack initiation sites observed during the failure analysis of the specimen were correlated with the x-ray tomography data obtained over the 5 timesteps and post fracture. Tomography datasets of each of the failed halves of the specimen were used to bridge the 2D SEM images obtained during failure analysis with the tomography datasets captured over the 20day corrosion period. Furthermore, this was used to trace the crack initiating pits in the 3D volume of the specimen and identify the exact location of pit initiation.

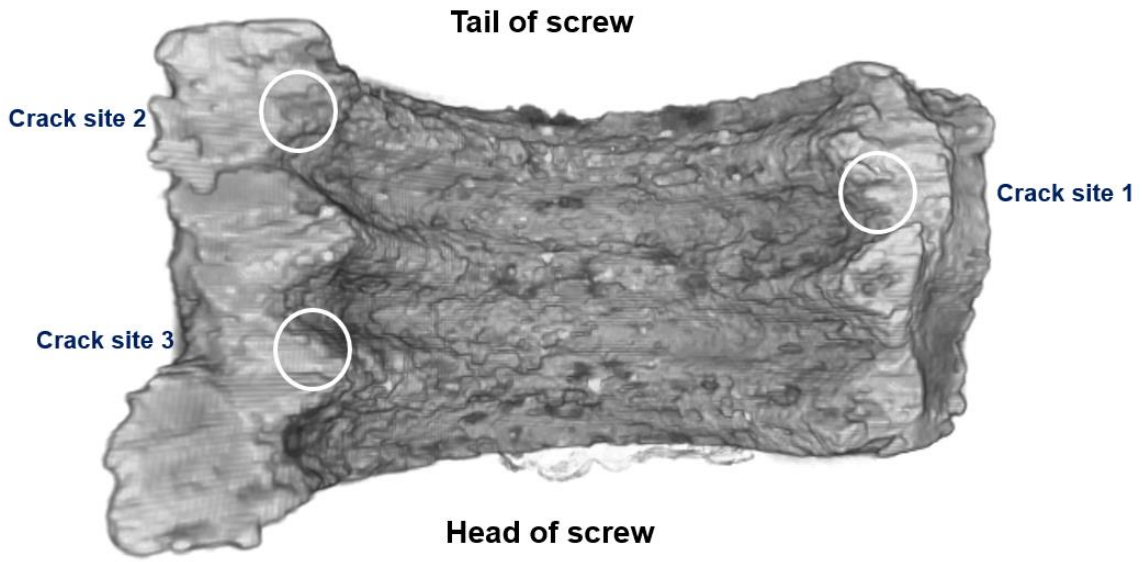

Figure 44:Top down view of one fractured surface highlighting crack initiation site locations.

Figure 44 details the exact location of the three crack initiation sites with the help of a top-down view of the 3D rendering of a fractured half of the specimen. Also included in the schematic is the orientation of the screw as it would have been in the couple during corrosion and fatiguing process. For each crack initiating pit, post-fracture images yield limited information pertaining the crack initiation site before pitting and the conditions that led to crack initiation locally. Hence, it is important to use a combination of fractography and tomography data to physically trace the locations of each site. The trace of the pit from 20 days to 0 days corrosion has been shown in the following figures. Figure 45 show that site 1 had an Fe-rich inclusion at the initiation site.

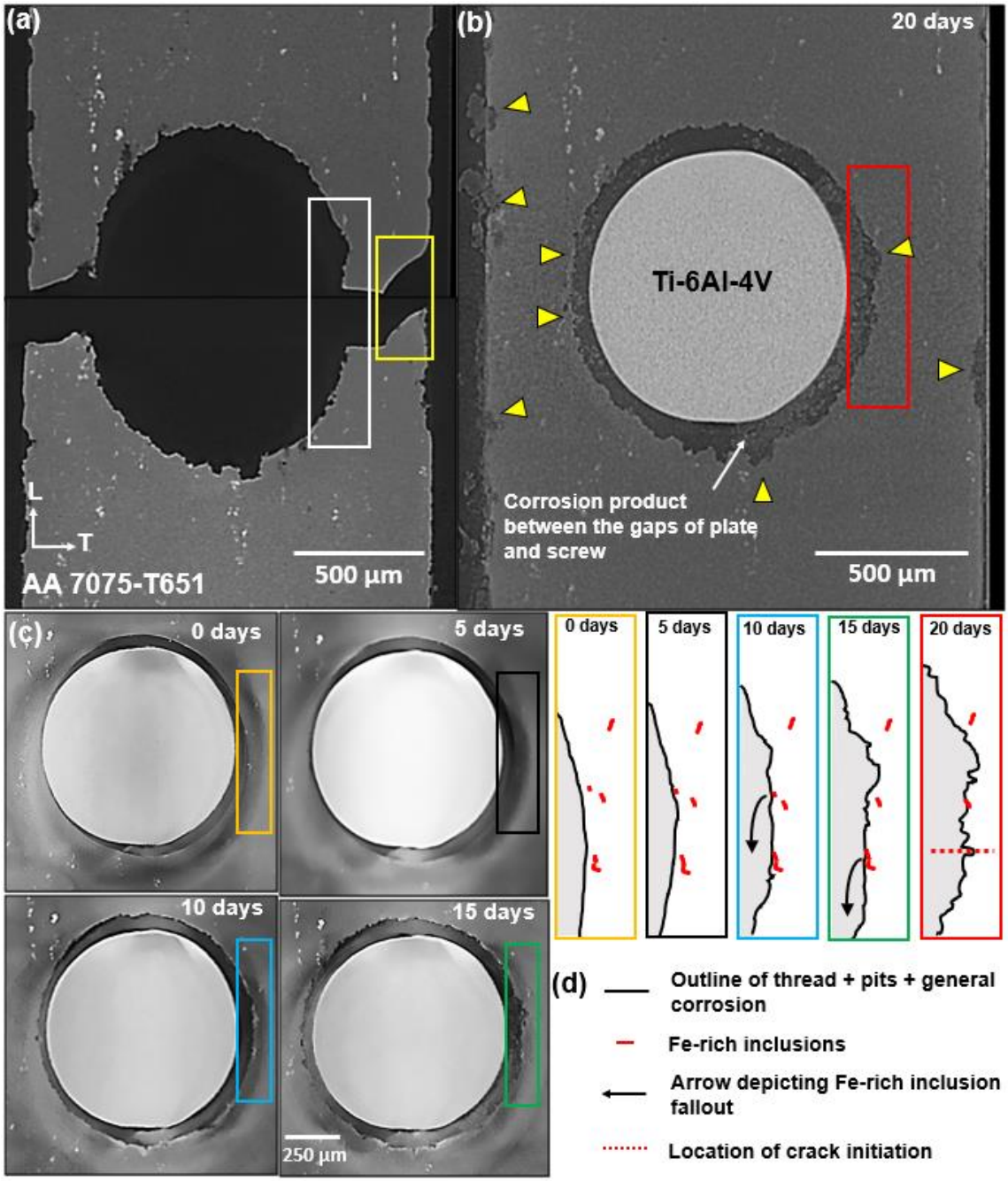

Figure 45: Crack initiation site 1 traceback, (a) Fractured halfs of the specimen highlighting the crack initiation site(white box), (b) The same slice from the dataset captured after 20 days of corrosion highlighting site 1(red box) and pits in the slice with yellow arrows, (c) The same slice with the ROI highlighted in green, blue, black and yellow boxes for the

15days, 10 days, 5 days and 0 days datasets, (d) Schematics showing the ROI from pristine microstructure to 20 days showing the fallout of inclusion particles during the trenching and pitting process.

Figure 45 shows the trace back of site 1 from 20 days of corrosion to zero days, detailing the sequence of events occurring during the corrosion process. Figure 45(a), (b) and (c) show the same virtual slice of the specimen after failure, 2 0days into corrosion and 15, 10, 5 and 0 days of corrosion respectively. The pit appears to have nucleated around the inclusion cluster via trenching and grown deeper, reaching a depth of 26 ± 2 μm after 20 days of corrosion.

Similarly, Figure 46 shows the trace back of the crack initiating pit from site 2. This region is observed to have a relatively high density of pits nearby. However, the pits initiated at the site of a relatively large Fe-rich inclusion particle. With an increase in corrosion time, this particle is also seen to be dislodged from its initial location and removed due to excessive localized corrosion. The pit reached a maximum depth of 50 ± 2 μm after 20 days of corrosion. Images from Figure 43 show that site 3 had a Si-rich inclusion, formerly Mg_2Si in the vicinity of one of the pits of the initiation site. The other pit contained a remnant of an Fe-rich inclusion at its base. Figure 47 shows the trace back of this pit until the beginning of the experiment.

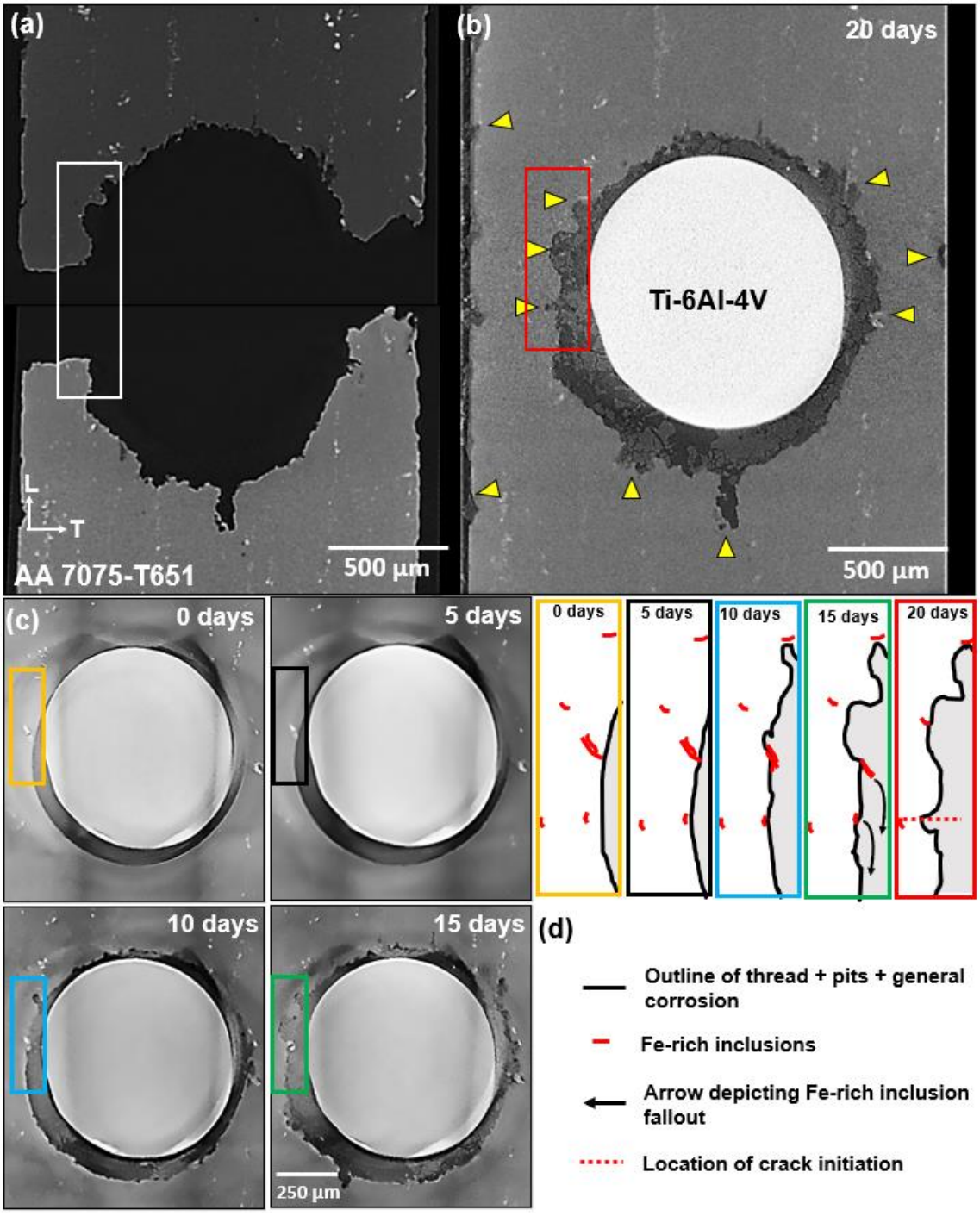

Figure 46: Crack initiation site 2 traceback, (a) Fractured halves of the specimen highlighting the crack initiation site(white box), (b) The same slice from the dataset captured after 20 days of corrosion highlighting site 1(red box) and pits in the slice with

yellow arrows, (c) The same slice with the ROI highlighted in green, blue, black and yellow boxes for the 15days, 10 days, 5 days and 0 days datasets, (d) Schematics showing the ROI from pristine microstructure to 20 days showing the fallout of inclusion particles during the trenching and pitting process.

Like the other two crack initiation sites, this site features the presence of Fe-rich inclusion particle clusters that lead to matrix trenching, dislodge and leave behind clusters of pits that are ideal for crack initiation. Interestingly, pits close to the fracture surface (shown by blue arrows in figure 47(a)), also show the formation of secondary cracking in the vicinity of pits that did not become dominating cracks during the corrosion-fatigue process. This is expected due to the fact that these pits lie close, but not on the plane of maximum stress concentration in this geometry. The dominant crack initiating pit in the cluster grew to a maximum depth of 46 ± 2 μm after 20 days of corrosion.

From figures 45, 46 and 47, it can be concluded that the crack initiation sites are associated with clusters of pits originating at metallic inclusion/inclusion cluster locations. Interestingly, the specific location of crack initiation at each of these sites (shown by dotted red lines) is characterized by deep pits that were formerly occupied by an Fe-rich inclusion particle. It can be seen from the trace back images that the inclusion particles at these sites cause trenching around themselves and dislodge from the surface leaving a deep pit underneath, which then act as crack initiation sites in conjunction with the conducive stress state. Another important observation about initiation sites pertains to the nature of the pits from which the crack initiates.

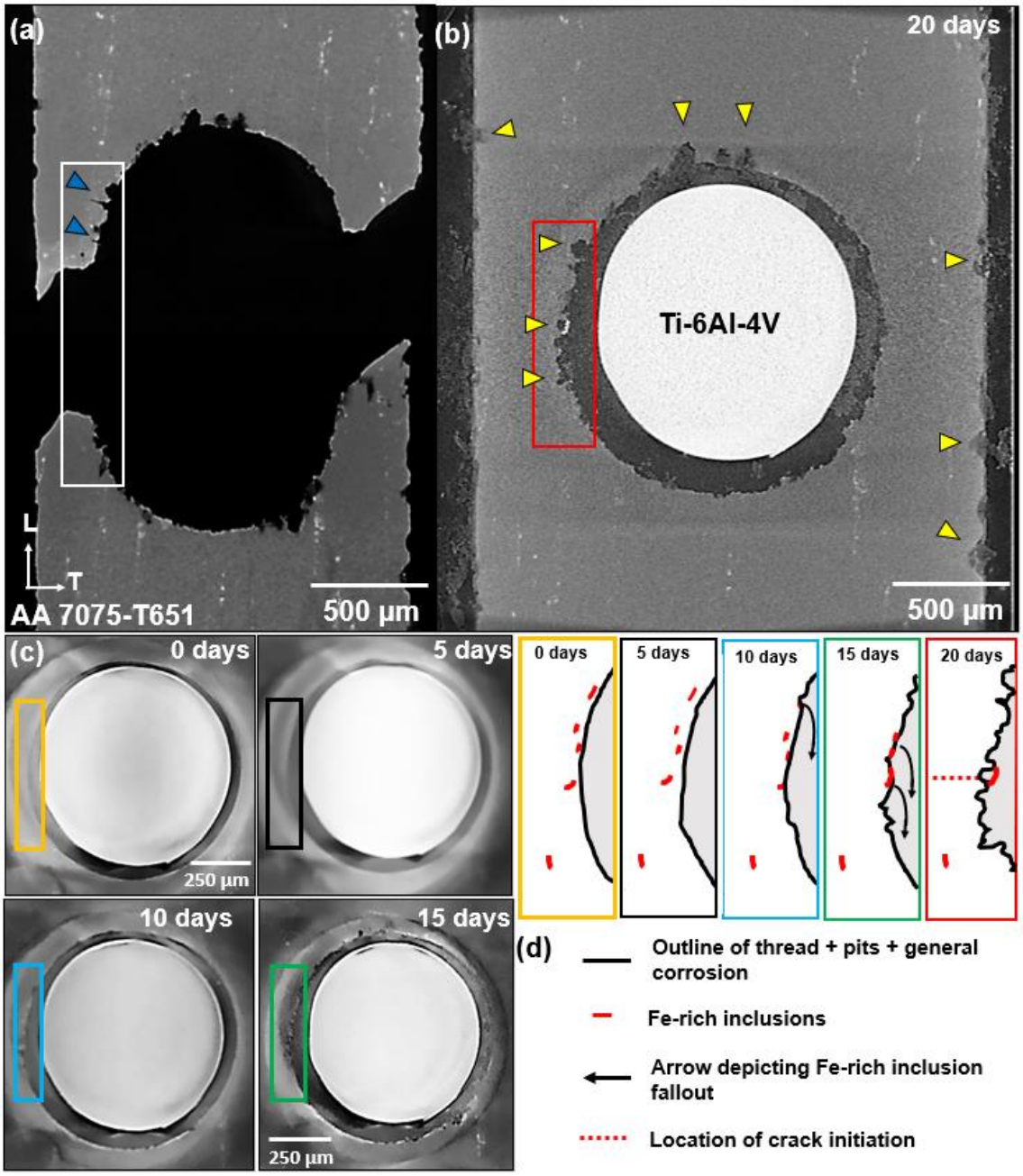

Figure 47: Crack initiation site 3 traceback, (a) Fractured halves of the specimen highlighting the crack initiation site(white box), (b) The same slice from the dataset captured after 20 days of corrosion highlighting site 1(red box) and pits in the slice with yellow arrows, (c) The same slice with the ROI highlighted in green, blue, black and yellow boxes for the 15days, 10 days, 5 days and 0 days datasets, (d) Schematics showing the ROI

from pristine microstructure to 20 days showing the fallout of inclusion particles during the trenching and pitting process.

These pits clusters are observed to not necessarily be the deepest pits in their respective virtual slices. For example, the lower half of the bore hole in figure 46 (a) shows a pit that is significantly deeper than the crack initiating. However, this pit originates on a plane parallel to the ST plane, is elongated along the L direction, and is parallel to the loading axis. Given the loading direction in this geometry this pit has a significantly lower chance of initiating a crack than a pit that nucleates along the T or S direction(perpendicular to loading axis), which is the plane expected to have the highest stress concentration at the center of the threaded hole. A similar observation is from figure 14(a) where a secondary crack did not emerge to be the dominant crack for that site. This implies that the precise location, size (a function of the local and global electrochemical environment) and the local stress state of the pit contribute to determine whether a pit/ pit cluster will act as a crack initiation site.

5.3.6 Sequence of Crack Initiation and Propagation

X-ray tomography combined with SEM characterization of each of these cracks show unique propagation features that help in obtaining further information about the cracking process. With the information presented above, it is possible to estimate the order in which cracks initiated during the corrosion fatigue cracking. Comparing the 3 crack initiation sites that were identified in this specimen, the fast fracture regime for all 3 cracks was characterized by the presence of dimples. Cracks from site 2 and 3 behave similarly, i.e., they have a pit cluster as crack initiation sites. They also demonstrate a clearly defined Paris regime indicated by the presence of fatigue striations. In both cases, the fatigue

striation spacing is seen to increase with increase in crack growth. However, the crack from site 3 is measured to have started off in its respective Paris regime with a larger striation spacing compared to crack from site 2. Secondly, the total number of striations observed in site 3's crack path is less than the striations observed in crack from site 2's path. Lastly, the rate of growth of striation spacing with increase in crack propagation is higher with crack 3. This indicates that the crack from site 3 initiated later during the corrosion fatigue process than the crack from site 2. Following a later initiation, the crack at site 3 propagated faster due to a higher local stress concentration, than at the crack from site 2.

On the other hand, the crack from site 1 shows the presence of a pit cluster as an initiation site, followed by a negligible Paris regime, a well-defined area containing river markings and a large fast fracture region. The fast fracture surface can also be seen in the post-fracture tomography data as oriented at ~45 degrees to the loading axis as can be seen in the yellow box in figure 45(a). A large river marking region indicates brittle cleavage fracture with a rapid crack growth rate unlike a cycle by cycle growth of cracks from site 2 and 3. This indicates that the sequence of initiation of cracks from their respective sites is crack 2, followed by crack 3, followed by crack 1. Lo et al [180] reported the formation of multiple cracks initiating at corrosion sites around a central hole in plate specimens.

While multiple crack initiation sites at corrosion pits were observed in the specimen in this study, the lack of tomograms *during* the corrosion fatigue experiment limits precise time-based observations of crack initiation at the base of pits, influence of a crack on the initiation and growth rate of the next crack and finally, crack coalescence. The variation in initiation and propagation rates of cracks within such geometries can further complicate crack growth modeling. On that note, 4D observations of crack initiation and propagation

during the fatigue / corrosion fatigue experiment are critical to improving the understanding of damage in fastener-plate geometries.

Multiple crack initiation sites at corrosion pits were documented in this study. *In situ* tomography scans conducted *during* the corrosion fatigue experiment would have enabled the precise time-based observations of crack initiation at the base of pits, influence of a crack on the initiation and growth rate of the next crack and finally, crack coalescence. However, despite this, a correlative microscopy-based approach enabled the successful identification of the local microstructural evolution in the vicinity of the three crack initiation sites, which otherwise would have been impossible with just fractography. Additionally, a crack growth sequence could also be hypothesized. 4D observations of crack initiation and propagation during the fatigue / corrosion fatigue experiment would push the boundary in improving the understanding of damage in fastener-plate geometries.

5.4 Summary

A dissimilar alloy couple comprising of an AA 7075-T651 plate and a Ti-6Al-4V screw was subjected to alternate immersion corrosion testing over a period of 20 days. X-ray microtomography was used to observe and analyze evolution of corrosion damage. Next, the specimen was corrosion fatigued until failure and failure analysis was performed on the specimen's fracture surfaces.

- In the beginning, Corrosion pitting initiated primarily at the outer surface of the specimen. Over time, the magnitude of corrosion damage increased substantially in the interior of the couple, i.e., contact regions underneath the head of the screw and around the

threads. After 15 days of corrosion, the number of pits started to decrease due to pit coalescence.

- Corrosion fatigue testing led to the formation of 3 crack initiating sites. Additionally, correlative microscopy comprising data from failure analysis and pre- and post-corrosion fatigue tomography scans were used to identify the precise location of these crack initiation sites in the original tomography datasets. In each case, Fe-rich inclusion clusters led to the formation of pits/ pit clusters that initiated cracks under cyclic loading and led to specimen failure. Additionally, using the crack propagation features ahead of the initiation sites, a crack initiation sequence was hypothesized.

CHAPTER 6

IN SITU CHARACTERIZATION OF CORROSION FATIGUE IN A NAVAL STRUCTURAL JOINT IN SALTWATER ENVIRONMENT

6.1 Introduction

Fastener couples and galvanic interfaces have been reported to be very favorable sites for crack initiation in service structures, accounting for up to 75- 90 % of structural failures[8,181]. These are also locations where dissimilar metal contact exists, leading to galvanic coupling and crevice corrosion and hence, very detrimental to the corrosion behavior of aluminum alloys in their vicinity. Stainless steel and Titanium alloys (Ti-6Al-4V) are widely used fastener materials that are often coupled with aluminum alloy plates in fastener-plate geometries. These two alloys have nobler potential values compared to aluminum alloys and behave as cathodes in a neutral saltwater solution.

Recently, several studies have attempted to study cracking from rivet holes. Gupta et. al studied crack initiation and growth from a rivet hole under dry and moist air fatigue[20,69]. They noted that stage 1 crystallographic cracking, generally observed in fatigue are absent and that the cracks start at inclusion cluster sites and propagate in a transgranular manner. Additionally, it was also observed that there was no correlation between initiation site and local grain structure. Second phase particles were seen to be the primary crack initiation sites in close proximity to the hole surface. Lo et. al performed corrosion fatigue on plates with rivet holes and observed the formation of multiple cracks initiating and coalescing during growth[182]. Burns et. al studied corrosion fatigue cracking in similar geometries. Using marker band technique, crack position with time

could be reasonably accurately mapped in the specimens and growth rate with distance trends calculated[183]. Pit topography and minute surface features were seen to play a strong role in determining the exact locations of crack initiation from pits. Additionally, flat features were observed immediately ahead of the crack tip indicating the role of hydrogen ingression and interaction with cyclically induced dislocation structures and thereby, assisting brittle crack growth behavior. Other works have also electrochemically created a pit at the bore hole surface and through thickness to study crack initiation[14,184]. Interestingly, the size and aspect ratio of the pit had nothing to do with the mechanism of fracture observed in these samples. However, the stress needed to initiate a crack in the through thickness pit at the bore hole was lower than that with the surface pit at the bore hole. Fawaz et. al have published several insightful works in this area and through extensive finite element modeling and AFGROW simulations and derived a methodology to obtain crack growth rate curves in these geometries[15,185,186].

From the literature, it is seen that a challenge involved in studying these plate geometries is the need to carefully initiate a pit at the bore hole to study corrosion fatigue from these pits. While this is a good method to study individual pit to crack behavior in such geometries and study relevant mechanisms, it falls short in adequately representing the local microstructure experienced by the plate near the bore hole in the presence of a cathodic fastener. Multiple pits can initiate at the bore hole – fastener contact surfaces and it can get significantly exacerbated with time and application of stress. In short, there is a need to perform a realistic corrosion initiation experiment in the couple and perform corrosion fatigue to study the relevant microstructural mechanisms taking place. Opportunity lies in the fact that *in situ* corrosion fatigue of a dissimilar metal couple of

industrial relevance has never been performed in 4D. Recently, the use of tomography was demonstrated using synchrotron tomography to study corrosion[119,170]. Observing corrosion initiation and progression is a difficult challenge in such couples as the cathodic fasteners are often significantly denser than the aluminum plate and this can result in imaging artefacts that can be challenging to eliminate. Ti alloy fasteners are however easier to work with in this scenario as they have a density that is not significantly greater than that of aluminum (Ti-6Al-4V density = 4.43 g/ cm^3). Due to this, they do not attenuate x-rays as much as a steel fastener would and hence require lower x-ray beam energy for the scan compared to what would be needed if a steel cathode was in the field of view. This also ensures that microstructural features such as inclusions in the aluminum alloy, which are in the field of view do not get "Washed out" in an attempt to obtain adequate x-ray intensity and transmission from the sample. Critical mechanisms such as the location of pit initiation are important to understand at a high resolution before the cracking begins. *In situ* tomography can help in tracking the location of crack initiation and further, studying enough specimens, can also help predict the same. Moreover, the challenges encountered in chapter 5 pertaining identifying crack initiation sites can be alleviated by actually observing crack growth and tracking it with time in 4D. The information obtained here can further be corroborated with detailed fractography.

In Chapter 5, the dissimilar alloy couple was exposed to the fluid on both the front side of the specimen (containing the head of the screw and the front face of the plate) as well as the back side of the specimen (containing the tail of the screw and the back face of the plate). This also increased the susceptibility to crevice corrosion. Thus, in this study, two types of specimens were prepared and compared with each other. Type A specimens

contained an AA 7075-T651 plate with a rivet hole coupled to a rivet that was exposed to the corrosive fluid on all sides including the front and back. Type B specimens contained the same couple geometry but was exposed to the fluid only on the front side of the couple. The back surface of the couple was covered completely with rubber cement. This inevitably minimized the susceptibility to crevice corrosion that was possible in the specimen and additionally, led to an increase in cathode/anode area ratio. Following this, *in situ* corrosion fatigue was performed on both specimen types. Crack initiation sites and propagation behavior was investigated. For both types of alloys. On failure, the specimens were subjected to fractography to study the fracture surfaces in higher resolution. The crack initiation sites were studies in significantly more detail and different regions of interest have been elaborated upon.

6.2 Materials and Experimental procedure

The dissimilar metal couple specimens were comprised of two components namely an AA 7075-T651 anode and Ti-6Al-4V cathode. Plate of AA 7075-T651 were electro-discharge machined from the center of the thickness of a commercially available 25.4 mm thick block of AA 7075-T651(Alcoa, New York, NY, USA) as in figure 48(a). The longest dimension of the plate specimen was oriented along the rolling (L) direction. A 0.85 mm hole was drilled into the center of the width of the plate specimen to accommodate a rivet. The plate was mechanically polished with 600 and 1200-P4000 grit SiC polishing papers.

The plate was further fine polished down to a 1 µm diamond finish. The specimen was thoroughly cleaned with isopropyl alcohol and sonicated to obtain contaminant free surfaces.

A commercially available Ti-6Al-4V plate was used to fabricate rivets with dimensions as in figure 48(b). Tables 4 and 5 show the composition of the as-received AA7075-T651 and Ti-6Al-4V specimen as reported by the supplier and as measured *via* EDS for comparison.

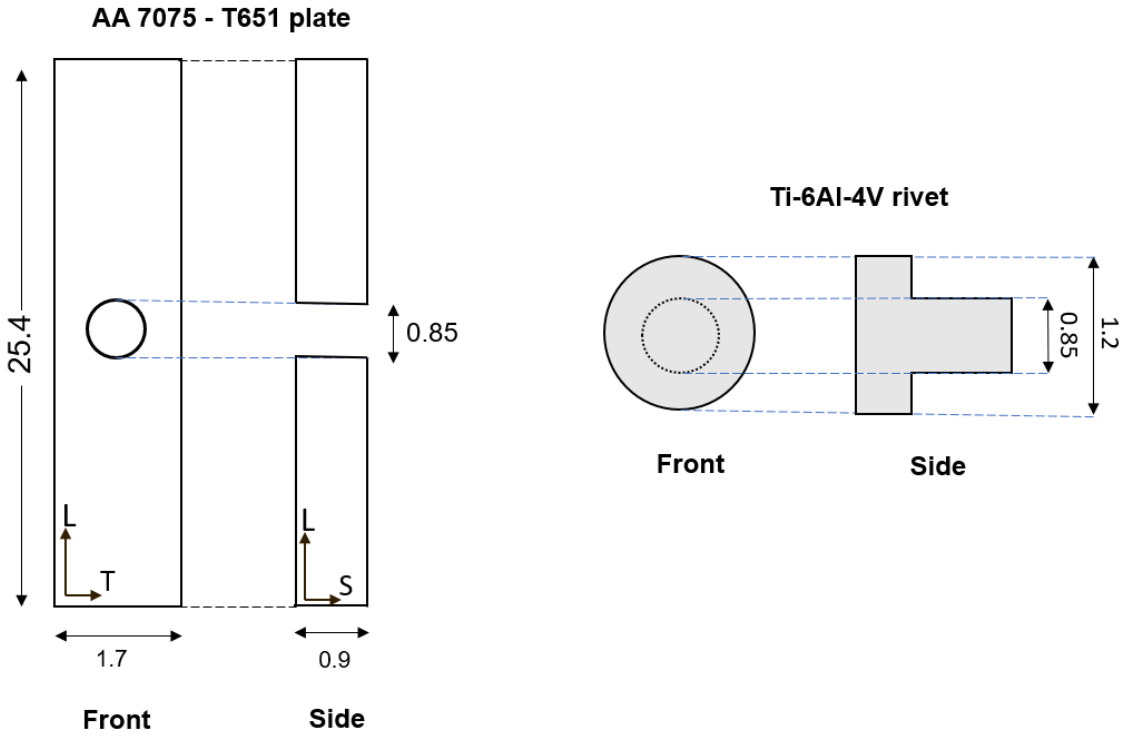

Figure 48. Schematic showing the geometries of the (a) AA 7075-T651 plate and (b) Ti-6Al-4V rivet (All dimensions in mm)

Table 4: Elemental Tolerances (ASTM B209-14) and Measured Chemical Composition of the AA 7075-T651 Block

AA 7075- T651: Chemical composition(wt.%)									
	Si (max)	**Fe (max)**	**Cu (range)**	**Mn (max)**	**Mg (range)**	**Cr (range)**	**Zn (range)**	**Ti (max)**	**Al**
ASTM B209-14	**0.4**	**0.5**	**1.2–2.0**	**0.3**	**2.1-2.9**	**0.18-0.28**	**5.1-6.1**	**0.2**	**Bal**
Measured	**0.2 ± 0.03**	**0.2 ± 0.04**	**1.5 ± 0.07**	**0**	**2.3 ± 0.03**	**0.2 ± 0.03**	**5.9 ± 0.11**	**0**	**Bal**

Table 5: Elemental Tolerances (ASTM B265-15) and Measured Chemical Composition of the Ti-6Al-4V Rivet.

Ti-6Al-4V: Chemical composition(wt.%)								
	Al (range)	**V (range)**	**Fe (max)**	**C (max)**	**O (max)**	**N (max)**	**Others (max)**	**Ti**
ASTM B265-15 (wt.%)	**5.5 - 6.75**	**3.5 - 4.5**	**0.4**	**0.08**	**0.2**	**0.05**	**0.4**	**Bal**
Measured	**6.0 ± 0.12**	**4.1 ± 0.09**	**0.15 ± 0.03**	**0 ± 0.04**	**0**	**0**	**0.2**	**Bal**

On obtaining a scratch free surface on the AA 7075-T651 plate with a rivet hole, the Ti-6Al-4V rivet was fit into the rivet hole of the plate and a tight fit was ensured. The rivet was positioned such that the head of the rivet was in contact with the AA 7075-T651 plate and the tail of the rivet was not protruding out of the surface of the plate. Two types of specimens were prepared for comparison. Rubber cement was used to cover portions of the specimens in order to obtain specific cathode/anode area ratios. Type A specimens were exposed on all surfaces of the specimen to the corrosive fluid. On the other hand, rubber cement was used to cover the sides and the back surface of the couple specimens in Type B specimens. This prevented fluid from seeping into the small cervices that could be created between the rivet hole and the rivet during the corrosion fatigue cycling of the specimen. Due to this, the cathode/anode area ratio could also be accurately controlled leading to an area ratio of 0.5 in Type A specimens and an area ratio of 1.2 in Type B specimens. The region encompassing the rivet and the plate surface not covered by rubber cement encompassed the regions of interest in both specimens.

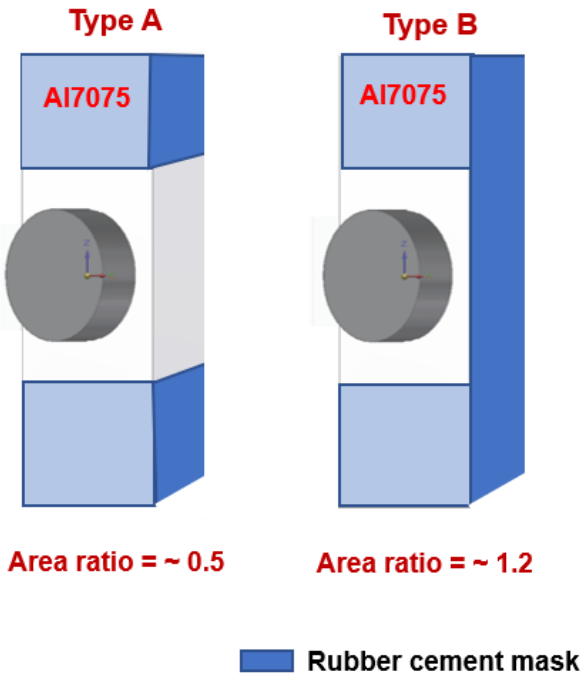

Figure 49: Schematics showing the two types of specimens designed for this experiment. Type A was exposed on all surfaces to the corrosive fluid while type B was exposed only on the face containing the head of the rivet.

Both Type A and Type B specimens were immersed in neutral 3.5 wt.% NaCl solution for pre-corrosion for a period of 10 days in order to let pitting corrosion to initiate. Care was taken to ensure that the level of the fluid was constant through the addition of DI water upon evaporation. The specimens were positioned such that the region of interest was dipped in the solution throughout the 10day period. After 10 days, any region of the plate that was not part of the region of interest (near the portion that would be gripped) that was corroded was carefully cleaned and polished to prevent specimen failure due to stress concentration during the subsequent corrosion fatigue experiment. Specimens were fitted with a bath composed of a PEEK base on which a Kapton cylinder was epoxy glued to

contain the fluid. They were then carefully placed inside the fixture for corrosion fatigue testing. Following this, corrosion fatigue was performed on the specimens using a specially designed loading fixture (figure 50(b)).

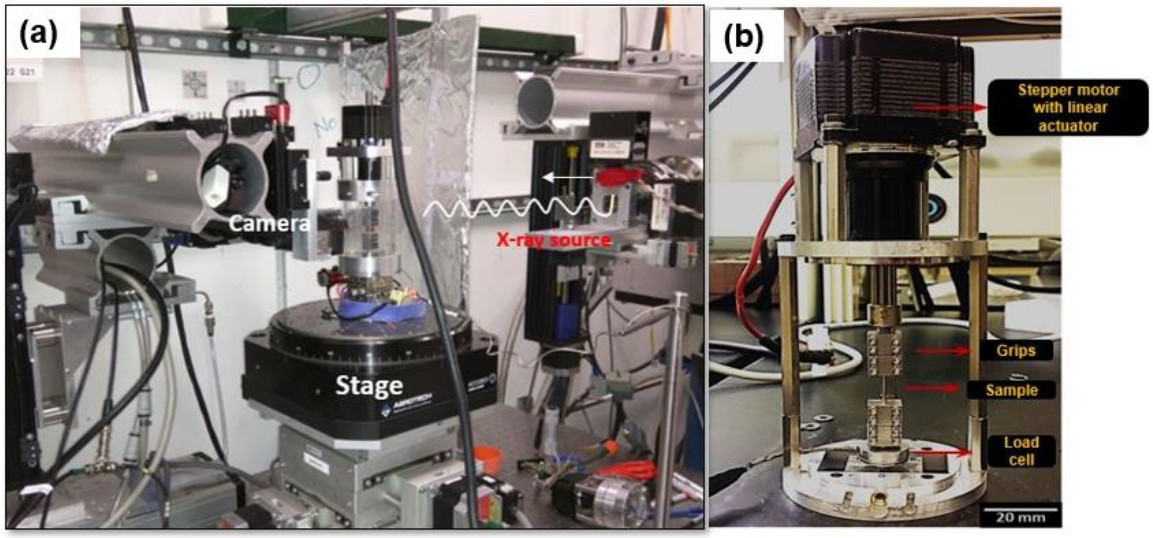

Figure 50: (a) Beamline setup at 2-BM, APS, Argonne National Laboratory, (b) Loading fixture that was used to conduct the in situ corrosion fatigue experiments.

In situ corrosion fatigue of the specimens was conducted at the 2-BM beamline at the Advanced Photon Source at Argonne National Laboratory. Corrosion-fatigue was conducted at an R-ratio of 0.1 with a s_{max} of 200 MPa being well within the elastic limit for LT AA 7075-T651(475 MPa along the L direction). A loading frequency of 1 Hz and a sinusoidal waveform were used. The specimen was corrosion-fatigued to failure. The fracture surface of the specimen was thoroughly cleaned with 3% HNO_3 to clear out any remnant oxide that could inhibit the fracture surface from being imaged using the SEM.

With regard to the x-ray tomography scans at the beamline, 1501 projections were captured at an exposure time of 0.01 seconds/projection over 0 – 180 degrees angular rotation (6 degrees/second) using a pink beam (average energy ~30keV). This ensured that

each tomography scan lasted a total of 30 seconds excluding time for data transfer. A 20 µm LuAG scintillator was used. A pixel size of 0.875 um was achieved. The temporal resolution of the scan was fast enough to capture bubble formation and enable the capturing of multiple scans once the crack had started propagating. The datasets were reconstructed using Tomopy, a python-based module used to reconstruct and post process tomography data . A filtered back projection algorithm was used to reconstruct the data. Since the experiment was conducted *in situ*, data alignment was not a challenge as they were misaligned by ≤ 3 pixels in any dimension. Following this, due to the large file size per dataset, they were appropriately cropped to ease the handling of multiple datasets simultaneously. ImageJ was used to perform the cropping operations and the preliminary filtering operations that involved the use of median and anisotropic diffusion filters. Next, Avizo 9 (Bethesda, MD) was used to further filter the datasets to improve contrast and reduce noise using the non-local means and unsharp mask filters. Furthermore, Avizo 9 was used to segment the Ti-6Al-4V screw and cracks in each dataset to observe crack initiation and evolution in 4D.

Once the specimens fractured, each half of the specimen with or without the fastener were collected, rinsed with DI water and carefully preserved for further analysis at Arizona State University. The specimens were carefully washed with 3% HNO_3 solution to be able to remove the obscuring corrosion product on the fracture surface. Fractography was performed using a dual-beam Zeiss® Auriga focused ion beam (FIB) workstation. The crack initiation site was identified using the x-ray tomography data and correlated with the observations in the SEM.

Following this, different portions of the specimen's fracture surface were mapped carefully to delineate the initiation site, the Paris regime and the fast crack propagation region.

6.3 Results and Discussion

6.3.1 Tomography Observations in Type A Specimens

Type A specimens were exposed to the corrosive fluid on all the surfaces in the region of interest. Figure 51 shows the progress of a crack that initiated from a Type A specimen that was segmented. Only one side of the Ti-6Al-4V rivet is visible, and the matrix is transparent. The crack for each timestep was segmented and is shown with a different color for each timestep. Additionally, included in the figure are number of cycles per timestep that was segmented. The crack in this case started from near the tail of the rivet in the specimen where a pit was formed at the location of an Fe-rich inclusion. The crack initiated from only one side of the specimen geometry and was observed to grow over the course of the corrosion fatigue cycling until fracture at 27,637 cycles.

A second crack initiated towards the very end of the life of the specimen and an image of the 2D slice of the LT plane that contains the secondary crack can be seen on the opposite side to the primary crack. Apart from the two cracks, several other interesting microstructural damage phenomena are visible. Excessive intergranular corrosion is seen to initiate from the rivet hole propagating along the L direction on the ST plane of the specimen. Secondly, hydrogen bubble formation is rampant within the cracks as well as the miniature gap between the rivet and the plate.

The gap between the bore hole and the rivet body is noted to be < 10 μm as measured in the tomography scans at the start of the experiment. Once the dominant crack

fractures one side of the sample, this gap between the plate hole and the rivet body increases substantially and enables the hydrogen bubbles that have formed inside the crack and between them to escape.

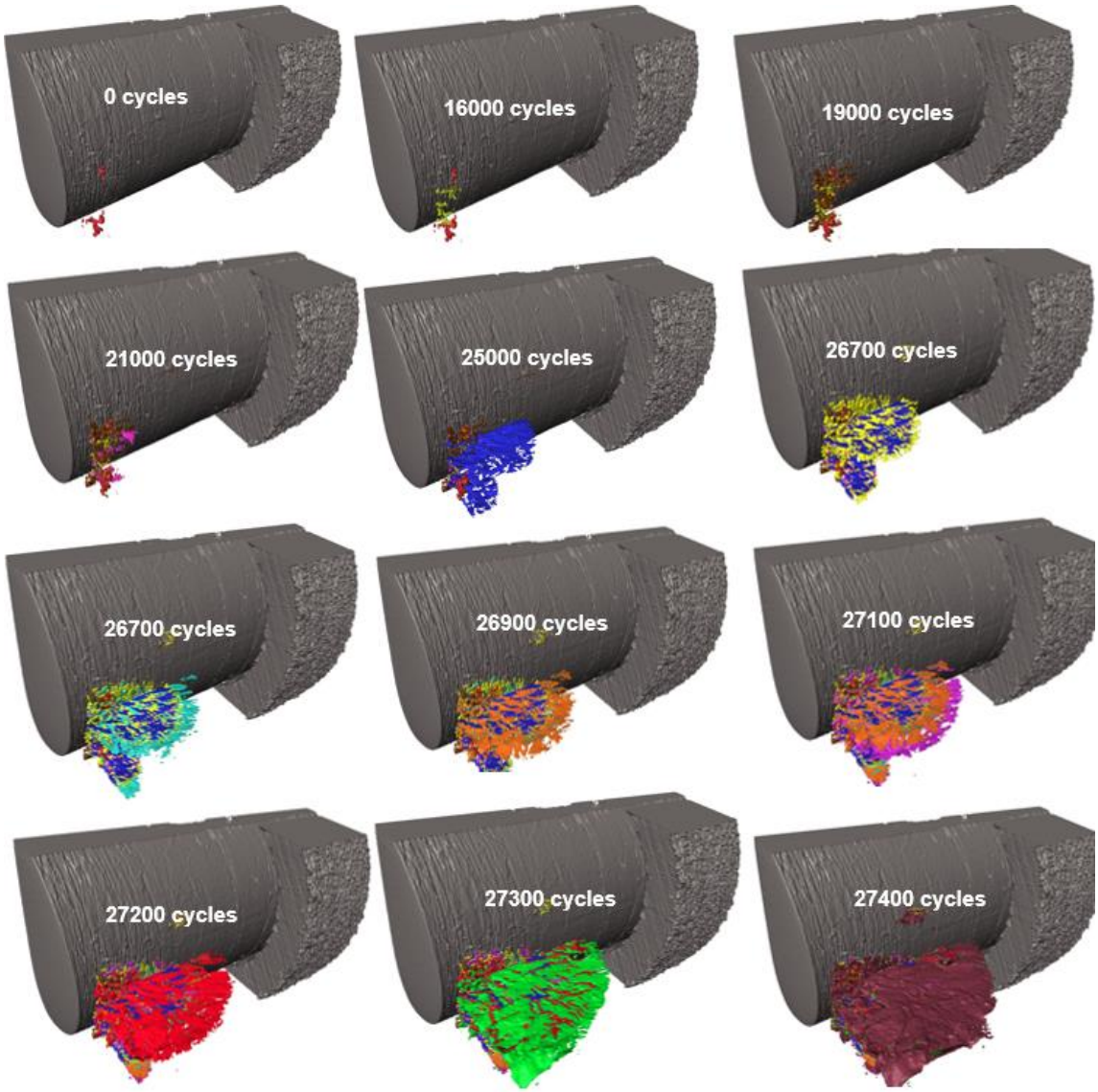

Figure 51: Example of segmented crack growth in a Type A specimen. The crack is observed to start near the tail of the rivet in the aluminum plate and grow as a quarter elliptical corner crack.

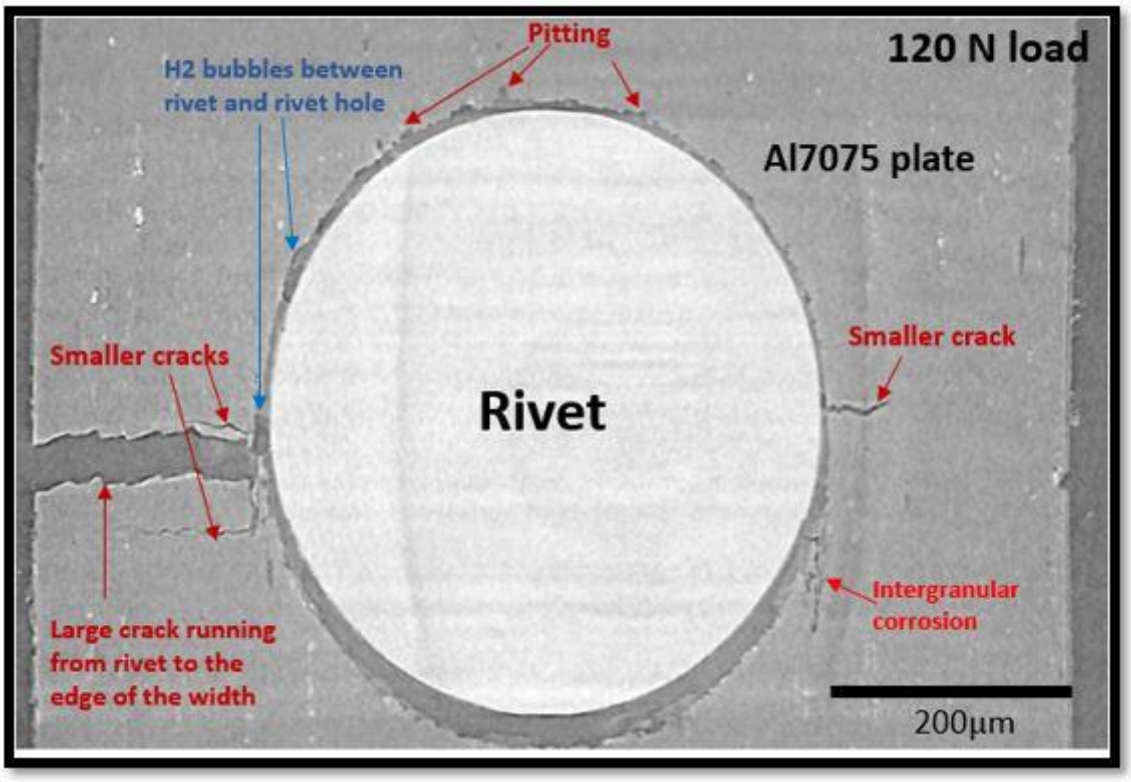

Figure 52: 2D slice of the LT plane showing the dominant crack from figure 51. Also seen are a host of other damage mechanisms acting simultaneously, such as secondary cracks, pitting with a preference along the L direction and intergranular corrosion.

6.3.2 Tomography Observations in Type B Specimens

The type B specimens were exposed to the corrosive fluid only on the front face of the couple containing the head. All other surfaces including the back containing the tail of the rivet were sealed off with rubber cement to prevent the corrosive fluid from seeping in. While during the 10 day period, no corrosion attack in the form of pitting was observed in between the rivet body and the bore hole. The corrosion damage in this specimen was restricted to the front surface of the plate right underneath the head of the rivet. Due to a combined galvanic and crevice action, deep fissures were observed on the surface which

resembled cigar shaped cracks on the ST plane. However, it was seen that during the corrosion fatigue operation, fluid could penetrate in between the gap and assist corrosion locally. This is also evidenced by the presence of hydrogen bubbles presence inside the bore hole. On fatiguing the specimen in the corrosive fluid, cracks started at the tip of pits close to the plate on both sides of the rivet and propagated outwards in both the S and T direction.

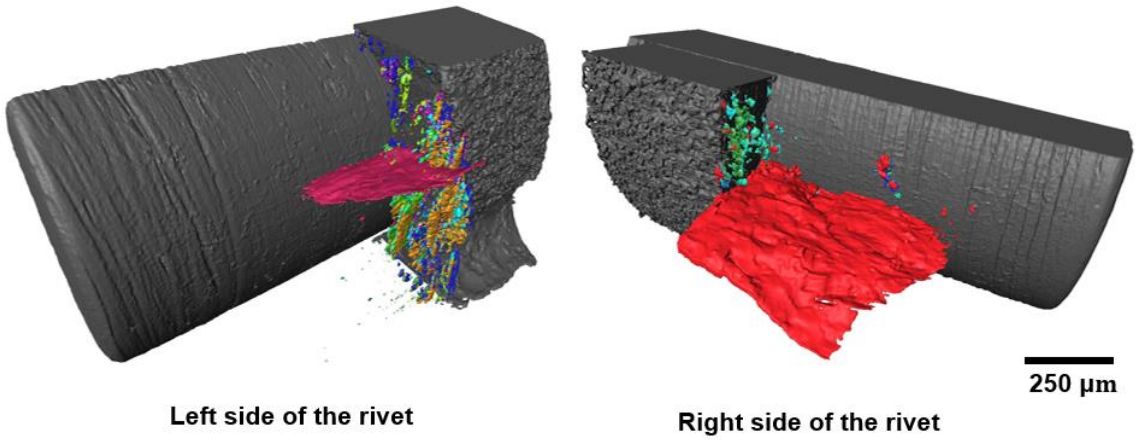

Figure 53: Type B specimen (a) Dominant crack 44 cycles before specimen failure on the left side of the rivet, (b) dominant crack 44 cycles before specimen failure on the right side of the rivet.

Figure 53 (a) shows the initiation and progression of cracking damage on the left side of the rivet head and figure 53(b) shows the same for the crack that initiated at the right side of the rivet. Interestingly, while the crack on the right side of the rivet (looking at the rivet face front) initiated at the plane of maximum stress concentration, the crack on the left started at a pit a little above this plane. This specimen was cycled for 19044 cycles. By the time 19000 cycles were completed, the crack on the right side dominated and fractured the specimen the right side of the specimen as in figure 53 (b). After 44 more

cycles, the crack on the left underwent fast fracture due to very high stress concentration and the specimen failed completely. Figure 54 shows the crack growth of both cracks seen from the top down view of the specimen. This serves as a good way to visually compare crack growth rates of the cracks on each side of the specimen.

6.3.3 Fractographic Analysis of the Fracture Specimens after Fatigue

The fractured specimens were thoroughly cleaned with 3% HNO_3 and sonicated in DI water to remove the corrosion product on the surface. Figure 55 shows the fractographic analysis from the specimen from Type B. Both specimens show similar and very interesting fracture surfaces often seen in corrosion fatigue of AA 7075-T651. Figure 55 (a) and (b) are large field of view images showing the entire fracture surface containing three surfaces A, B and C wherein A and C are similar as they both observed simultaneous crack initiation and propagation in this specimen. Figure 55(c) shows an image of surface A which contains signs of corrosion damage attack. Figure 55(d) shows the initiation site of the crack at a high magnification. The pits closest to the rivet hole and exactly in the middle of the height of the specimen are seen to be most active in terms of crack initiation due to the fact that they are present on the plane of highest stress concentration. Thus, even though deeper pits exist on the front face of the plate, the pits closest to the bore hole are seen to be the most active in terms of crack initiation. A pit is observed to be present on the bottom right corner of the image. It is interesting to note that the shape of the pit is not semicircular in 2D as one may expect. This pit interestingly contains a jut in that is known to be responsible for increasing localized stress concentration. Jut ins and micropits within bigger pits have been previously observed to follow local grain structure or grain boundaries to grow ahead of the existing pit and lead to crack initiation.

Fatigue river markings are seen to emanate from these pits near the initiation site indicating the direction of crack growth. Additionally, striations (~0.8 μm) are observed ahead of the initiation site indicating the Paris regime of steady state crack growth (figure 55(e)). Finally, the fast crack growth regime is characterized by the presence of excessive dimpling and a very rugged surface morphology (figure 55(f)). Also included is surface B (figure 55(g)) which was in contact with the rivet body during the entirety of the experiment. Clear signs of intergranular corrosion are seen with pits present at different locations of the surface.

6.4 Summary

The experiment from chapter 5 was improved upon by designing an *in situ* corrosion fatigue experiment in order to be able to study the initiation and propagation of corrosion fatigue cracking in 4D. Type A specimens were exposed to the fluid on all sides and type B were exposed on the side containing the rivet head face. The *in situ* experiments were conducted at the 2-BM beamline at Argonne National Laboratory. Tomography datasets obtained show that pits close to the bore hole of the plate and near the head of the rivet are responsible for crack initiation. Following this, the cracks appear to start grow in the shape of quarter elliptical corner cracks increasing in size along the crack length as well as along the width. Fractography corroborated the information obtained from tomography by yielding insights into the Paris regime and fast fracture regime.

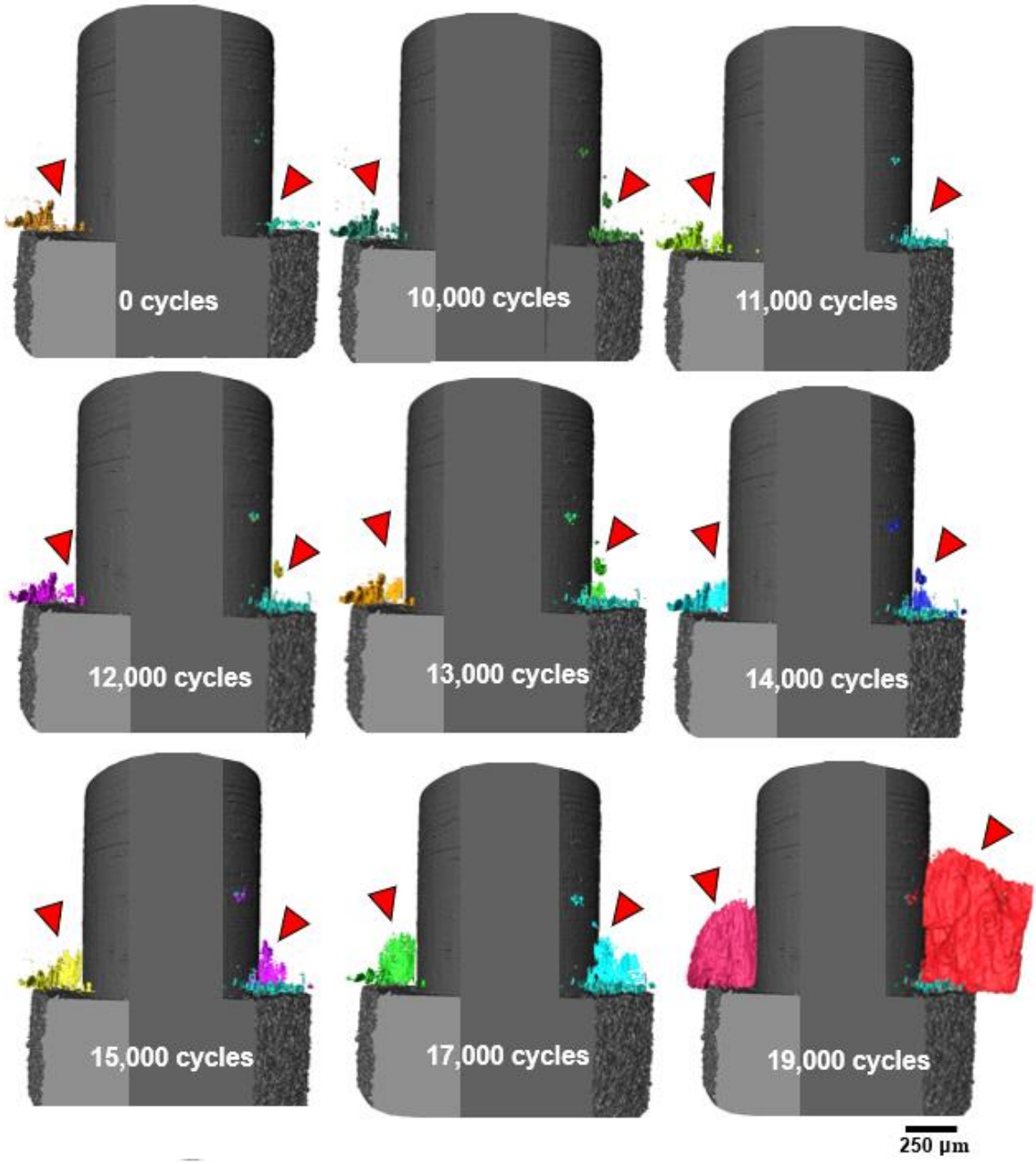

Figure 54: Segmented top view of the Type B specimen from figure 53 showing crack initiation and growth with increase in corrosion fatigue cycling. Red arrows point to the cracks in the AA 7075-T651 plate (invisible) on both sides of the rivet.

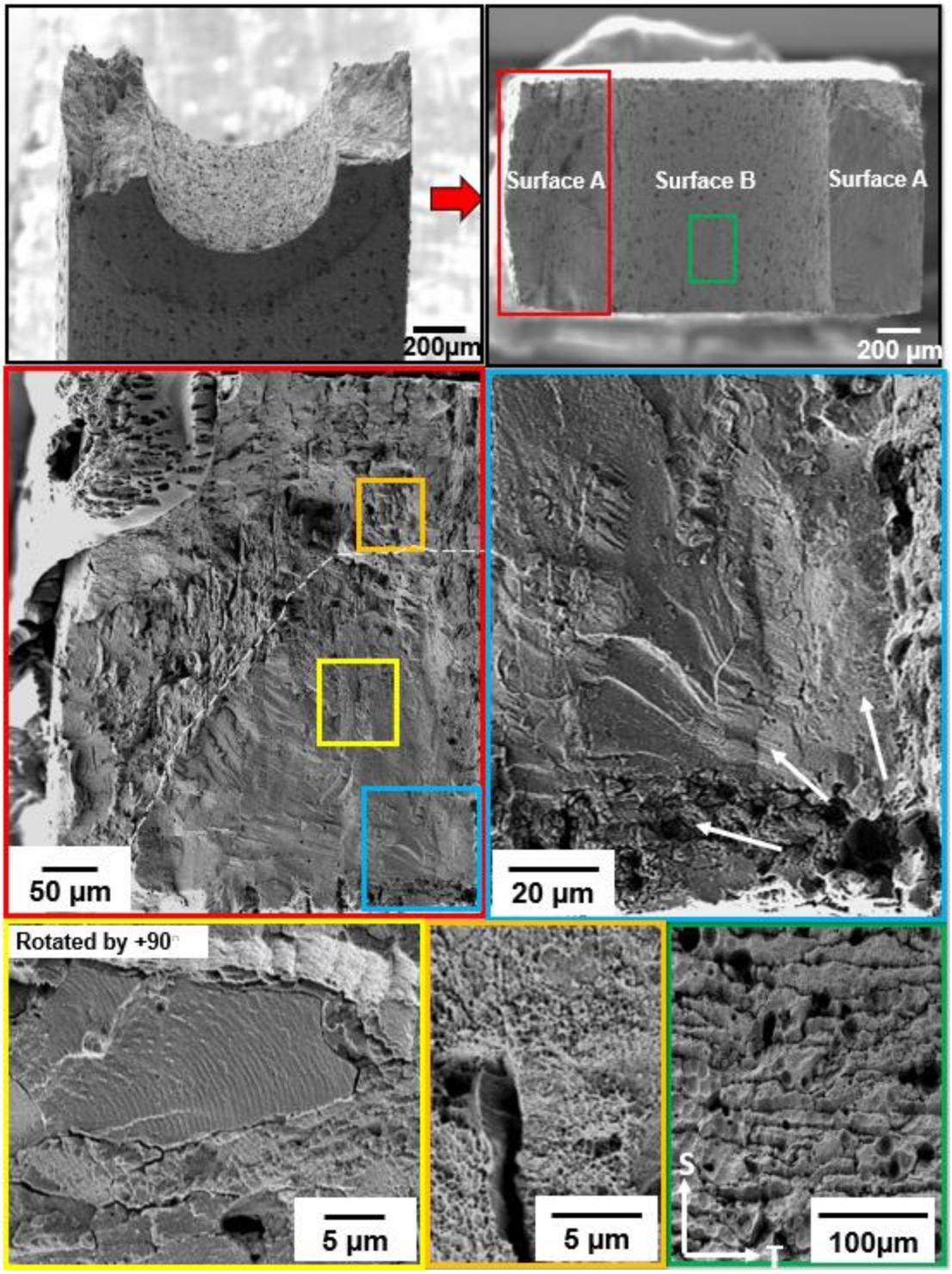

Figure 55: Fractography performed on one fracture surface of the type B specimen whose segmentation is shown in figures 53 and 54. (a) and (b) show an angled (54 degrees) and

top view of the fracture surface which was delineated into surfaces A, B and C. Surface A showed signs of typical corrosion fatigue in the specimen with the initiation of pits seen close to the bore hole surface (figure55(d)). (e) the Paris regime characterized by the presence of striations. (f) Fast fracture regime characterized by the presence of dimples. And (g), surface B characterized by excessive intergranular corrosion and pitting.

CHAPTER 7

CONCLUSIONS

7.1 Summary of Research Findings and Recommendations

- The corrosion behavior of AA 7075-T651 was investigated globally and locally over multiple length scales using correlative microscopy. Investigating Potentiodynamic polarization scans yielded valuable insights into the global corrosion behavior of the alloy with increase in applied external potential. The corrosion behavior starts from region 1 with dissolution of Mg starting at Mg_2Si particles and Al_2CuMg dispersoids. Furthermore, pitting corrosion starts after the second breakdown potential and extends into deep sub-surface damage in the form of Exfoliation Like Action (ELA). It was observed that the precipitates within the grains were responsible for the propagation of the ELA and hence, a mechanism for the initiation and propagation of the same was proposed. Concentric corrosion patterns were observed in the regions 2 and 3. It was observed that these patterns do not resemble any microstructural features such as local precipitate distribution. A mechanism for their formation was hypothesized based on the available literature data on the magnetohydrodynamic phenomenon.
- Fe-rich inclusions played a critical role in all the studies included here. While they do not dissolve at open circuit potential, for the very first time, their dissolution has been documented here and it was observed at 30 mV beyond the second breakdown potential of the potentiodynamic polarization plot. The particle also shows directional dissolution attack indicative of a role of the particle's crystallography.

- To further study the role of localized corrosion due to second phase particles, micropillars of peak aged and highly overaged AA 7075 were fabricated and subjected to alternate immersion corrosion tests using *ex situ* Transmission X-ray Microscopy (TXM). The role of Fe-rich particles and precipitates could be visualized and quantified accurately with image segmentation methods. Additionally, the role of precipitates in aiding intergranular corrosion was compared between the two specimens. Precipitates in the highly overaged specimen are significantly more cathodic to the matrix compared to the precipitates in the peak aged condition. Fe-rich inclusions play an important role in the peak aged condition and almost no role in the highly overaged condition due to the precipitates being the dominant cathodes and aiding faster intergranular corrosion. A clear preference for high angle grain boundary corrosion was observed after sectioning a pillar with the FIB.
- With knowledge of the corrosion behavior of bare AA 7075, a series of experiments were performed on dissimilar alloy couples of AA7075-T651 / Ti-6Al-4V. Plates of AA7075-T651 with M1 threaded hole were fastened with Ti-6Al-4V screws and the couple geometry was subjected to a 20 day alternate immersion experiment to study the initiation and growth of pitting corrosion damage. Pit coalescence was observed after 15 days of immersion corrosion. Corrosion fatigue was performed and on failure, the use of extensive fractography and trace back analysis showed that the initiation sites were composed of Fe-rich inclusion clusters.
- Finally, AA7075-T651 plates with a bore hole were fastened with Ti-6Al-4V rivets. Two specimen types A and B with different cathode/anode area ratios were prepared. These couples were pre-corroded for a duration of 10 days and corrosion fatigued until failure.

Correlative *in situ* tomography and SEM showed that cracks were initiated from pits close to the bore hole in all cases. Jut ins present on the pit surfaces are indicative of local increases in stress concentration within the pit. The cracks are observed to have the shape of quarter elliptical corner cracks. Locations of pits depended on sample type and while the type A specimen cracked from near the tail, the type B specimen nucleated two cracks from pits underneath the head of the rivet that both grew to failure. This study demonstrates for the very first time, the observation of crack initiation and propagation in 4D in fastener-plate couples.

Studying dissimilar metal joints in aircraft and naval structure is a complex multidisciplinary challenge. The incorporation of corrosion and corrosion related damage effects (SCC and Corrosion fatigue) into structural design is still an ongoing challenge. Systematic studies that can adequately simulate in-service corrosion scenarios are critical to establishing protocols that can be incorporated into structural design. The studies presented above are important steps towards realizing this goal. Chapters 3 and 4 specifically examined the corrosion behavior of AA 7075. The use of multi-scale and multimodal techniques correlatively have yielded novel information pertaining the wide range of corrosion mechanisms that can act simultaneously to aid in structural degradation. Furthermore, two simplified fastener plate geometries (Plate + Screw and Plate + Rivet in Chapters 5 and 6 respectively) were investigated without the use of coatings to simulate the worst case scenario of corrosion damage possible in a fixed time frame. Bore holes and dissimilar metal couples are regions where a majority of corrosion and cracking damage is seen to initiate during service. These studies are novel due to the fact that 4D non-destructive corrosion over long periods of time combined with corrosion fatigue has never

been performed in such geometries. Moving forward, these geometries can be further built on, say with more fasteners and with the use of coatings and studied to investigate the role of multiple fastener- plate couples in the vicinity of each other. Additionally, the use of non-destructive *in situ* x-ray computed tomography and correlative microscopy-based workflows can significantly accelerate the pace of research as well as insights that can be obtained from such complex geometries. In short, these studies introduce the possibility and methodology for performing corrosion and cracking studies of such complex geometries in realistic corrosion and cracking conditions. The investigations carried out in this dissertation help layout the following general recommendations:

- Careful materials selection in the form of cleaner aluminum alloys with a lower metallic inclusion content can enable a decrease in the magnitude of localized corrosion taking place in the form of pitting.
- The use of high performance coatings is critical to the safety and prevention of corrosion attack of the alloy surfaces. These coatings must be carefully designed to be stable over a range of temperature and pressure conditions that the structure can experience.
- Further improvement in the understanding of the environmental influence on the performance of structural aluminum alloys and couple geometries through the use of novel analysis techniques, such as those detailed in this dissertation. Furthermore, using these lab-scale testing protocols to develop standards that can be extended to simulate in-service mechanical stresses and corrosion scenarios to provide critical data to the industry.

7.2 Future Work

The results obtained over the course of these studies have opened new possibilities in terms of the experiments that can be conducted and insights that can be gained.

1. Lab scale Diffraction Contrast Tomography (LabDCT)- This lab-scale technique enables grain mapping in 3D non-destructively. Using DCT, a number of experiments can be performed to study grain boundary misorientation and grain orientation effects. The dissimilar metal couple studies can be greatly enhanced using this technique and can provide a comprehensive understanding of the influence of grain orientation on pit initiation, crack initiation and crack growth.

2. Micropillar grain mapping- The *ex situ* studies on the corrosion of peak aged and over aged micropillars have shown that grain boundary misorientation plays a critical role in deciding the corrosion behavior of the alloy. Further insights into this behavior can be obtained by grain mapping the entire pillar with serial sectioning EBSD and correlating the same with the sequence of corrosion attack.

3. *In situ* TXM corrosion studies - The *ex situ* corrosion experiments at 32-ID-C at Argonne National Laboratories provided valuable insights into the effect of ageing and misorientation on corrosion initiation and propagation. Observing corrosion in real time to study the local mechanisms acting simultaneously such as bubble formation, matrix dissolution etc. can be extremely interesting to study and valuable to the community.

REFERENCES

[1] E.A. Starke, J.T. Staley, Application of modern aluminum alloys to aircraft, 32 (1996) 131–172.

[2] J.C. Williams, E.A. Starke, Progress in structural materials for aerospace systems, Acta Mater. 51 (2003) 5775–5799. https://doi.org/10.1016/j.actamat.2003.08.023.

[3] J.R. (Joseph R.. Davis, Corrosion of aluminum and aluminum alloys, ASM International, 1999.

[4] O. Speidel, Stress Corrosion Cracking of Aluminum Alloys, Metall. Trans. A. 6 (1975).

[5] L. Molent, Managing airframe fatigue from corrosion pits - A proposal, Eng. Fract. Mech. 137 (2015) 12–25. https://doi.org/10.1016/j.engfracmech.2014.09.001.

[6] S.J. Findlay, N.D. Harrison, Why aircraft fail, Mater. Today. 5 (2002) 18–25. https://doi.org/10.1016/S1369-7021(02)01138-0.

[7] G.A. Shoales, S.A. Fawaz, M.R. Walters, Compilation Of Damage Findings From Multiple Recent Teardown Analysis Programs, ICAF 2009, Bridg. Gap between Theory Oper. Pract. (2009) 187–207. https://doi.org/10.1007/978-90-481-2746-7_11.

[8] W.C. Nickerson, U.S. Naval Aviation: Operational airframe experience with combined environmental and mechanical loading, Corros. Rev. 33 (2015) 285–291. https://doi.org/10.1515/corrrev-2015-0067.

[9] W.C. Nickerson, N. Iyyer, K. Legg, M. Amiri, Modeling galvanic coupling and localized damage initiation in airframe structures, Corros. Rev. 35 (2017) 205–223. https://doi.org/10.1515/corrrev-2017-0025.

[10] J.H.P. G.H. Koch, M.P.H. Brongers, N.G. Thompson, P. Virmani, Corrosion Costs and Preventative Strategies in the United States, 2002., NACE Int. (2002). https://trid.trb.org/view/707382.

[11] L. Herridge, Combating Corrosion, (2006). https://www.nasa.gov/centers/kennedy/news/corrosion.html.

[12] J. Caplan, M. Niethammer, R.M. Taylor, K.J. Czymmek, The power of correlative microscopy: Multi-modal, multi-scale, multi-dimensional, Curr. Opin. Struct. Biol. 21 (2011) 686–693. https://doi.org/10.1016/j.sbi.2011.06.010.

[13] T.L. Burnett, S.A. McDonald, A. Gholinia, R. Geurts, M. Janus, T. Slater, S.J. Haigh, C. Ornek, F. Almuaili, D.L. Engelberg, G.E. Thompson, P.J. Withers, Correlative Tomography, Sci. Rep. 4 (2015) 4711. https://doi.org/10.1038/srep04711.

[14] S.E. Galyon Dorman, J.W. Rausch, S. Arunachalam, S.A. Fawaz, Examination and prediction of corrosion fatigue damage and inhibition, Corros. Rev. 35 (2017) 355–363. https://doi.org/10.1515/corrrev-2017-0057.

[15] S.A. Fawaz, J. Schijve, Fatigue crack growth in riveted joints, ICAF97 Fatigue New Ageing Aircraft, Vols I Ii. (1997) 553–574.

[16] ASM International Handbook Committee, ASM Handbook Volume 2: Properties and Selection: Nonferrous Alloys and Special-Purpose Materials, 1990.

[17] S.S. Singh, C. Schwartzstein, J.J. Williams, X. Xiao, F. De Carlo, N. Chawla, 3D microstructural characterization and mechanical properties of constituent particles in Al 7075 alloys using X-ray synchrotron tomography and nanoindentation, J. Alloys Compd. 602 (2014) 163–174. https://doi.org/10.1016/j.jallcom.2014.03.010.

[18] T. Stannard, Corrosion and Corrosion-Fatigue Behavior of 7075 Aluminum Alloys Studied By In Situ X-Ray Tomography, Arizona State University, 2017.

[19] J. Bucci R.J, G Nordmark, E.A.Starke, Selecting aluminum alloys to resist failure by fracture mechanisms, ASM Handbook, Vol. 19 Fatigue Fract. 4 (1996) 771–812. https://doi.org/10.1361/asmhba000.

[20] V.K. Gupta, S.R. Agnew, Fatigue crack surface crystallography near crack initiating particle clusters in precipitation hardened legacy and modern Al-Zn-Mg-Cu alloys, Int. J. Fatigue. 33 (2011) 1159–1174. https://doi.org/10.1016/j.ijfatigue.2011.01.018.

[21] R.G. Buchheit, Local Dissolution Phenomena Associated with S Phase (Al_2CuMg) Particles in Aluminum Alloy 2024-T3, J. Electrochem. Soc. 144 (1997) 2621. https://doi.org/10.1149/1.1837874.

[22] N. Birbilis, R.G. Buchheit, Electrochemical Characteristics of Intermetallic Phases in Aluminum Alloys, J. Electrochem. Soc. 152 (2005) B140. https://doi.org/10.1149/1.1869984.

[23] K. Chawla, M. Meyers, Mechanical behavior of materials, 2009.

[24] K. Easterling, D.A. Porter, Phase transformations in metals and alloys, 1992.

[25] F. Viana, A.M.P. Pinto, H.M.C. Santos, A.B. Lopes, Retrogression and re-ageing of 7075 aluminium alloy: microstructural characterization, J. Mater. Process. Technol. 92–93 (1999) 54–59. https://doi.org/10.1016/S0924-0136(99)00219-8.

[26] C.S. Kaira, Structure property relationships in aluminum-copper alloys using transmission x-ray microscopy(TXM) and micromechanical testing, Arizona State University, 2017.

[27] R. Vallabhaneni, T.J. Stannard, C.S. Kaira, N. Chawla, 3D X-ray microtomography and mechanical characterization of corrosion-induced damage in 7075 aluminium (Al) alloys, Corros. Sci. 139 (2018) 97–113. https://doi.org/10.1016/J.CORSCI.2018.04.046.

[28] T.J. Stannard, J.J. Williams, S.S. Singh, A.S. Sundaram Singaravelu, X. Xiao, N. Chawla, 3D time-resolved observations of corrosion and corrosion-fatigue crack initiation and growth in peak-aged Al 7075 using synchrotron X-ray tomography, Corros. Sci. 138 (2018) 340–352. https://doi.org/10.1016/J.CORSCI.2018.04.029.

[29] N. Birbilis, M.K. Cavanaugh, R.G. Buchheit, Electrochemical behavior and localized corrosion associated with Al_7Cu_2Fe particles in aluminum alloy 7075-T651, Corros. Sci. 48 (2006) 4202–4215. https://doi.org/10.1016/j.corsci.2006.02.007.

[30] S.S. Singh, J.J. Williams, M.F. Lin, X. Xiao, F. De Carlo, N. Chawla, In situ investigation of high humidity stress corrosion cracking of 7075 aluminum alloy by three-dimensional (3D) X-ray synchrotron tomography, Mater. Res. Lett. 2 (2014) 217–220. https://doi.org/10.1080/21663831.2014.918907.

[31] N.J.H. Holroyd, A.K. Vasudevan, L. Christodoulou, Stress Corrosion of High-Strength Aluminum Alloys, Treatise Mater. Sci. Technol. 31 (1989) 463–483. https://doi.org/10.1016/b978-0-12-341831-9.50021-8.

[32] R. Braun, Environmentally assisted cracking of aluminium alloys, Materwiss. Werksttech. 38 (2007) 674–689. https://doi.org/10.1002/mawe.200700204.

[33] W. Schütz, Corrosion fatigue – the forgotten factor in assessing durability, in: 18th ICAF Symp. Proc., Melbourne, Australia, 1995.

[34] R.G. Kelly, J.R. Scully, D.W. Shoesmith, R. Buchheit, Electrochemical Techniques in Corrosion Science and Engineering, 2003.

[35] ASM International Handbook Committee, ASTM B117-19, Standard Practice for Operating Salt Spray (Fog) Apparatus ASTM International, in: West Conshohocken, PA, 2019.

[36] W.J. Schwerdtfeger, Laboratory measurement of the corrosion of ferrous metals in soils, J. Res. Natl. Bur. Stand. (1934). 50 (1953) 329. https://doi.org/10.6028/jres.050.043.

[37] S. Maitra, G.C. English, Mechanism of localized corrosion of 7075 alloy plate, Metall. Trans. A. 12 (1981) 535–541. https://doi.org/10.1007/BF02648553.

[38] X.L. Zhang, Z.H. Jiang, Z.P. Yao, Y. Song, Z.D. Wu, Effects of scan rate on the potentiodynamic polarization curve obtained to determine the Tafel slopes and corrosion current density, Corros. Sci. 51 (2009) 581–587. https://doi.org/10.1016/j.corsci.2008.12.005.

[39] J. Soltis, Passivity breakdown, pit initiation and propagation of pits in metallic materials - Review, Corros. Sci. 90 (2015) 5–22. https://doi.org/10.1016/j.corsci.2014.10.006.

[40] J.M. Kolotyrkin, Pitting corrosion of metals, in: Second Int. Congr. Met. Corros., New York, NY, 1963.

[41] H.H. Uhlig, Adsorbed and reaction-product films on metals, J. Electrochem. Soc. (1950).

[42] M.J.G. R. Goetz, B. MacDougall, An AES and SIMS study of the influence of chloride on the passive oxide film on iron, Electrochem. Acta. (1986).

[43] J.K. G.C. Wood, J.A. Richardson, M.F. Abd Rabbo, L.B. Mapa, W.H. Sutton, in: R. Frankenthal, Passivity of Metals, Electrochem. Soc. (1978) 973–979.

[44] P.M. Natishan, W.E. O'Grady, Chloride Ion Interactions with Oxide-Covered Aluminum Leading to Pitting Corrosion: A Review, J. Electrochem. Soc. 161 (2014) C421–C432. https://doi.org/10.1149/2.1011409jes.

[45] N. Sato, Toward a more fundamental understanding of corrosion processes, Corros. 45. (1989).

[46] J.R. Galvele, Transport processes in passivity breakdown-II. Full hydrolysis of the metal ions, Corros. Sci. (1981).

[47] R.K. Gupta, N.L. Sukiman, M.K. Cavanaugh, B.R.W. Hinton, C.R. Hutchinson, N. Birbilis, Metastable pitting characteristics of aluminium alloys measured using current transients during potentiostatic polarisation, Electrochim. Acta. 66 (2012) 245–254. https://doi.org/10.1016/j.electacta.2012.01.090.

[48] G.S. Frankel, T. Li, J.R. Scully, Localized Corrosion: Passive Film Breakdown vs Pit Growth Stability, J. Electrochem. Soc. 164 (2017) 180–181. https://doi.org/10.1149/2.1381704jes.

[49] Z. Szklarska-Smialowska, Pitting corrosion of aluminum, Corros. Sci. 41 (1999) 1743–1767. https://doi.org/10.1016/S0010-938X(99)00012-8.

[50] K.D. Ralston, N. Birbilis, M. Weyland, C.R. Hutchinson, The effect of precipitate size on the yield strength-pitting corrosion correlation in Al-Cu-Mg alloys, Acta Mater. 58 (2010) 5941–5948. https://doi.org/10.1016/j.actamat.2010.07.010.

[51] J.K. Park, A.J. Ardell, Microchemical analysis of precipitate free zones in 7075-A1 in the T6, T7 and RRA tempers, Acta Metall. Mater. 39 (1991) 591–598. https://doi.org/10.1016/0956-7151(91)90127-M.

[52] Z. Zhao, G.S. Frankel, On the first breakdown in AA7075-T6, Corros. Sci. 49 (2007) 3064–3088. https://doi.org/10.1016/j.corsci.2007.02.001.

[53] Q. Meng, G.S. Frankel, Effect of Cu Content on Corrosion Behavior of 7xxx Series Aluminum Alloys, J. Electrochem. Soc. 151 (2004) B271. https://doi.org/10.1149/1.1695385.

[54] Y. Liu, A. Laurino, T. Hashimoto, X. Zhou, P. Skeldon, G.E. Thompson, G.M. Scamans, C. Blanc, W.M. Rainforthd, M.F. Frolishd, Corrosion behaviour of mechanically polished AA7075-t6 aluminium alloy, Surf. Interface Anal. 42 (2010) 185–188. https://doi.org/10.1002/sia.3136.

[55] W. Tian, S. Li, B. Wang, J. Liu, M. Yu, Pitting corrosion of naturally aged AA 7075 aluminum alloys with bimodal grain size, Corros. Sci. 113 (2016) 1–16. https://doi.org/10.1016/j.corsci.2016.09.013.

[56] F. Andreatta, M.M. Lohrengel, H. Terryn, J.H.W. De Wit, Electrochemical characterisation of aluminium AA7075-T6 and solution heat treated AA7075 using a micro-capillary cell, Electrochim. Acta. 48 (2003) 3239–3247. https://doi.org/10.1016/S0013-4686(03)00379-7.

[57] J. Newton, N.J.H. Holroyd, Time-lapse video techniques in the corrosion testing of aluminum alloys, ASTM Spec. Tech. Publ. (1991) 153–179. https://doi.org/10.1520/stp19588s.

[58] A.S.S. Singaravelu, J.J. Williams, H.D. Goyal, S. Niverty, S.S. Singh, T.J. Stannard, X. Xiao, N. Chawla, 3D Time-Resolved Observations of Fatigue Crack Initiation and Growth from Corrosion Pits in Al 7XXX Alloys Using In Situ Synchrotron X-ray Tomography, Metall. Mater. Trans. A Phys. Metall. Mater. Sci. (2019). https://doi.org/10.1007/s11661-019-05519-z.

[59] T.J. Stannard, J.J. Williams, S.S. Singh, A.S. Sundaram Singaravelu, X. Xiao, N. Chawla, 3D time-resolved observations of corrosion and corrosion-fatigue crack initiation and growth in peak-aged Al 7075 using synchrotron X-ray tomography, Corros. Sci. 138 (2018) 340–352. https://doi.org/10.1016/j.corsci.2018.04.029.

[60] J.T. Burns, J.M. Larsen, R.P. Gangloff, Driving forces for localized corrosion-to-fatigue crack transition in Al-Zn-Mg-Cu, Fatigue Fract. Eng. Mater. Struct. 34 (2011) 745–773. https://doi.org/10.1111/j.1460-2695.2011.01568.x.

[61] R.M. Chlistovsky, P.J. Heffernan, D.L. DuQuesnay, Corrosion-fatigue behaviour of 7075-T651 aluminum alloy subjected to periodic overloads, Int. J. Fatigue. 29 (2007) 1941–1949. https://doi.org/10.1016/j.ijfatigue.2007.01.010.

[62] S. Suresh, Fatigue of Materials, 1998.

[63] T. Marlaud, B. Malki, C. Henon, A. Deschamps, B. Baroux, Relationship between alloy composition, microstructure and exfoliation corrosion in Al-Zn-Mg-Cu alloys, Corros. Sci. 53 (2011) 3139–3149. https://doi.org/10.1016/j.corsci.2011.05.057.

[64] A. Bonakdar, F. Wang, J.J. Williams, N. Chawla, Environmental Effects on Fatigue Crack Growth in 7075 Aluminum Alloy, Metall. Mater. Trans. A. 43 (2012) 2799–2809. https://doi.org/10.1007/s11661-011-0810-0.

[65] J.J. Williams, K.E. Yazzie, N. Connor Phillips, N. Chawla, X. Xiao, F. De Carlo, N. Iyyer, M. Kittur, On the correlation between fatigue striation spacing and crack growth rate: A three-dimensional (3-D) X-ray synchrotron tomography study, Metall. Mater. Trans. A Phys. Metall. Mater. Sci. 42 (2011) 3845–3848. https://doi.org/10.1007/s11661-011-0963-x.

[66] A. Nicolas, A.W. Mello, M.D. Sangid, The effect of strain localization on galvanic corrosion pitting in AA7050, Corrosion. 74 (2018) 860–872. https://doi.org/10.5006/2729.

[67] S.S. Singh, E. Guo, H. Xie, N. Chawla, Mechanical properties of intermetallic inclusions in Al 7075 alloys by micropillar compression, Intermetallics. 62 (2015) 69–75. https://doi.org/10.1016/j.intermet.2015.03.008.

[68] S.S. Singh, J.J. Williams, P. Hruby, X. Xiao, F. De Carlo, N. Chawla, In situ experimental techniques to study the mechanical behavior of materials using X-ray synchrotron tomography, Integr. Mater. Manuf. Innov. 3 (2014) 9. https://doi.org/10.1186/2193-9772-3-9.

[69] V.K. Gupta, R.P. Gangloff, S.R. Agnew, Diffraction characterization of microstructure scale fatigue crack growth in a modern Al-Zn-Mg-Cu alloy, Int. J. Fatigue. 42 (2012) 131–146. https://doi.org/10.1016/j.ijfatigue.2011.08.003.

[70] J.J. Williams, K.E. Yazzie, E. Padilla, N. Chawla, X. Xiao, F. De Carlo, Understanding fatigue crack growth in aluminum alloys by in situ X-ray synchrotron tomography, Int. J. Fatigue. 57 (2013) 79–85. https://doi.org/10.1016/j.ijfatigue.2012.06.009.

[71] P.S. Pao, S.J. Gill, C.R. Feng, On fatigue crack initiation from corrosion pits in 7075-T7351 aluminum alloy, Scr. Mater. 43 (2000) 391–396.

[72] P.S. Pao, C.R. Feng, S.J. Gill, Corrosion fatigue crack initiation in aluminum alloys 7075 and 7050, Corrosion. 56 (2000) 1022–1031. https://doi.org/10.5006/1.3294379.

[73] Y.J. Ro, S.R. Agnew, R.P. Gangloff, Environmental fatigue-crack surface crystallography for Al-Zn-Cu-Mg-Mn/Zr, Metall. Mater. Trans. A Phys. Metall. Mater. Sci. 39 A (2008) 1449–1465. https://doi.org/10.1007/s11661-008-9522-5.

[74] J.T. Burns, J.M. Larsen, R.P. Gangloff, Driving forces for localized corrosion-to-fatigue crack transition in Al-Zn-Mg-Cu, Fatigue Fract. Eng. Mater. Struct. 34 (2011) 745–773. https://doi.org/10.1111/j.1460-2695.2011.01568.x.

[75] R.S. Sidhu, N. Chawla, Three-dimensional microstructure characterization of Ag_3Sn intermetallics in Sn-rich solder by serial sectioning, Mater. Charact. 52 (2004) 225–230. https://doi.org/10.1016/j.matchar.2004.04.010.

[76] T.L. Burnett, S.A. McDonald, A. Gholinia, R. Geurts, M. Janus, T. Slater, S.J. Haigh, C. Ornek, F. Almuaili, D.L. Engelberg, G.E. Thompson, P.J. Withers, Correlative tomography, Sci. Rep. 4 (2014) 1–6. https://doi.org/10.1038/srep04711.

[77] A. Kirubanandham, I. Lujan-Regalado, R. Vallabhaneni, N. Chawla, Three Dimensional Characterization of Tin Crystallography and Cu_6Sn_5 Intermetallics in Solder Joints by Multiscale Tomography, Jom. 68 (2016) 2879–2887. https://doi.org/10.1007/s11837-016-2042-7.

[78] T.L. Burnett, R. Kelley, B. Winiarski, L. Contreras, M. Daly, A. Gholinia, M.G. Burke, P.J. Withers, Large volume serial section tomography by Xe Plasma FIB dual beam microscopy, Ultramicroscopy. (2016). https://doi.org/10.1016/j.ultramic.2015.11.001.

[79] Y. Suzuki, T. Asai, S. Nagai, K. Kajiwara, K. Hata, T. Iwata, Stability measurement of neon ion beam current emitted from supertip gas field ion source, in: Tech. Dig. - 25th Int. Vac. Nanoelectron. Conf. IVNC 2012, 2012: pp. 320–321. https://doi.org/10.1109/IVNC.2012.6316953.

[80] R. Okawa, Y. Morikawa, S. Nagai, T. Iwata, K. Kajiwara, K. Hata, Stability measurement of ion beam current from argon field ion source, E-Journal Surf. Sci. Nanotechnol. 9 (2011) 371–374. https://doi.org/10.1380/ejssnt.2011.371.

[81] S. Singh, C.S. Kaira, H. Bale, C. Huynh, A. Merkle, N. Chawla, In situ micropillar compression of Al/SiC nanolaminates using laboratory-based nanoscale X-ray microscopy: Effect of nanopores on mechanical behavior, Mater. Charact. 150 (2019) 207–212. https://doi.org/10.1016/j.matchar.2019.02.030.

[82] S.S. Singh, J.J. Loza, A.P. Merkle, N. Chawla, Three dimensional microstructural characterization of nanoscale precipitates in AA7075-T651 by focused ion beam (FIB) tomography, Mater. Charact. 118 (2016) 102–111. https://doi.org/10.1016/j.matchar.2016.05.009.

[83] T. Hashimoto, M. Curioni, X. Zhou, J. Mancuso, P. Skeldon, G.E. Thompson, Investigation of dealloying by ultra-high-resolution nanotomography, Surf. Interface Anal. 45 (2013) 1548–1552. https://doi.org/10.1002/sia.5176.

[84] K.E. Yazzie, J.J. Williams, N.C. Phillips, F. De Carlo, N. Chawla, Multiscale microstructural characterization of Sn-rich alloys by three dimensional (3D) X-ray synchrotron tomography and focused ion beam (FIB) tomography, Mater. Charact. 70 (2012) 33–41. https://doi.org/10.1016/j.matchar.2012.05.004.

[85] L. Renversade, R. Quey, W. Ludwig, D. Menasche, S. Maddali, R.M. Suter, A. Borbély, Comparison between diffraction contrast tomography and high-energy diffraction microscopy on a slightly deformed aluminium alloy, IUCrJ. 3 (2016) 32–42. https://doi.org/10.1107/S2052252515019995.

[86] C.S. Kaira, V. De Andrade, S.S. Singh, C. Kantzos, A. Kirubanandham, F. De Carlo, N. Chawla, Probing Novel Microstructural Evolution Mechanisms in Aluminum Alloys Using 4D Nanoscale Characterization, Adv. Mater. 1703482 (2017) 1–8. https://doi.org/10.1002/adma.201703482.

[87] P.J. Withers, X-ray nanotomography, Mater. Today. 10 (2007) 26–34. https://doi.org/10.1016/S1369-7021(07)70305-X.

[88] P.J. Withers, Fracture mechanics by synchrotron X-ray microscopy, Phil. Trans. R. Soc. A373 (2015) 0157. https://doi.org/http://dx.doi.org/10.1098/rsta.2013.0157.

[89] D.F. Swinehart, The Beer-Lambert law, J. Chem. Educ. 39 (1962) 333–335. https://doi.org/10.1021/ed039p333.

[90] Q. Zhang, S. Niverty, A.S.S. Singaravelu, J.J. Williams, E. Guo, T. Jing, N. Chawla, Microstructure and micropore formation in a centrifugally-cast duplex stainless steel via X-ray microtomography, Mater. Charact. 148 (2019) 52–62. https://doi.org/10.1016/j.matchar.2018.12.009.

[91] S. Niverty, J. Sun, J. Williams, F. Bachmann, N. Gueninchault, E. Lauridsen, N. Chawla, A Forward Modeling Approach to High-Reliability Grain Mapping by Laboratory Diffraction Contrast Tomography (LabDCT), JOM. 71 (2019) 2695–2704. https://doi.org/10.1007/s11837-019-03538-0.

[92] C. Holzner, L. Lavery, H. Bale, A. Merkle, S. Mcdonald, P. Withers, Y. Zhang, D.J. Jensen, M. Kimura, A. Lyckegaard, P. Reischig, E.M. Lauridsen, Diffraction Contrast Tomography in the Laboratory-Applications and Future Directions, Micros. Today. (2016). https://doi.org/10.1017/S1551929516000584.

[93] F.A. Almuaili, S.A. McDonald, P.J. Withers, D.L. Engelberg, Application of a Quasi In Situ Experimental Approach to Estimate 3-D Pitting Corrosion Kinetics in Stainless Steel, J. Electrochem. Soc. 163 (2016) C745–C751. https://doi.org/10.1149/2.0381613jes.

[94] W. Tian, S. Li, B. Wang, J. Liu, M. Yu, Pitting corrosion of naturally aged AA 7075 aluminum alloys with bimodal grain size, Corros. Sci. 113 (2016) 1–16. https://doi.org/10.1016/J.CORSCI.2016.09.013.

[95] A. Nicolas, A.W. Mello, M.D. Sangid, The Effect of Strain Localization on Galvanic Corrosion Pitting in AA7050, Corrosion. (2018). https://doi.org/10.5006/2729.

[96] J.T. Burns, J.M. Larsen, R.P. Gangloff, Effect of initiation feature on microstructure-scale fatigue crack propagation in Al-Zn-Mg-Cu, Int. J. Fatigue. 42 (2012) 104–121. https://doi.org/10.1016/j.ijfatigue.2011.08.001.

[97] N.E.C. Co, J.T. Burns, Effects of macro-scale corrosion damage feature on fatigue crack initiation and fatigue behavior, Int. J. Fatigue. 103 (2017) 234–247. https://doi.org/10.1016/j.ijfatigue.2017.05.028.

[98] N.E.C. Co, J.T. Burns, Galvanic corrosion-induced fatigue crack initiation and propagation behavior in AA7050-T7451, Corrosion. 72 (2016) 1215–1219. https://doi.org/10.5006/2132.

[99] R.G. Buchheit, N. Birbilis, Electrochemical microscopy: An approach for understanding localized corrosion in microstructurally complex metallic alloys, Electrochim. Acta. 55 (2010) 7853–7859. https://doi.org/10.1016/j.electacta.2010.04.046.

[100] N. Birbilis, M.K. Cavanaugh, R.G. Buchheit, Electrochemical behavior and localized corrosion associated with Al7Cu2Fe particles in aluminum alloy 7075-T651, Corros. Sci. 48 (2006) 4202–4215. https://doi.org/10.1016/j.corsci.2006.02.007.

[101] S.P. Knight, N. Birbilis, B.C. Muddle, A.R. Trueman, S.P. Lynch, Correlations between intergranular stress corrosion cracking, grain-boundary microchemistry, and grain-boundary electrochemistry for Al-Zn-Mg-Cu alloys, Corros. Sci. 52 (2010) 4073–4080. https://doi.org/10.1016/j.corsci.2010.08.024.

[102] S.K. Kairy, S. Turk, N. Birbilis, A. Shekhter, The role of microstructure and microchemistry on intergranular corrosion of aluminium alloy AA7085-T7452, Corros. Sci. 143 (2018) 414–427. https://doi.org/10.1016/j.corsci.2018.08.033.

[103] S.S. Singh, J.J. Williams, T.J. Stannard, X. Xiao, F. De Carlo, N. Chawla, Measurement of localized corrosion rates at inclusion particles in AA7075 by in situ three dimensional (3D) X-ray synchrotron tomography, Corros. Sci. 104 (2016) 330–335. https://doi.org/10.1016/j.corsci.2015.12.027.

[104] R. Goswami, S. Lynch, N.J.H. Holroyd, S.P. Knight, R.L. Holtz, Evolution of grain boundary precipitates in Al 7075 upon aging and correlation with stress corrosion cracking behavior, Metall. Mater. Trans. A Phys. Metall. Mater. Sci. 44 (2013) 1268–1278. https://doi.org/10.1007/s11661-012-1413-0.

[105] R.K. Gupta, N.L. Sukiman, K.M. Fleming, M.A. Gibson, N. Birbilis, Electrochemical Behavior and Localized Corrosion Associated with Mg2Si Particles in Al and Mg Alloys, ECS Electrochem. Lett. 1 (2012) C1–C3. https://doi.org/10.1149/2.002201eel.

[106] T. Hashimoto, X. Zhang, X. Zhou, P. Skeldon, S.J. Haigh, G.E. Thompson, Investigation of dealloying of S phase (Al_2CuMg) in AA 2024-T3 aluminium alloy using high resolution 2D and 3D electron imaging, Corros. Sci. 103 (2016) 157–164.

[107] G.S. Frankel, Pitting Corrosion of Metals, J. Electrochem. Soc. 145 (1998) 2186. https://doi.org/10.1149/1.1838615.

[108] F. Andreatta, H. Terryn, J.H.W. De Wit, Corrosion behaviour of different tempers of AA7075 aluminium alloy, Electrochim. Acta. 49 (2004) 2851–2862. https://doi.org/10.1016/j.electacta.2004.01.046.

[109] Z. Zhao, G.S. Frankel, The effect of temper on the first breakdown in AA7075, Corros. Sci. 49 (2007) 3089–3111. https://doi.org/10.1016/j.corsci.2007.02.004.

[110] F. Andreatta, Local electrochemical behavior of 7xxx aluminium alloys, University of Trento, 2004.

[111] E. Melilli, M. Trueba, S.P. Trasatti, Effect of chloride concentration on the repassivation behavior of structural Al alloys, Metall. Ital. 106 (2014) 29–33.

[112] I.M. Comotti, M. Trueba, S.P. Trasatti, The pit transition potential in the repassivation of aluminium alloys, Surf. Interface Anal. 45 (2013) 1575–1584. https://doi.org/10.1002/sia.5270.

[113] F. Andreatta, H. Terryn, J.H.W. de Wit, Effect of solution heat treatment on galvanic coupling between intermetallics and matrix in AA7075-T6, Corros. Sci. 45 (2003) 1733–1746. https://doi.org/10.1016/S0010-938X(03)00004-0.

[114] P.S. Pao, S.J. Gill, C.R. Feng, On fatigue crack initiation from corrosion pits in 7075-T7351 aluminum alloy, Scr. Mater. 43 (2000) 391–396. https://doi.org/10.1016/S1359-6462(00)00434-6.

[115] S.P. Knight, M. Salagaras, A.R. Trueman, The study of intergranular corrosion in aircraft aluminium alloys using X-ray tomography, Corros. Sci. 53 (2011) 727–734. https://doi.org/10.1016/j.corsci.2010.11.005.

[116] P. Hruby, S.S. Singh, J.J. Williams, X. Xiao, F. De Carlo, N. Chawla, Fatigue crack growth in SiC particle reinforced Al alloy matrix composites at high and low R-ratios by in situ X-ray synchrotron tomography, Int. J. Fatigue. 68 (2014) 136–143. https://doi.org/10.1016/j.ijfatigue.2014.05.010.

[117] F. Eckermann, T. Suter, P.J. Uggowitzer, A. Afseth, P. Schmutz, Investigation of the exfoliation-like attack mechanism in relation to Al-Mg-Si alloy microstructure, Corros. Sci. 50 (2008) 2085–2093. https://doi.org/10.1016/j.corsci.2008.04.003.

[118] B.J. Connolly, D.A. Horner, S.J. Fox, A.J. Davenport, C. Padovani, S. Zhou, A. Turnbull, M. Preuss, N.P. Stevens, T.J. Marrow, J.-Y. Buffiere, E. Boller, A. Groso, M. Stampanoni, X-ray microtomography studies of localised corrosion and transitions to stress corrosion cracking, Mater. Sci. Technol. 22 (2006) 1076–1085. https://doi.org/10.1179/174328406X114199.

[119] V. Rafla, A. King, S. Glanvill, A. Parsons, A. Davenport, J. Scully, Operando Observation of Galvanic Corrosion between AA7050-T7451 and 304 Stainless Steel in a Simulated Fastener Arrangement using X-ray Tomography, Corrosion. 71 (2015) 150806110456007. https://doi.org/10.5006/1813.

[120] A. Nicolas, N.E.C. Co, J.T. Burns, M.D. Sangid, Predicting fatigue crack initiation from coupled microstructure and corrosion morphology effects, Eng. Fract. Mech. 220 (2019). https://doi.org/10.1016/j.engfracmech.2019.106661.

[121] S.P. Knight, M. Salagaras, A.M. Wythe, F. De Carlo, A.J. Davenport, A.R. Trueman, In situ X-ray tomography of intergranular corrosion of 2024 and 7050 aluminium alloys, Corros. Sci. 52 (2010) 3855–3860. https://doi.org/10.1016/j.corsci.2010.08.026.

[122] M.B. Kelly, S. Niverty, N. Chawla, Electromigration in Bi-crystal pure Sn solder joints: Elucidating the role of grain orientation, J. Alloys Compd. 818 (2020) 152918. https://doi.org/10.1016/j.jallcom.2019.152918.

[123] M.B. Kelly, S. Niverty, N. Chawla, Four Dimensional (4D) Microstructural Evolution of Cu6Sn5 Intermetallic and Voids under Electromigration in Bi-crystal Pure Sn Solder Joints, Acta Mater. (2020). https://doi.org/10.1016/j.actamat.2020.02.052.

[124] N.C. Daniel Sinclair, Sridhar Niverty, 3D visualization and quantification of corrosion pitting in AA 7075-T651 with different processing conditions., 2020.

[125] F. Eckermann, T. Suter, P.J. Uggowitzer, A. Afseth, A.J. Davenport, B.J. Connolly, M.H. Larsen, F. De Carlo, P. Schmutz, In situ monitoring of corrosion processes within the bulk of AlMgSi alloys using X-ray microtomography, Corros. Sci. 50 (2008) 3455–3466. https://doi.org/10.1016/j.corsci.2008.09.015.

[126] F. Eckermann, T. Suter, P.J. Uggowitzer, A. Afseth, P. Schmutz, Investigation of the exfoliation-like attack mechanism in relation to Al-Mg-Si alloy microstructure, Corros. Sci. 50 (2008) 2085–2093. https://doi.org/10.1016/j.corsci.2008.04.003.

[127] P.C. King, I.S. Cole, P.A. Corrigan, A.E. Hughes, T.H. Muster, S. Thomas, FIB/SEM study of AA2024 corrosion under a seawater drop, part II, Corros. Sci. 55 (2012) 116–125. https://doi.org/10.1016/j.corsci.2011.10.012.

[128] M.J. Robinson, N.C. Jackson, The influence of grain structure and intergranular corrosion rate on exfoliation and stress corrosion cracking of high strength Al-Cu-Mg alloys, Corros. Sci. 41 (1999) 1013–1028. https://doi.org/10.1016/S0010-938X(98)00171-1.

[129] X. Liu, G.S. Frankel, B. Zoofan, S.I. Rokhlin, In Situ X-ray radiographic study of stress corrosion cracking in AA2024-T3, Corrosion. 62 (2006) 217–230. https://doi.org/10.5006/1.3278268.

[130] X.G.F. Zhao, Exfoliation corrosion kinetics of high strength aluminum alloys , Ohio State University, 2006.

[131] F.H. Cao, Z. Zhang, J.F. Li, Y.L. Cheng, J.Q. Zhang, C.N. Cao, Exfoliation corrosion of aluminum alloy AA7075 examined by electrochemical impedance spectroscopy, Mater. Corros. 55 (2004) 18–23. https://doi.org/10.1002/maco.200303691.

[132] M.J. Robinson, The role of wedging stresses in the exfoliation corrosion of high strength aluminum alloys, Corros. Sci. 23 (1983) 887–899.

[133] T. Marlaud, B. Malki, A. Deschamps, B. Baroux, Electrochemical aspects of exfoliation corrosion of aluminium alloys: The effects of heat treatment, Corros. Sci. 53 (2011) 1394–1400. https://doi.org/10.1016/j.corsci.2011.01.010.

[134] F.A. Almuaili, S.A. McDonald, P.J. Withers, A.B. Cook, D.L. Engelberg, Strain-induced reactivation of corrosion pits in austenitic stainless steel, Corros. Sci. 125 (2017) 12–19. https://doi.org/10.1016/j.corsci.2017.05.023.

[135] S. Jafarzadeh, Z. Chen, J. Zhao, F. Bobaru, Pitting, lacy covers, and pit merger in stainless steel: 3D peridynamic models, Corros. Sci. 150 (2019) 17–31. https://doi.org/10.1016/j.corsci.2019.01.006.

[136] P. Ernst, N.J. Laycock, M.H. Moayed, R.C. Newman, The mechanism of lacy cover formation in pitting, Corros. Sci. 39 (1997) 1133–1136. https://doi.org/10.1016/S0010-938X(97)00043-7.

[137] H.J. Kim, W.K. Kim, M.L. Falk, D.A. Rigney, MD simulations of microstructure evolution during high-velocity sliding between crystalline materials, Tribol. Lett. 28 (2007) 299–306. https://doi.org/10.1007/s11249-007-9273-2.

[138] A. Hughes, T.H. Muster, A. Boag, A.M. Glenn, C. Luo, X. Zhou, G.E. Thompson, D. McCulloch, Co-operative corrosion phenomena, Corros. Sci. 52 (2010) 665–668. https://doi.org/10.1016/j.corsci.2009.10.021.

[139] A.E. Hughes, A. Boag, A.M. Glenn, D. McCulloch, T.H. Muster, C. Ryan, C. Luo, X. Zhou, G.E. Thompson, Corrosion of AA2024-T3 Part II: Co-operative corrosion, Corros. Sci. 53 (2011) 27–39. https://doi.org/10.1016/j.corsci.2010.09.030.

[140] S. Molokov, R. Moreau, H.K. Moffatt, Magnetohydrodynamics- historical evolution and trends, 2007.

[141] L.M.A. Monzon, J.M.D. Coey, Magnetic fields in electrochemistry: The Lorentz force. A mini-review, Electrochem. Commun. 42 (2014) 38–41. https://doi.org/10.1016/j.elecom.2014.02.006.

[142] Y.C. Tang, A.J. Davenport, Magnetic Field Effects on the Corrosion of Artificial Pit Electrodes and Pits in Thin Films, J. Electrochem. Soc. 154 (2007) C362. https://doi.org/10.1149/1.2736662.

[143] S. Pondicherry, A Study on the effects of magnetic field on the corrosion behavior of materials, University of Texas at Arlington, 2014.

[144] K.L. Rabah, J.P. Chopart, H. Schloerb, S. Saulnier, O. Aaboubi, M. Uhlemann, D. Elmi, J. Amblard, Analysis of the magnetic force effect on paramagnetic species, J. Electroanal. Chem. 571 (2004) 85–91. https://doi.org/10.1016/j.jelechem.2004.04.014.

[145] R. Aogaki, K. Fueki, T. Mukaibo, Application of Magnetohydrodynamic Effect to the Analysis of Electrochemical Reactions 1. MHD Flow of an Electrolyte Solution in an Electrode－Cell with a short Rectangular Channel, Denki Kagaku. 43 (1975) 504–508. https://doi.org/10.5796/kogyobutsurikagaku.43.504.

[146] S. Lebouil, J. Tardelli, E. Rocca, P. Volovitch, K. Ogle, Dealloying of Al_2Cu, Al_7Cu_2Fe, and Al_2CuMg intermetallic phases to form nanoparticulate copper films, Mater. Corros. 65 (2014) 416–424. https://doi.org/10.1002/maco.201307550.

[147] F. Eckermann, T. Suter, P.J. Uggowitzer, A. Afseth, P. Schmutz, The influence of MgSi particle reactivity and dissolution processes on corrosion in Al-Mg-Si alloys, Electrochim. Acta. 54 (2008) 844–855. https://doi.org/10.1016/j.electacta.2008.05.078.

[148] W. Zhang, G.S. Frankel, Transitions between pitting and intergranular corrosion in AA2024, Electrochim. Acta. 48 (2003) 1193–1210. https://doi.org/10.1016/S0013-4686(02)00828-9.

[149] X.Y. Sun, B. Zhang, H.Q. Lin, Y. Zhou, L. Sun, J.Q. Wang, E.H. Han, W. Ke, Correlations between stress corrosion cracking susceptibility and grain boundary microstructures for an Al-Zn-Mg alloy, Corros. Sci. 77 (2013) 103–112. https://doi.org/10.1016/j.corsci.2013.07.032.

[150] X.Y. Sun, B. Zhang, H.Q. Lin, Y. Zhou, L. Sun, J.Q. Wang, E.H. Han, W. Ke, Atom probe tomographic study of elemental segregation at grain boundaries for a peak-aged Al-Zn-Mg alloy, Corros. Sci. 79 (2014) 1–4. https://doi.org/10.1016/j.corsci.2013.10.027.

[151] H. Zhao, F. De Geuser, A. Kwiatkowski da Silva, A. Szczepaniak, B. Gault, D. Ponge, D. Raabe, Segregation assisted grain boundary precipitation in a model Al-Zn-Mg-Cu alloy, Acta Mater. 156 (2018) 318–329. https://doi.org/10.1016/J.ACTAMAT.2018.07.003.

[152] V. De Andrade, A. Deriy, M.J. Wojcik, D. Gürsoy, D. Shu, K. Fezzaa, F. De Carlo, Nanoscale 3D imaging at the Advanced Photon Source, SPIE Newsroom. (2016). https://doi.org/10.1117/2.1201604.006461.

[153] W. Yang, S. Ji, Q. Zhang, M. Wang, Investigation of mechanical and corrosion properties of an Al-Zn-Mg-Cu alloy under various ageing conditions and interface analysis of η' precipitate, Mater. Des. 85 (2015) 752–761. https://doi.org/10.1016/j.matdes.2015.06.183.

[154] L. Molent, Managing airframe fatigue from corrosion pits - A proposal, Eng. Fract. Mech. 137 (2015) 12–25. https://doi.org/10.1016/j.engfracmech.2014.09.001.

[155] R. Domingo, Advisory Circular 43-4B - Corrosion Control for Aircraft, 2018. https://www.faa.gov/documentLibrary/media/Advisory_Circular/AC_43-4B.pdf.

[156] A.K. Vasudevan, K. Sadananda, P.S. Pao, Residual stress affecting environmental damage in 7075-T651 alloy, Corros. Rev. (2019). https://doi.org/10.1515/corrrev-2019-0018.

[157] J.N. Scheuring, Mechanical Properties of Aircraft Materials Subjected to Long Periods of Service Usage, J. Eng. Mater. Technol. 119 (1997) 380–386.

[158] R.H. Jones, Metal Matrix Composites, 2001. https://doi.org/10.1007/978-94-011-1266-6.

[159] F.P. Chiang, Damage of Al 2024 alloy due to sequential exposure to fatigue , corrosion and fatigue, Int. J. Fatigue. 20 (1998) 743–748.

[160] F. Mansfeld, E.P. Parry, Galvanic corrosion of bare and coated Al alloys coupled to stainless steel 304 or Ti-6Al-4V, Corros. Sci. 13 (1973) 605–621. https://doi.org/10.1016/S0010-938X(73)80027-7.

[161] F. Mansfeld, J.V. Kenkel, Galvanic corrosion of A1 alloys — II. Effect of solution composition, Corros. Sci. 15 (1975) 183–198. https://doi.org/10.1016/S0010-938X(75)80008-4.

[162] F. Mansfeld, J. V. Kenkel, Galvanic corrosion of Al alloys-III. The effect of area ratio, Corros. Sci. 15 (1975) 239–250. https://doi.org/10.1016/S0010-938X(75)80019-9.

[163] A. Imanian, M. Amiri, Phase Field Modeling of Galvanic Corrosion., ArXiv Mater. Sci. (n.d.) 1–24. https://doi.org/arXiv:1804.08517v1.

[164] K.B. Deshpande, Experimental investigation of galvanic corrosion: Comparison between SVET and immersion techniques, Corros. Sci. 52 (2010) 2819–2826. https://doi.org/10.1016/j.corsci.2010.04.023.

[165] K.B. Deshpande, Validated numerical modelling of galvanic corrosion for couples: Magnesium alloy (AE44)-mild steel and AE44-aluminium alloy (AA6063) in brine solution, Corros. Sci. 52 (2010) 3514–3522. https://doi.org/10.1016/j.corsci.2010.06.031.

[166] D. Snihirova, D. Höche, S. Lamaka, Z. Mir, T. Hack, M.L. Zheludkevich, Galvanic corrosion of Ti6Al4V -AA2024 joints in aircraft environment: Modelling and experimental validation, Corros. Sci. 157 (2019) 70–78. https://doi.org/10.1016/j.corsci.2019.04.036.

[167] C. Liu, V. Rafla, J.R. Scully, R.G. Kelly, Mathematical modeling of potential and current distributions for atmospheric corrosion of galvanic coupling in airframe components, Corrosion. (2015).

[168] V.K. Gupta, S.R. Agnew, Fatigue crack surface crystallography near crack initiating particle clusters in precipitation hardened legacy and modern Al-Zn-Mg-Cu alloys, Int. J. Fatigue. 33 (2011) 1159–1174. https://doi.org/10.1016/j.ijfatigue.2011.01.018.

[169] V.K. Gupta, R.P. Gangloff, S.R. Agnew, Diffraction characterization of microstructure scale fatigue crack growth in a modern Al-Zn-Mg-Cu alloy, Int. J. Fatigue. 42 (2012) 131–146. https://doi.org/10.1016/j.ijfatigue.2011.08.003.

[170] V. Rafla, A. Davenport, J.R. Scully, Determination of cathodic and anodic charge from operando x-ray tomography observation of galvanic corrosion of aluminum alloy 7050-T7451 and 304 stainless steel in a simulated fastener, Corrosion. 71 (2015) 1300–1303. https://doi.org/10.5006/1871.

[171] Z. Feng, Galvanic Corrosion of Coated Al Alloy Panels with More Noble Fasteners, Ohio State University, 2015.

[172] J. Schindelin, I. Arganda-Carreras, E. Frise, V. Kaynig, M. Longair, T. Pietzsch, S. Preibisch, C. Rueden, S. Saalfeld, B. Schmid, J.-Y. Tinevez, D.J. White, V. Hartenstein, K. Eliceiri, P. Tomancak, A. Cardona, Fiji: an open-source platform for biological-image analysis, Nat. Methods. 9 (2012) 676–682. https://doi.org/10.1038/nmeth.2019.

[173] ASTM International, Standard Practice for Preparing , Cleaning , and Evaluating Corrosion Test, Significance. 90 (1999) 1–9. https://doi.org/10.1520/G0001-03R11.2.

[174] P. Leblanc, G.S. Frankel, A Study of Corrosion and Pitting Initiation of AA2024-T3 Using Atomic Force Microscopy, J. Electrochem. Soc. (2002) 239–247. https://doi.org/10.1149/1.1471546.

[175] J. R. Davis, Corrosion of Aluminum and Aluminum Alloys, A S M International, 1999.

[176] Y. Xue, H. El Kadiri, M.F. Horstemeyer, J.B. Jordon, H. Weiland, Micromechanisms of multistage fatigue crack growth in a high-strength aluminum alloy, Acta Mater. 55 (2007) 1975–1984. https://doi.org/10.1016/j.actamat.2006.11.009.

[177] J.T. Burns, J.M. Larsen, R.P. Gangloff, Driving forces for localized corrosion-to-fatigue crack transition in Al-Zn-Mg-Cu, Fatigue Fract. Eng. Mater. Struct. 34 (2011) 745–773. https://doi.org/10.1111/j.1460-2695.2011.01568.x.

[178] A.J. McEvily, H. Matsunaga, On Fatigue Striations, Sci. Iran. B Mech. Eng. 17 (2010) 75–82.

[179] W.C. Connors, Fatigue striation spacing analysis, Mater. Charact. 33 (1994) 245–253. https://doi.org/10.1016/1044-5803(94)90046-9.

[180] M. Lo, R. Jones, D. Peng, A. Bowler, D. Edwards, Fatigue crack growth from environmentally induced damage in 7075 alloy, 34th ICAF Conf. 28th ICAF Symp. ICAF 2015. 2 (2015) 1074–1084. https://doi.org/10.13140/RG.2.1.1412.8489.

[181] Mendoza R, In-service corrosion issues in sustainment of naval aircraft, in: ASETS Def. Conf. Proc., 2012.

[182] M. Lo, R. Jones, D. Peng, A. Bowler, D. Edwards, Fatigue crack growth from environmentally induced damage in 7075 alloy, in: 34th ICAF Conf., 2015: pp. 1074–1084. https://doi.org/10.13140/RG.2.1.1412.8489.

[183] N. Brown, B. Clark, P. Kramer, N.E.C. Co, F. Friedersdorf, J. Burns, Corrosion modified fatigue analysis for next-generation damage-tolerant management, Corros. Rev. (2019). https://doi.org/10.1515/corrrev-2019-0037.

[184] V. Sabelkin, V.Y. Perel, H.E. Misak, E.M. Hunt, S. Mall, Investigation into crack initiation from corrosion pit in 7075-T6 under ambient laboratory and saltwater environments, Eng. Fract. Mech. 134 (2015) 111–123. https://doi.org/10.1016/j.engfracmech.2014.12.016.

[185] S.A. Fawaz, B. Andersson, Accurate stress intensity factor solutions for corner cracks at a hole, Eng. Fract. Mech. 71 (2004) 1235–1254. https://doi.org/10.1016/S0013-7944(03)00207-8.

[186] S. Arunachalam, S. Fawaz, Test method for corrosion pit-to-fatigue crack transition from a corner of hole in 7075-T651 aluminum alloy, Int. J. Fatigue. 91 (2016) 50–58. https://doi.org/10.1016/j.ijfatigue.2016.05.021.